

GRANT  
IN-43-CR  
36356

DESIGN OF THE PRIMARY AND  
SECONDARY PRE-TRMM AND TRMM  
GROUND TRUTH SITES

8143

Final Report  
Covering the Period  
March 16, 1990 to June 30, 1991

on

NASA Grant NAG-5-870

Submitted by

Michael Garstang, P.I.  
Geoffrey Austin, Co-P.I.  
Claire Cosgrove

University of Virginia  
Department of Environmental Sciences  
Charlottesville, VA 22903

9 August 1991

(NASA-CR-188795) DESIGN OF THE PRIMARY AND  
SECONDARY PRE-TRMM AND TRMM GROUND TRUTH  
SITES Final Report, 16 Mar. 1990 - 30 Jun.  
1991 (Virginia Univ.) 143 p

OSCL 068

N91-50577

Unclass

63/43 0036586

## 1. Overview

The Final Report on "Design of the Primary and Secondary Pre-TRMM and TRMM Ground Truth Sites" covers the period of February 1987 to June 1991.

During the grant period, semi-annual and annual reports were submitted as listed in Appendix I. Further results have been reported upon in papers and at conferences, in conference proceedings and in a M.S. thesis by Ms. Claire Cosgrove. Appendix II lists the reviewed and non-reviewed publications and presentations of results.

## 2. Recent Results

Results generated over the last six months of grant research are covered by 5 manuscripts attached under Appendix III.

Manuscript #1 addresses estimates of rain volume over the Peninsular of Florida during the summer (convective) season based upon the Manually Digitized Radar (MDR) data. This work shows diurnal patterns of rainfall and preferred rain areas. Rain volume, particularly from the hourly estimates, as well as rain rates are obtained and show agreement with previous estimates.

Manuscript #2 examines the diurnal characteristics of rainfall over Florida and over the near shore waters. Strong diurnal oscillations found over land are classified out over the near shore waters. The presence of rain at all hours of the day over the offshore waters suggests that the near shore region is being influenced by daytime production of rain over land and the nighttime production over the sea (beyond the near shore environment). The results, thus, suggest that a domain covering the land (peninsula) near shore region and part of the offshore ocean will contain a mix of diurnal periodicities: daytime maximum over land, nighttime maximum over the offshore and no diurnal signal over the near shore.

Manuscript #3 characterizes convective rainfall as measured over the east coast of central Florida. The 1-minute precipitation data collected by the Kennedy Space Center (KSC) rain gage network are analyzed to determine the statistical properties of the precipitation fields on an annual, monthly and seasonal basis. The 1990 rainfall data are compared with the historical rainfall records for the region (1895-1985 NCDC - Climate Division 3 - Central Florida). The occurrence of rain days and mean daily rainfall rates were determined on a monthly basis. The daily rainfall amounts were analyzed as frequency distributions over the entire network. It is generally stated in the literature that daily rainfall totals in the tropics have a high correlation with storm rainfall. Therefore, the daily rainfall analysis can also be considered as storm depth equivalent. This will be verified in subsequent analysis for

this subtropical region. Finally, the relationship between the mean daily rainfall amount and the percentage of the network recording rainfall was determined for each season. These results will be further investigated in terms of seasonal trend analyses. Individual rain events are being characterized in terms of intensity, duration, time of occurrence, average and maximum rainfall rates, total rainfall amounts, etc. These results are not included in this report but will be subsequently submitted for publication.

Manuscript #4 deals with the spatial and temporal variability of rainfall over Florida. Microwave and rain gauge model simulations are used to determine rainfall distributions and estimate potential errors in the optimal conversion between microwave brightness temperatures and rainfall rates. These are found to be highly sensitive to the spatial resolution of the measurements. The optimum relationship is found to be much less sensitive to the details of the vertical profile of precipitation. A strategy for the combined use of rain gauges, ground-based radar, and microwave VIS/IR satellite sensors is discussed.

The final manuscript reports upon comparisons between a land based radar (Patrick AFB) and an optical rain gauge onboard an anchored buoy 50 km offshore. The radar was calibrated against detailed rain gauge measurements for the Kennedy Space Flight Center network. Good agreement, based on this calibration, was obtained between the optical rain gauge and the radar estimate of rainfall.

### **3. Data Base**

A substantial and detailed rainfall data base has been acquired and transmitted to the TRMM office at Goddard for the Kennedy Space Flight Center network, the Florida Water Management District and from the Kwajalein Network in the Marshall Islands.

### **4. Acknowledgements**

The work on above was supported by a grant from NASA Goddard Space Flight Center. We wish to acknowledge this support with thanks as well as recognize with appreciation the moral and administrative support given us by Mr. Otto Thiele.

## APPENDIX I

### Listing of Project Reports

- 1988: Design of the Primary Pre-TRMM and TRMM Ground Truth Site, Annual Report, April.
- Design of the Primary Pre-TRMM and TRMM Ground Truth Site, Semi-Annual Report, September.
- 1989: Design of the Primary and Secondary Pre-TRMM and TRMM Ground Truth Sites, Annual Report, June.
- 1990: Design of the Primary and Secondary Pre-TRMM and TRMM Ground Truth Sites, Annual Report, April.

## APPENDIX II

### Listing of Conference Presentations/Published Papers Student Theses

#### Conference Presentations

- 1987: Austin, G.L.: On the combining of rain gauge, radar and satellite estimates of rainfall. Proc. Internat. Symp. on Trop. Precip. Mea., Tokyo, Japan, October 28-30.
- Garstang, M., C. Cosgrove, R. Swap and S. Greco: Estimation of tropical rainfall. Proc. Internat. Symp. on Trop. Precip. Mea., Tokyo, Japan, October 28-30.
- 1991: Cosgrove, C.M.: Areal estimation of mean monthly rainfall over the Florida peninsula. 3rd Internat. Conf. on Precipitation Modelling - Hydrologic and Meteorological Aspects, College Station, TX, February 27-1 March.
- Cosgrove, C.M.: Radar echo patterns over the peninsula of Florida and what they can tell us. Science Foundation for the EOS era: Physical Climate and Hydrology Workshop, University Park, PA, 22-26 July.
- Cosgrove, C.M.: Precipitation fields over Florida - rainfall patterns over time and space and extreme rain event characteristics. To be presented in Glucksburg, Germany, 30 September-1 October.

#### Thesis

- 1991: Cosgrove, C.M.: The spatial and diurnal distribution of rainfall over the peninsula of Florida. M.S. thesis, Dept. of Environmental Sciences, University of Virginia, Charlottesville, VA, 158 pp.

#### Published Papers

- 1990: Seed, A. and G.L. Austin: Variability of summer Florida rainfall and its significance for the estimation of rainfall by gages, radar and satellite. J. Geophys. Res., 95, D3, 2207-2215.

### APPENDIX III

#### Manuscripts Submitted/Under Preparation

- 1991: Cosgrove, C.M. and M. Garstang: An estimate of the convective rain volume over the Florida peninsula for the month of July. Submitted to J. Appl. Meteor.
- Cosgrove, C.M. and M. Garstang: Mean diurnal characteristics of radar echoes offshore and over the Florida peninsula. To be submitted to J. Clim.
- Cosgrove, C.M. and M. Garstang: Characteristics of rainfall over the Kennedy Space Flight Center. To be submitted.
- Turner, B.J. and G.L. Austin: Spatial variability of summer Florida precipitation and its impact on microwave radiometer rainfall measurements systems.
- Turner, B.J., G.L. Austin, J. Wilkerson and M. Garstang: On the calibration and use of radar and an optical rain gauge to measure oceanic rainfall.

7. Appl. Met.

AN ESTIMATE OF THE MEAN CONVECTIVE RAIN  
VOLUME OVER THE FLORIDA PENINSULA FOR  
THE MONTH OF JULY

Claire M. Cosgrove and Michael Garstang

Department of Environmental Sciences  
University of Virginia  
Charlottesville, VA 22903

### **Abstract**

This paper describes the use of manually digitized radar data to estimate convective rain volume and average rain rates over the peninsula of Florida for the month of July by applying the area-time integral (ATI) technique. The ATI method is simplistic in nature, requiring only two meteorological parameters, namely, the areal extent and duration of the rain events. The integrated area is then multiplied by a constant rain rate to estimate a rain volume. The data sources are National Weather Service (NWS) weather radars located at five coastal locations over the peninsula. Although their surveillance area is in excess of the study area, the rain volume estimates are for an area on the order of 80,000 km<sup>2</sup>.



## 1. Introduction

Byers (1948) was one of the first researchers to use radar to estimate rain volume. He noted that the rain rate of convective storms was closely related to the size of the storm system. Woodley et al. (1971) tested this idea and found that the horizontal size of a convective cell was an important characteristic which related to the yield of precipitation at that location. Other qualitative correlations were reported in South Dakota (Dennis et al., 1975), in North Dakota (Doneaud et al., 1981, 1984), over the eastern Atlantic Ocean (Hudlow et al., 1979) and again in south Florida (Gagin et al., 1985). Very high correlation was obtained between convective rainfall and its real-time integral using the ATI estimation technique developed by Doneaud et al. (1981). The correlation coefficient of 0.955 was determined between the radar estimated rain volume and the daily integrated rainfall coverage over an area of  $3.8 \times 10^4 \text{ km}^2$  (Doneaud et al., 1981). This power-law relationship had a regression line with a slope approaching unity. This implied that the average rain rate tended to be constant.

The applicability of the ATI method for different geographic and climatic regions was also demonstrated by Lopez and his colleagues (Lopez et al., 1983, 1989) using the Florida Area Cumulus Experiment (FACE-2) data. High correlation coefficients (0.92) between radar estimated volume and the integrated radar echo area were determined for the 12 hour period between 0800-2000

UTC during the summer months over an area of  $3.6 \times 10^4 \text{ km}^2$ . Their estimates were made for time intervals ranging from 5-min up to 1 h. It was found that by using the 1-h intervals, i.e., 12 observations of echo coverage, a reliable estimate of the rain volume was given.

Chiu (1988), using the radar data from the GARP Atlantic Tropical Experiment (GATE), established a strong relationship between the fractional area of convective cloud exceeding a rain rate threshold and the area average rainfall rate at an instant in time. His results delineated between convective rainfall and the stratiform portion of the storm cell at a threshold of  $5 \text{ mm h}^{-1}$  (Chiu, 1988). This method has been improved upon in an empirical and theoretical manner by Atlas et al. (1989). Estimates of areal average rainfall rates have been even more successful when a height threshold is incorporated into the method, along with the rain rate threshold (Rosenfeld et al., 1989).

The imminent advent of a space-based remote sensing platform specifically directed at measuring rainfall, i.e., Tropical Rainfall Measurement Mission (TRMM) (Theon and Fugono, 1988; Simpson et al., 1988) highlights the interest in assessing our ability to measure rainfall over relatively large areas ( $500 \times 500 \text{ km}$ ) integrated over time (30 days). The focus of this present work is to explore a simple and inexpensive approach for estimating areal rain volume and mean rain rates for such spatial and temporal dimensions.

This work is divided into four main parts. The first deals with the frequency of occurrence of echoes (six echo levels) over the nine year period, 1978-1986. The occurrence of each echo level is considered both as a percentage of the total echoes recorded and as a percentage of the total time in which echoes could occur. The second part is the mapping of the precipitation fields based on the percentage occurrence of the echoes. Next, the standard NWS radar rain rates are adjusted proportionally for the study area. The fourth part is the culmination of the foregoing whereby estimates of rain volume and rain rates are derived.

The rain estimation procedure used is considered an 'alternative' approach based upon Doneaud et al. (1981). It does not address the issue of the Z-R relationship nor the complicating factors that influence the reflectivity factor as measured by the radar as the raindrops pass through the atmosphere. Instead, the rainfall is considered in terms of its areal extent and duration of the rain event. The areal extent has been calculated from rainfall distribution maps, while the duration of rain events has been based on the frequency of occurrence of the radar echoes over the diurnal cycle and during a calendar month. The modified rain rates are taken as constant to determine the area rain volume.

## **2. Radar Data Source**

The manually digitized radar (MDR) data are encoded by personnel at the NWS radar sites located at or near the coastline

of the Florida peninsula (Fig. 1). The radars at Daytona, Miami and Tampa are the WSR-57 model while the WSR-74S model is located at West Palm Beach and Key West. Both radar models are 10 cm systems (S-band) with a parabolic antenna producing a  $2^\circ$  beamwidth. The radars operate continuously in plane mode scanning over a maximum range of 230 km (125 nmi). The reflectivity values are from scans taken at a base elevation angle of  $0.5^\circ$ . The specifications for both radar models are the same except for the peak power and minimum detectable signal (Table 1).

The hourly MDR data for the period 1978 to 1986, inclusive, were used in this study. A  $12 \times 12$  array of 144 grid cells was extracted from the operational NWS radar network dataset. In this locale, the grid cell covered an area of approximately  $34 \times 34 \text{ km}^2$ . This whole array covered the central and southern portions of the peninsula, between  $25^\circ$  and  $29^\circ\text{N}$ , and extended offshore 30 km from the southeast coastline, and over 150 km from the southwest and northeast shorelines (Fig. 2). The area covered by all the radars is in the order of  $16.5 \times 10^4 \text{ km}^2$ .

The radar return signals are automatically processed by a digital video integrator and processor (DVIP) unit to produce levels of echo intensities, VIP levels. There are six echo levels based on the standard Z-R relationship,  $Z = 200 R^{1.6}$ , where Z is the radar reflectivity and R is the rain rate. The maximum level of intensity, regardless of areal extent, is allocated to each grid cell. The one exception is with Level 1 echoes which

must cover at least 20% of the grid cell. The gridding procedure identifies the areas of maximum precipitation but does not reflect the persistence of the echoes nor areal coverage information. Each VIP level has a corresponding intensity and range of rainfall rates (Table 2).

### **3. Method of Analysis of Radar Data**

To measure precipitation successfully during the summer season and to estimate area rainfall over the peninsula of Florida, it was necessary not only to parameterize the nature of convection but also to depict the temporal and spatial distribution of the convective activity. Analysis of the radar data on an hourly basis is aimed at identifying regions of sub-peninsular scale forcing. The rainfall distribution maps generated for longer time periods, i.e., 3 h and 8 h periods, were intended to delineate rain areas on the larger scale depicting the mean areal extent of rainfall over a 30-day period.

The initial stage in the analyses was to ascertain the mean number of occurrences of each echo level during each month. From these values, the mean percentages of total echo hours (TEH) and of the total time were determined (Table 3). As L2 was the dominant echo level, occurring between 45% and 70% of all echo hours per month, it could potentially bias the subsequent analyses. Therefore, L2 echoes were separated out of the dataset. The L6 echoes were also removed from the analysis since they were only 1% or less of the total echo hours in any one month (Table 3a). The L6 echoes are indicative of very large

storms with strong convection in association with extensive areas of L3, L4 and L5 echoes. These three echo levels tend to fill the greater portion of the grid cell. This was in agreement with the findings of other researchers. Statistics of radar measurements in south Florida and other regions, indicate that convective rain systems tend to produce reflectivity maxima of moderate values with rare intense cores (Lopez, 1978; Lopez et al., 1983). Consequently, the combined echo levels, L3 + L4 + L5, were chosen to map the areas of deep cumulus convection and heavy rain.

The combined echo levels were initially mapped as a composite for the month. The analysis was then broken down into hourly increments. The number of occurrences of the combined echo levels was calculated as a ratio of deep cumulus/heavy rainfall to the total diurnal echo hours (TDEH) for each grid cell. At this point, the hourly contour plots for the month were drawn using the NCAR graphics package (McArthur, 1983). When addressing a single month, twenty-four contour maps were feasible to interpret and discuss, but the total number of maps over a whole year (288) became unmanageable. The table of occurrence of rain echoes was subjectively reassessed to group the data into suitable time frames which would still depict the diurnal distribution of the echoes and their spatial variation over the peninsula. As a result, 8 h periods were considered adequate for the winter months and 3 h periods for the summer. In this study, radar estimated rain volumes (RERV) for July were determined for

each rainfall distribution map, i.e., composite L3 + L4 + L5 for the month, for 8-h and 3-h periods, and hourly during the period typically associated with convective activity (1700-2400 UTC).

#### 4. Radar Estimated Rain Volume

The ATI method incorporates both the areal extent and duration of the rainfall (Doneaud et al., 1984). It is also referred to in the literature as the Integrated Rainfall Coverage (IRC) (Doneaud et al., 1981). The technique consists of estimating the rain volume,  $V$ , over an area,  $A$ , during the time,  $t$ , given by:

$$V = \int_t \int_A R \, dAdt$$

If the rainfall rate,  $R$ , is constant ( $R_c$ ) then

$$V = R_c \int_t \int_A dAdt .$$

The integrated rainfall coverage is approximated by summing the area-time integrals such that:

$$ATI = \sum a_i \Delta t = \int \int dAdt$$

where  $a_i$  is the area over which rain was detected during the  $i$ th observing period for the time interval  $\Delta t$ .

From previous research, it was found that the maximum hourly echo coverage is better correlated with the estimated areal rain volume than the average hourly echo coverage (Doneaud et al., 1981). Therefore, the maximum echo coverage is considered the better predictor of the rain volume. Maximum echo values are used in this study. Doneaud et al. (1981) also assessed the

significance of incorporating echo coverage of less than 1% of the total study area. Their results showed that all areas with rain should be used in estimating the rain volume. Also, the feasibility of estimating area rainfall for periods of hours over extended regions using hourly radar echo observations has been substantiated with a fairly high degree of accuracy (Lopez et al., 1989).

#### **5. Radar Surveillance Area**

In the present study, the radar surveillance area covered 166,464 km<sup>2</sup> and was comprised of two subregions; terrestrial, which covers 49% of the area (80,920 km<sup>2</sup>), and coastal waters, which comprise the remaining 51% of the MDR grid array (85,544 km<sup>2</sup>). The Florida Panhandle (Fig. 2) was not taken into consideration in the radar estimation of rainfall (RER). The lower limit of the standard convective rainfall rates are used as the rain rate constants respectively, for L3-L5 (Table 2). The lower limit was chosen to ensure a conservative estimate of the rain volume. The units for the standard rainfall rate are mm h<sup>-1</sup> over the area-time integral in km<sup>2</sup> h, the product of which results in the area rain volume in mm km<sup>2</sup>.

#### **6. Rainfall Distribution Maps**

The contour maps depicting the rain areas are a type of isohyetal maps. The contours correspond to convective rainfall (L3-L5) as discrete percentages of either the TEH or the TDEH. The area contained between the contours needs to be measured. This time integrated contour area is then multiplied by the



appropriate rain rate, i.e., for L3 + L4 + L5, and by the mean percentage occurrence of the echoes, i.e., average of the two contours bounding the measured area. The summation of these products gives the total radar estimated rain volume for the time period of integration. However, the echoes only occur for a portion of the time. The total radar estimated rain volume (RERV), must be adjusted according to the frequency of each echo level with respect to the total echo hours (Table 3a) and the total number of hours in the month (Table 3b). Therefore, the area measured between the contours only exists for a portion of the time.

#### **7. Limitations Associated with MDR Data**

There are limitations with the MDR data which tend to under- and/or overestimate the rain rates at different ranges from the radar. These factors are mainly dependent on the radar characteristics. Other aspects need to be addressed when undertaking quantitative estimates of rainfall. The limit of the radar range for hydrological purposes is about 185 km (100 nmi) (Moore and Smith, 1979). The MDR grid cells are large relative to the characteristic size of intense thunderstorms and isolated convective cells. There are no data regarding the echo coverage within the grid cell. This uncertainty is a major limitation when making quantitative estimations. It is necessary to make certain assumptions regarding the extent of grid cell coverage by the echoes. First, the reported echo may cover any portion of the grid cell. Assume that the area enclosed by a L6 contour is

smaller than that of the L5, the area of the L5 echo being smaller than the L4 echo, and so on. The result is a series of successively smaller echo levels surrounding the more intense core of the rain cell. The area covered by an echo increases as the level of the echo decreases. The data represent only hourly 'snapshots' of the rainfall activity. There is no indication of echo movement, neither growth nor decay, and consequently, no indication of the varying rainfall intensities. Therefore, a deterministic approach is not feasible whereas a probabilistic assessment of the rainfall likely to occur at a given point in the radar cell may be acceptable.

In determining the possible rainfall volume in a radar cell, 50% of the radar estimated rainfall can be considered the 'most likely maximum' but needs to be adjusted for 'wetter' or 'drier' conditions (Moore and Smith, 1979). In areas subjected to short-lived, rapidly moving and/or small echo areas, 50% of the rainfall amount will be an overestimate of the 'most likely maximum' rainfall (Moore and Smith, 1979). As seen from Table 3a, 20% of the TEH in July consist of L3 echoes, L4 echoes are 20% of the TEH and L5 are less frequent, only 13% of the TEH. Instead of the 50% adjustment suggested in the literature, the use of 20% was chosen as the more appropriate factor for the Florida area based on the values in Table 3a. The total radar estimated rain volume can therefore be considered as the most likely maximum rainfall. This type of adjustment is necessary since it is assumed that the radar data covers the entire grid

cell and the conversion factor for changing the echo value to rainfall amount is an hourly rain rate.

#### 8. Adjusted MDR Rain Rates for Florida

The above adjustments are now applied. The standard MDR rain rates were adjusted by taking the lower limit of the convective rain rates for each echo level (Table 2) and multiplying by the occurrence of each echo level as a percentage of the total echo hours (Table 3a).

#### 9. Areal Rain Volume Estimates

The radar estimated rain volume (RERV) is determined using the areal coverage of radar echoes as measured from the various contour maps for the month of July. Estimates are made for rain contributions for the combined echoes L3, L4 and L5. The 8 hour, 3 hour and hourly maps are also used to derive rain volume estimates for the corresponding time periods. Summations are made for the peak rainfall period, 1700-2400 UTC, and for the 24-hour cycle.

##### a. Combined echo levels (L3, L4 and L5)

The area covered by the combined echo levels, L3 + L4 + L5, was measured off the contour map (Fig. 3). The contribution of rainfall from each echo level was determined. The total rain volume for the entire area was

$$17.35 \times 10^4 \text{ mm km}^2$$

with an hourly rain rate of

$$2 \text{ mm h}^{-1} .$$

b. 8-hour echo levels

The area covered by echo L3-L5 over the 8-hour periods are measured off the contour maps (Figs. 4a-c). These rain areas are used to determine the rain volume over the land during these time periods. The results are given in Table 4.

c. 3-hour echo levels

The same was done for the 3-hour periods. The echo coverage of the land is measured off Figs. 5a-h. The results are given in Table 5.

d. Hourly echo levels

The same was done for the hourly radar estimated rain volumes using Figs. 6a-h. Results are provided in Table 6.

## 10. Discussion

The estimated rain volume from the combined echo levels (L3-L5,  $17.35 \times 10^4$  mm km<sup>2</sup>) corresponds closely with the calculation based on the hourly values ( $15.6 \times 10^4$  mm km<sup>2</sup>). There is a 10% difference which is within the limits of the measurement error. Both rain volume estimates based on the 3-hour ( $66.0 \times 10^4$  mm km<sup>2</sup>) and 8-hour ( $205 \times 10^4$  mm km<sup>2</sup>) values appear to be gross overestimates. This reflects the fact that areal integration of radar echoes is not proportional to the area integrated rain rates. It is a non-linear relationship between the echo area and the equivalent rain rate. The adjustments applied to the calculations are not adequate for handling the calculation of the rain volume over time periods greater than one hour.

Based on the foregoing calculations, it would appear that a reasonable estimate of area rain volume for the month of July is between  $15 \times 10^4$  and  $18 \times 10^4$  mm km<sup>2</sup> with a rain rate of about 2 mm h<sup>-1</sup>. The rain rate of 2 mm h<sup>-1</sup> is the same as that obtained in a study undertaken at McGill University over an area one-third the size of the Florida peninsula (Zawadzki, 1973). From studies undertaken in south Florida, the area average rainfall on sea breeze days ranged between 0.3-13.5 mm d<sup>-1</sup> (Burpee and Lahiff, 1984). On highly disturbed days, the value of the rain rate exceeded 20 mm d<sup>-1</sup> and averaged 33 mm d<sup>-1</sup>. The average rainfall rate was estimated for both sea breeze (undisturbed) and disturbed days as 6.5 mm d<sup>-1</sup> and 8.7 mm d<sup>-1</sup>, respectively. Summer days are made up of 57% sea breeze days and 39% disturbed days. A rain rate of 2 mm h<sup>-1</sup> represents the lower end of the range of daily rainfall rates.

The work of Lopez et al. (1989) indicated that a time period of 1 h was the optimum time interval for estimating rainfall based on echo coverage as measured by radar. As the time interval increased beyond 60 min, the correlation coefficient relating rain volume to rain area decreased. The rain rate determined in their study was,  $R_c = 3.4$  mm h<sup>-1</sup> at a threshold of 18 dBz or 0.33 mm h<sup>-1</sup>. Their radar estimated rain volumes for an area of  $3.6 \times 10^4$  km<sup>2</sup> over a time period of 12 h showed extreme variability. The estimates ranged from  $10^2$  to  $1.64 \times 10^6$  m<sup>3</sup>. However, their correlations between integrated radar echo

coverage and rain volume were as high as 0.92. The results of this study appear to bear resemblance to those of Lopez et al. (1989) when the size of the study areas and the time interval for the estimates of rain volume are taken into consideration (Table 7).

#### 11. Summary and Conclusions

The MDR data from 1978 to 1986, covering the central and southern portion of the peninsula, were used to estimate area rain volume and determine a mean rain rate for the month of July. These estimates were based on the percentage occurrence of three levels of radar echoes (L3, L4 and L5). Level 3 echo intensity was used as the threshold to delineate between heavy and light rainfall, and an adjusted rain rate was used to determine rain volume via the ATI technique.

Conclusions that can be drawn from the study are that radar echoes can be mapped over a region to depict the spatial pattern of rainfall and its development during the diurnal cycle. The resultant series of rainfall distribution maps are a valuable source in themselves depicting the preferred rain areas but can also be used to determine area rain volume by applying such methods as the area-time integral technique. The estimated area rain volume is a probability rather than an exact measure of the rainfall. However, this rain volume should be an indicator of the most likely maximum precipitation over the region.

In this study, the range of the estimated average rain rates reflects the importance of the time period for which these

estimates are made. On the 8-hour basis, the average hourly rain rate varied from  $0.25 \text{ mm h}^{-1}$  to  $2.5 \text{ mm h}^{-1}$ . These results indicate that the main rain associated echoes occur between 1700 and 2400 UTC. The average hourly rain rate, estimated on the 3-hour basis, ranged from  $0.02 \text{ mm h}^{-1}$  during the night hours to around  $1.0 \text{ mm h}^{-1}$  from midday through to the early evening. On the hourly basis, the significant period of radar echoes appeared to be from 1900 through to 2200 UTC when the average rain rate fluctuated around  $0.4 \text{ mm h}^{-1}$ . It appears that estimates of rain rates are best determined from the longer time period analyses, either the 8-hour maps or the combined L3, L4 and L5 map for the whole month.

All of these estimated average rain rates appear low especially when compared with those rates given elsewhere in the literature for south Florida. However, the relative importance of the values is still valid in identifying the significant hours during the day when convective activity is most likely to occur. The study also illustrates a potential use for MDR data in mapping precipitation fields in time and space domains.

The estimated rain volumes determined in the study cover a wide range of values. With the ATI estimation technique, a linear relationship is applied to the rain areas resulting in a smoothed distribution of precipitation. This resulted in an overestimation of the rain volume on the 3-hour and 8-hour rainfall maps. The results obtained from the hourly rainfall maps are better estimates of the probable area rain volume.

Acknowledgement

This research has been supported under a grant from  
NASA/Goddard Space Flight Center.



### References

- Atlas, D.D., D. Rosenfeld and D.A. Short, 1989: The estimation of convective rainfall by area integral. Part I: The theoretical and empirical basis. J. Geophys. Res., 95, 2153-2160.
- Burpee, R.W. and L.N. Lahiff, 1984: Area-average rainfall variations on sea-breeze days in south Florida. Mon. Wea. Rev., 112, 520-534.
- Byers, H.R., 1948: The use of radar in determining the amount of rain falling over a small area. EOS Trans., 29, 187-196.
- Chiu, L.S., 1988: Estimating areal rainfall from rain area. In Tropical Rainfall Measurement, J.S. Theon and N. Fugano (eds.), A. Deepak Publishing, Hampton, VA, 361-367.
- Dennis, A.S., A. Koscielski, D.E. Cain, J.H. Hirsch and P.L. Smith, Jr., 1975: Analysis of radar observations of a randomized cloud seeding experiment. J. Appl. Meteor., 14, 897-908.
- Doneaud, A.A., P.L. Smith, A.S. Dennis and S. Sengupta, 1981: A simple method for estimating convective rain volume over an area. Water Resour. Res., 17, 1676-1782.
- \_\_\_\_\_, S.I. Niscov, D.L. Priegnitz and P.L. Smith, 1984: The area-time integral as an indicator for convective rain volumes. J. Clim. Appl. Meteor., 23, 555-561.
- Gagin, A.D., D. Rosenfeld and R.E. Lopez, 1985: The relationship between height and precipitation characteristics of

summertime convective cells in south Florida. J. Atmos. Sci., 42, 492-508.

Hudlow, M.R., R. Arkell, V. Patterson, P. Pytlowany, F. Richards and S. Geotis, 1979: Calibration and intercomparison of the GATE C-band radars. NOAA Tech. Rept. EDIS 31, U.S. Dept. of Commerce, Washington, D.C., 98 pp.

Lopez, R.E., 1978: Internal structure and processes of C-scale aggregates of cumulus clouds. Mon. Wea. Rev., 106, 1488-1494.

\_\_\_\_\_, J. Thomas, D.O. Blanchard and R.L. Holle, 1983: Estimation of rainfall over an extended region using only measurements of the area covered by radar echoes. Preprints A.M.S. 21st Conf. Radar Meteor., Edmonton, Canada, 681-686.

\_\_\_\_\_, D. Atlas, D. Rosenfeld, J.L. Thomas, D.O. Blanchard and R.L. Holle, 1989: Estimation of areal rainfall using the radar echo area time integral. J. Appl. Meteor., 28, 1162-1175.

McArthur, G. (ed.), 1983: The SCD graphics utilities. NCAR-TN/166-1A, Scientific Computing Division, National Center for Atmospheric Research, Boulder, CO.

Moore, P.L. and D.S. Smith, 1979: Manually digitized radar data - interpretation and applications. NOAA Tech. Memo National Weather Service SR-99, 24 pp.

Rosenfeld, D.D., D. Atlas and D.A. Short, 1989: The estimation of convective rainfall by area integrals. Part II: The height-area threshold (HART) method. J. Geophys. Res.,

95, 2161-2176.

Simpson, J., R.F. Adler and G.R. North, 1988: A proposed Tropical Rainfall Measuring Mission (TRMM) satellite. Bull. Amer. Meteor. Soc., 69, 278-295.

Theon, J.S. and N. Fugono (eds.), 1988: Tropical Rainfall Measurements, A Deepak Publishing, Hampton, VA, 528 pp.

Woodley, W.L., J. Norwood and S. Briseida, 1971: Some precipitation aspects of Florida showers and thunderstorms. Weatherwise, 24, 106-114.

Zawadzki, I.I., 1973: Statistical properties of precipitation patterns. J. Appl. Meteor., 12, 459-472.

### List of Figures

- Fig. 1: Range of the radar scope over the peninsula of Florida. The range of the radar is depicted at 185 km (100 nmi).
- Fig. 2: The manually digitized radar (MDR) array of 144 grid cells over the Florida peninsula.
- Fig. 3. Contour map for the combined echo levels: L3, L4 and L5, for the month of July depicting the spatial rainfall distribution as a percentage of the TEH.
- Fig. 4a: Contour map for the 8-hour time period 0100-0800 UTC for the month of July depicting the spatial distribution of the rainfall as a percentage of the TDEH.
- Fig. 4b: Contour map for the 8-hour time period 0900-1600 UTC for the month of July depicting the spatial distribution of the rainfall as a percentage of TDEH.
- Fig. 4c: Contour map for the 8-hour time period 1700-2400 UTC for the month of July depicting the spatial distribution of the rainfall as a percentage of the TDEH.
- Fig. 5a-d: Contour maps for 3-hour time period for the month of July depicting the spatial distribution of the rainfall. (a) 0200-0400 UTC; (b) 0500-0700 UTC; (c) 0800-1000 UTC; and (d) 1100-1300 UTC.
- Fig. 5e-h: Contour maps for 3-hour time periods for the month of July depicting the spatial distribution of the rainfall. (e) 1400-1600 UTC; (f) 1700-1900 UTC; (g) 2000-2200; and (h) 2300-0100 UTC.

Fig. 6a-d: Contour maps for the hours of peak rainfall for the month of July depicting the spatial distribution as a percentage of TDEH. (a) 1700 UTC; (b) 1800 UTC; (c) 1900 UTC; and (d) 2000 UTC.

Fig. 6e-h: Contour maps for the hours of peak rainfall for the month of July depicting the spatial distribution as a percentage of TDEH. (e) 2100 UTC; (f) 2200 UTC; (g) 2300 UTC; and (h) 2400 UTC.

TABLE 1  
Characterisics of the MDR radar.

Location		Radar Model
Daytona		WSR-57
Miami		WSR-57
Tampa		WSR-57
West Palm Beach		WSR-74S
Key West		WSR-74S
<hr style="border-top: 1px dashed black;"/>		
Specifications	WSR-57	WSR-74S
<hr/>		
<u>Antenna:</u> Parabolic dish		
Diameter (ft)	12	12
Beam width (degrees)	2.0	2.0
Wavelength (cm)	10.53	10.53
<u>Transmitter:</u>		
Peak power (kW)	410	403
Pulse repetition frequency (PRF-s <sup>-1</sup> )	164	164
Frequency (MHz)	2700-2900	2700-2900
Pulse duration (u s)	4	4
Pulse speed (m s <sup>-1</sup> )	3 x 10 <sup>8</sup>	3 x 10 <sup>8</sup>
<u>Receiver:</u>		
Min. detectable signal (dBm)	106	-
Max. range (km)	450	450

TABLE 2

Manually digitized radar intensity code.

Code No.	Intensity	<u>Rainfall Rate (mm/h)</u>	
		Stratiform	Convective
1	Light	<2.5	<5.0
2	Moderate	2.5-13.0	5.0-28.0
3	Strong	13.0-25.0	28.0-56.0
4	Very Strong	25.0-51.0	56.0-114.0
5	Intense	51.0-127.0	114.0-180.0
6	Extreme	>127.0	>180.0

TABLE 3

The seasonal distribution of echo levels as (a) mean percentage of the total cho hours (TEH), (b) mean percentage of the total time (TT).

---

**a. Mean percentage of total echo hous (TEH)**

	JAN	FEB	MAR	APR	MAY	JUN	JUL	AUG	SEP	OCT	NOV	DEC
L2	69	66	62	45	50	46	45	46	51	45	67	70
L3	18	19	20	21	21	21	21	21	22	21	20	18
L4	10	10	12	20	17	20	20	20	18	20	10	9
L5	3	5	6	13	11	12	13	12	8	13	3	3
L6	0	0	1	1	1	1	1	1	0	0	0	0

---

**b. Mean percentage of total time (TT)**

	JAN	FEB	MAR	APR	MAY	JUN	JUL	AUG	SEP	OCT	NOV	DEC
L2	2	3	3	3	4	7	7	8	8	5	4	3
L3	1	1	1	1	2	3	3	4	3	2	1	1
L4	0	1	1	1	1	3	3	4	3	1	1	0
L5	0	0	0	0	1	2	2	2	1	0	0	0
L6	0	0	0	0	0	0	0	0	0	0	0	0
TOTAL	3	5	5	4	8	15	15	18	15	8	6	4

---



TABLE 4

Area rain volume estimates and mean hourly rain rate  
based on 8-hour radar echo contour maps.

	$10^4 \text{ km}^2$	$\text{mm km}^2$	$\text{mm h}^{-1}$
0100-0800 UTC	7.67	$18 \times 10^4$	0.25
0900-1600 UTC	8.38	$25 \times 10^4$	0.38
1700-2400 UTC	7.46	$162 \times 10^4$	2.5
Total RER:			
0100-2400 UTC		$205 \times 10^4$	

TABLE 5

Area rain volume estimates and mean hourly rain rate  
based on 3-hour radar echo contour maps.

	$\times 10^4 \text{ km}^2$	$\text{mm km}^2$	$\text{mm h}^{-1}$
0200-0400 UTC	1.73	$1.4 \times 10^4$	0.07
0500-0700 UTC	0.53	$0.4 \times 10^4$	0.02
0800-1000 UTC	0.61	$0.5 \times 10^4$	0.02
1100-1300 UTC	0.57	$0.5 \times 10^4$	0.02
1400-1600 UTC	4.40	$6.4 \times 10^4$	0.23
1700-1900 UTC	7.07	$23.0 \times 10^4$	0.9
2000-2200 UTC	6.92	$26.0 \times 10^4$	1.0
2300-0100 UTC	6.17	$8.7 \times 10^4$	0.3
Total RER:			
0200-0100 UTC	$66.9 \times 10^4$		

TABLE 6

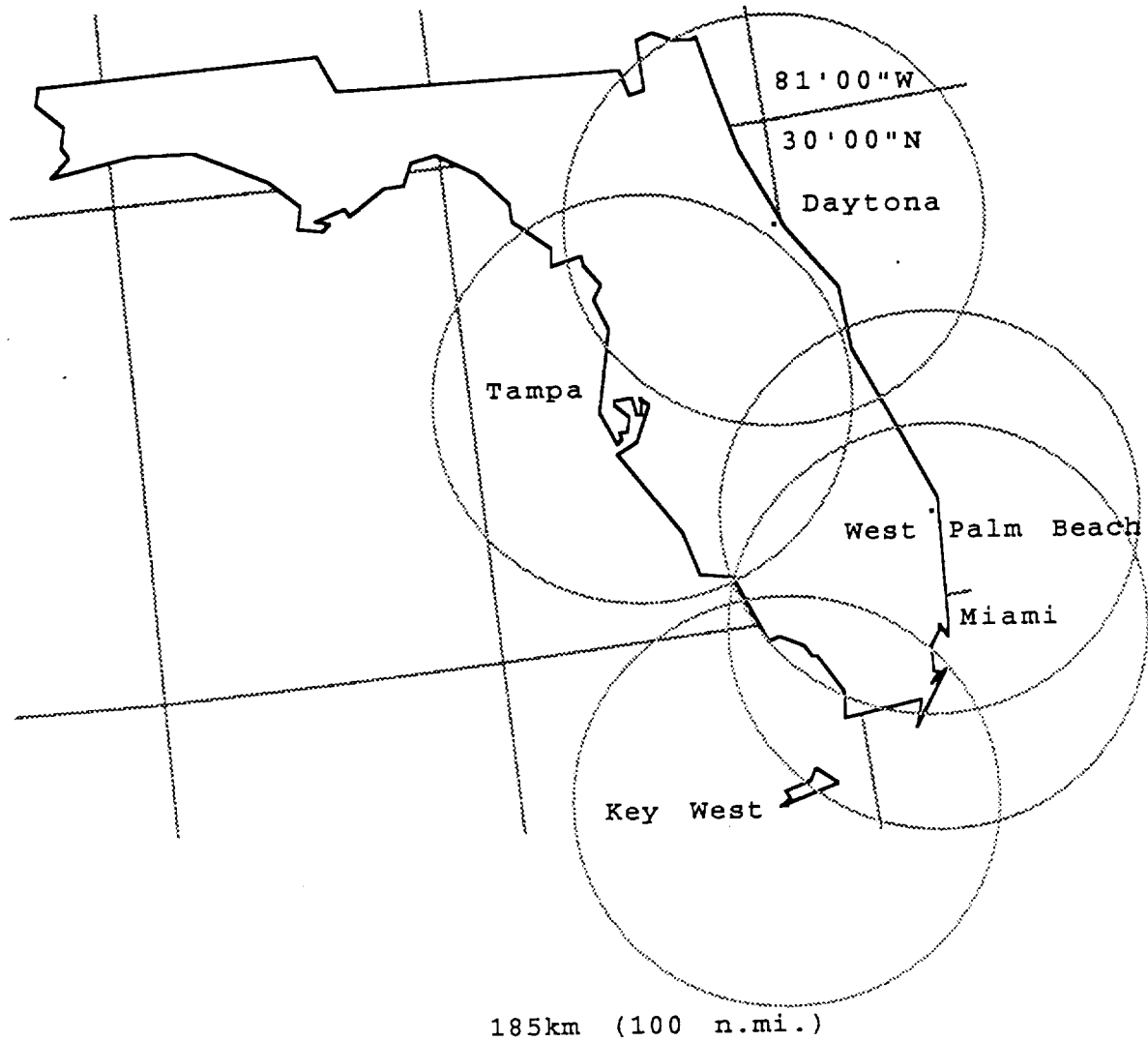
Area rain volume estimates and mean hourly rain rate  
based on hourly radar echo contour maps.

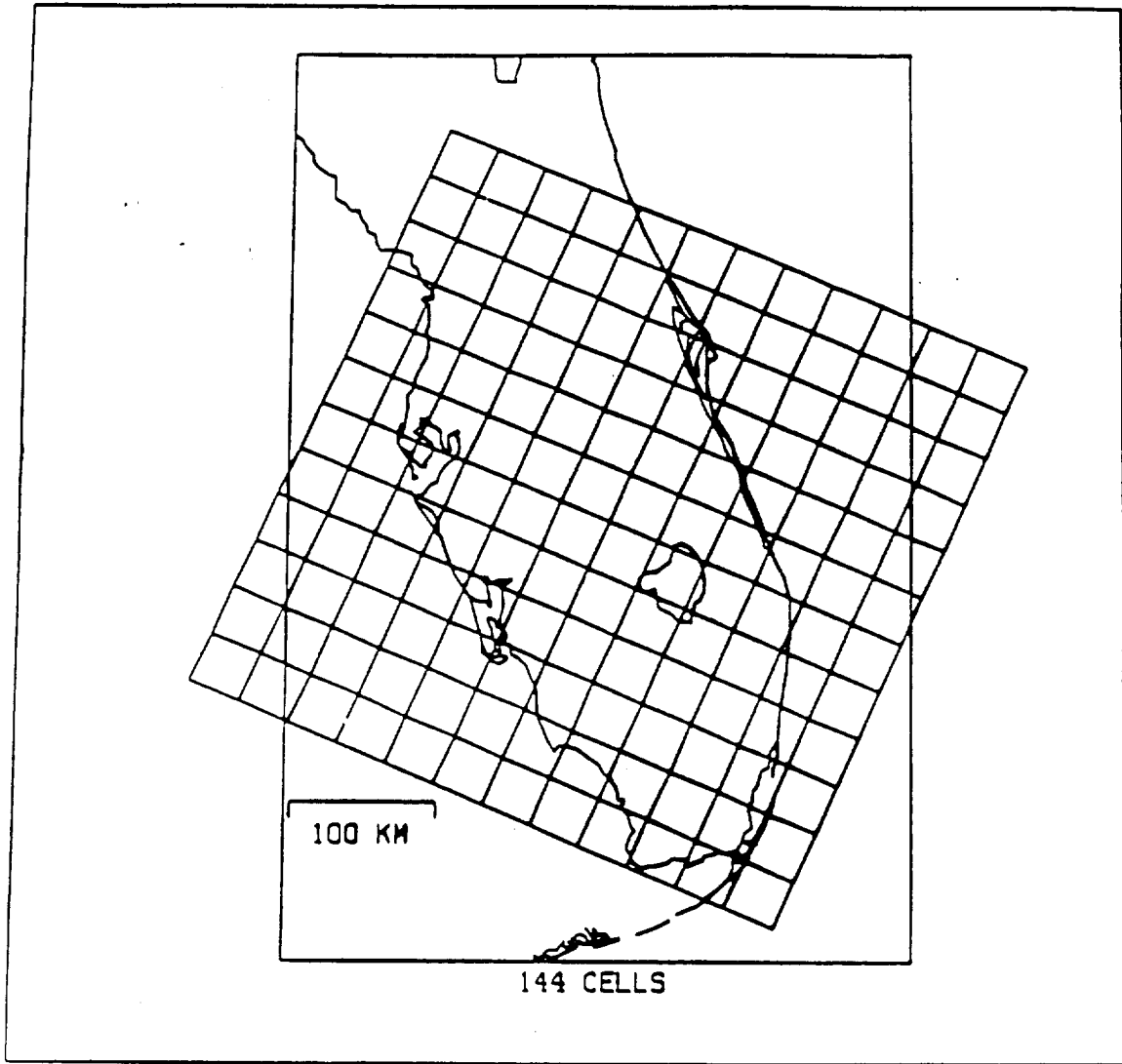
	$\times 10^4 \text{ km}^2$	$\text{mm km}^2$	$\text{mm h}^{-1}$
1700 UTC	4.65	$1.3 \times 10^4$	0.2
1800 UTC	3.50	$1.1 \times 10^4$	0.2
1900 UTC	8.38	$3.7 \times 10^4$	0.5
2000 UTC	7.06	$3.3 \times 10^4$	0.4
2100 UTC	7.24	$3.1 \times 10^4$	0.4
2200 UTC	7.10	$2.7 \times 10^4$	0.3
2300 UTC	1.11	$0.3 \times 10^4$	0.04
2400 UTC	0.55	$0.1 \times 10^4$	0.02
0100 UTC	Insignificant		
Total RER:			
1700-2400 UTC	$15.6 \times 10^4$		

TABLE 7

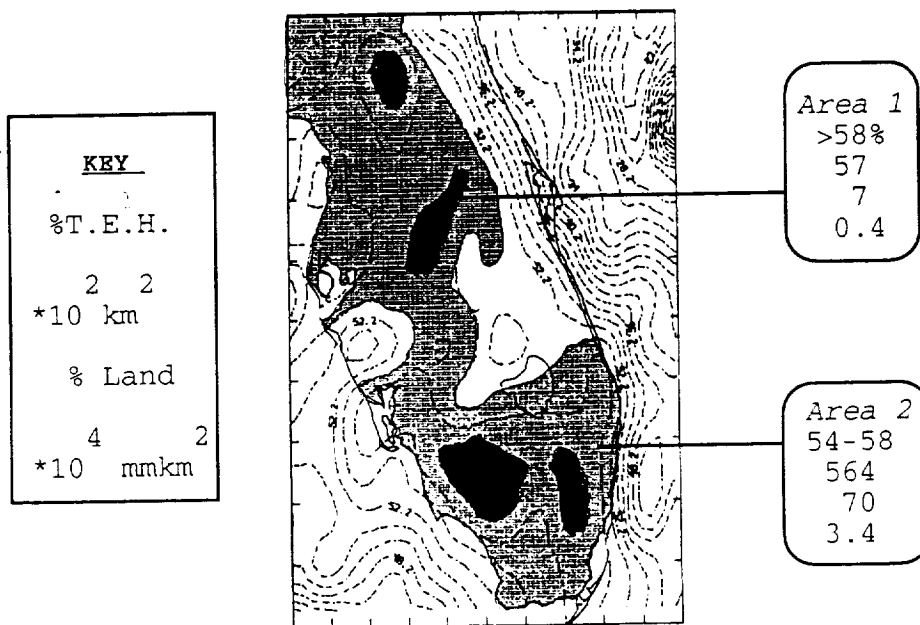
Comparison of radar estimated rainfall volume (RERV)  
and rain rates determined for Florida.

	FACE-2 Lopez et al.	MDR-ATI Analysis Present Study
Time	1978-1980	1978-1986
Period	Jun/Jul/Aug	July
Area	$3.6 \times 10^4 \text{ km}^2$	$8.0 \times 10^4 \text{ km}^2$
RERV	$10^2 - (1.64 \times 10^6 \text{ m}^3)$	$16.6 \times 10^4 \text{ mm km}^2$ $1.66 \times 10^8 \text{ mm}^3$
Mean rain rate	$3.4 \text{ mm h}^{-1}$	$2 \text{ mm h}^{-1}$





# Combined Echo Levels 3-5



KEY

%T.E.H.

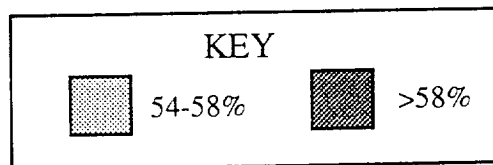
2 2

\*10 km

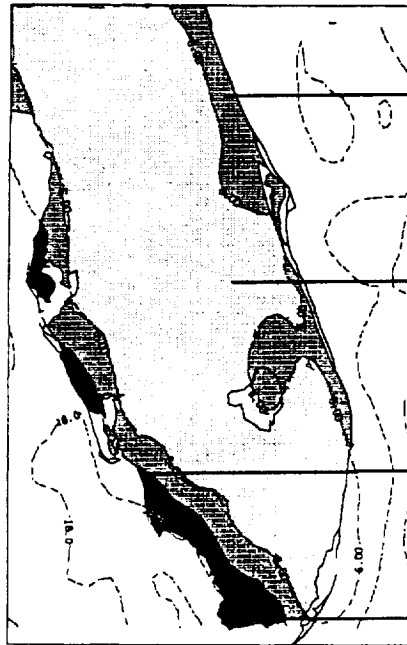
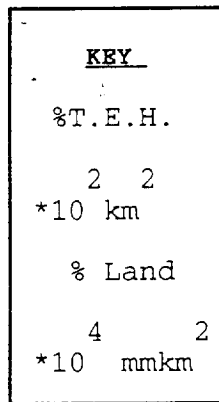
% Land

4 2

\*10 mmkm



0100-0800 GMT July

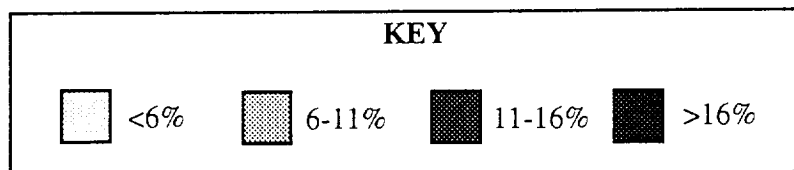


Area 2  
6-11%  
149  
18  
6.1

Area 1  
<6%  
577  
71  
8.8

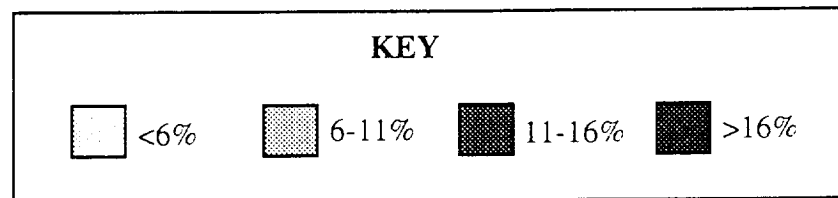
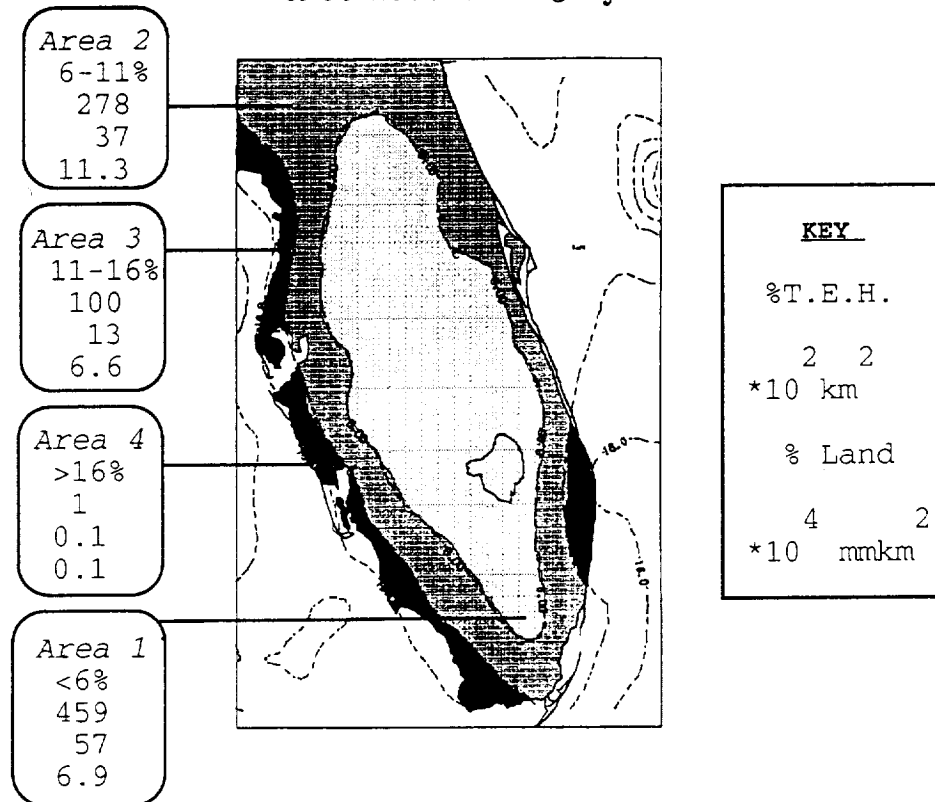
Area 3  
11-16%  
35  
4  
2.3

Area 4  
>16%  
6  
0.8  
0.6

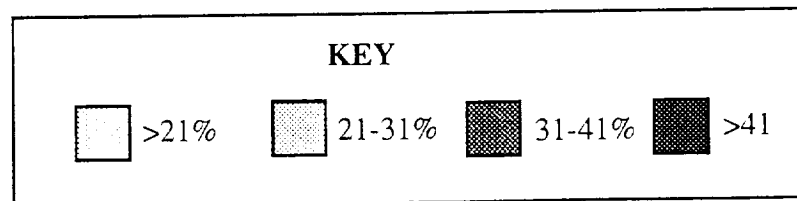
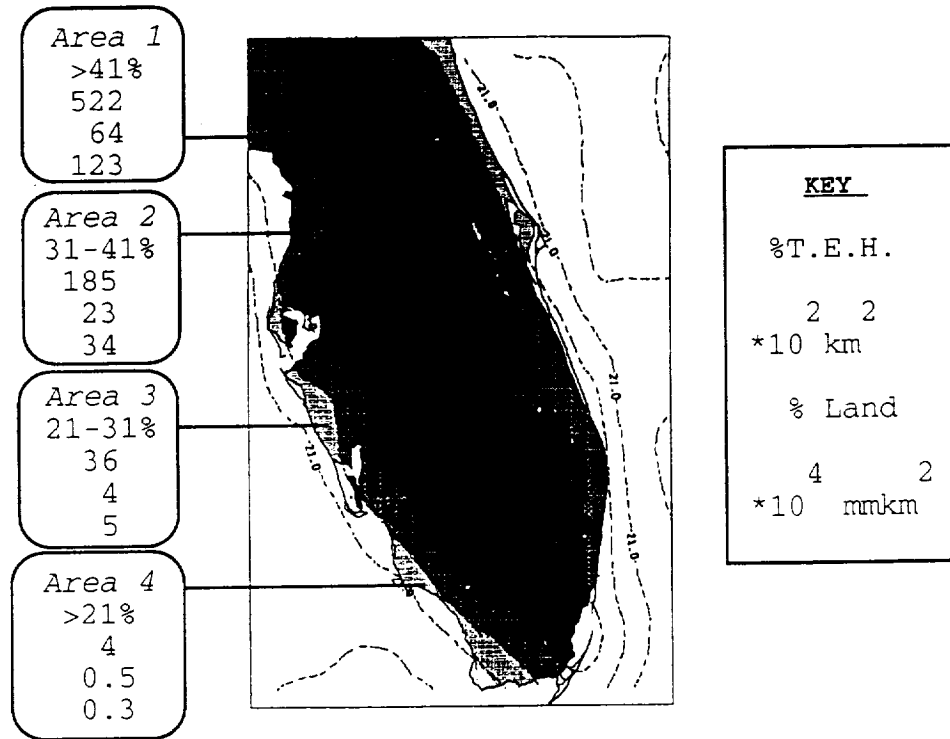




# 0900-1600 GMT July

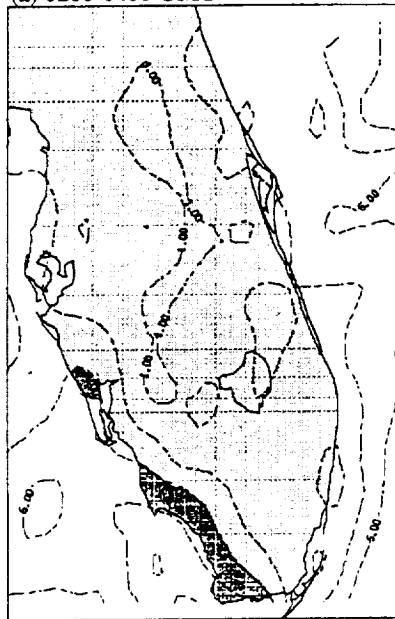


1700-2400 GMT July

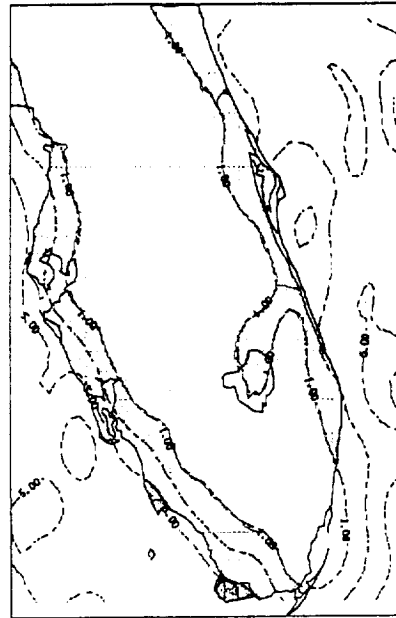


# JULY

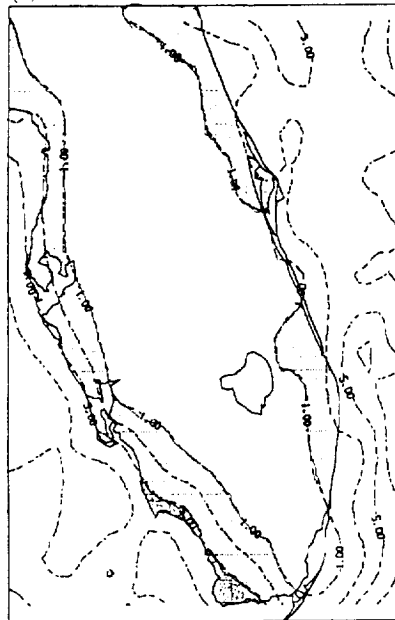
(a) 0200-0400 GMT



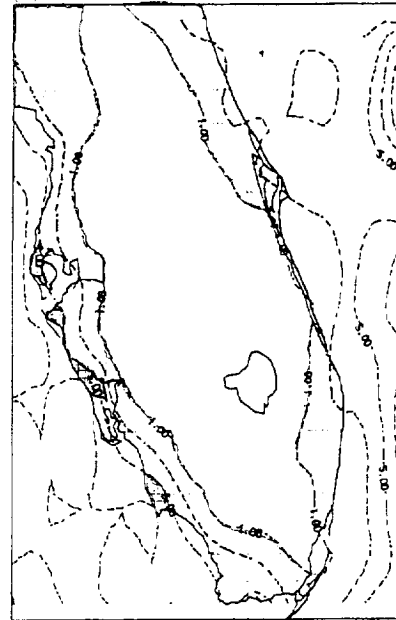
(b) 0500-0700 GMT



(c) 0800-1000 GMT



(d) 1100-1300 GMT

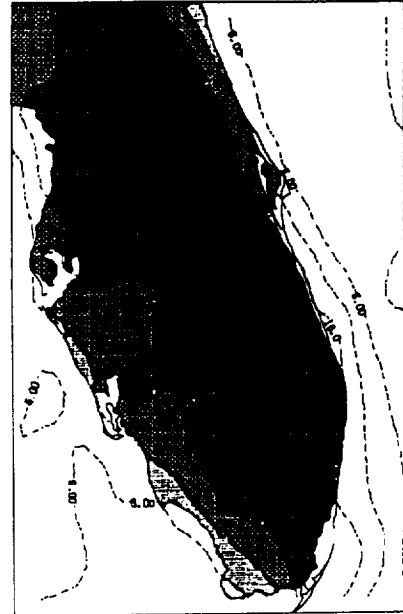


JULY

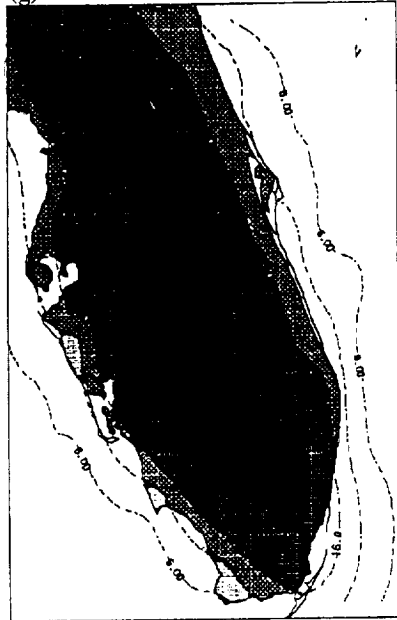
(e) 1400-1600 GMT



(f) 1700-1900 GMT



(g) 2000-2200 GMT

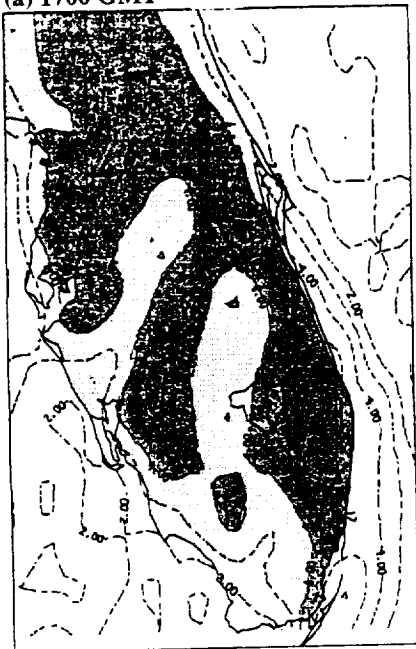


(h) 2300-0100 GMT



JULY

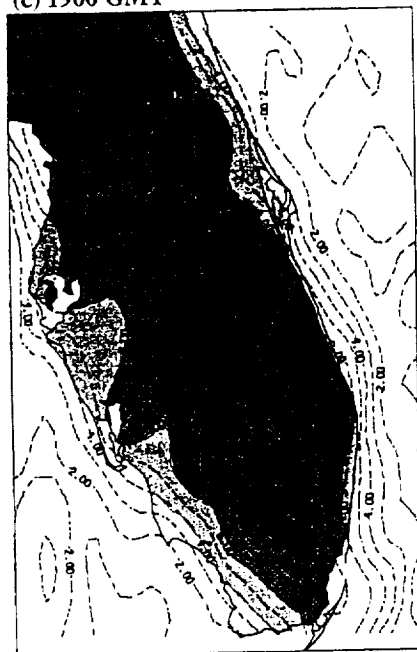
(a) 1700 GMT



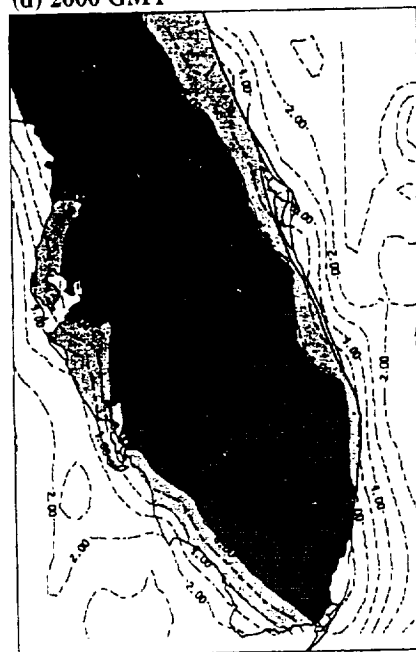
(b) 1800 GMT



(c) 1900 GMT



(d) 2000 GMT

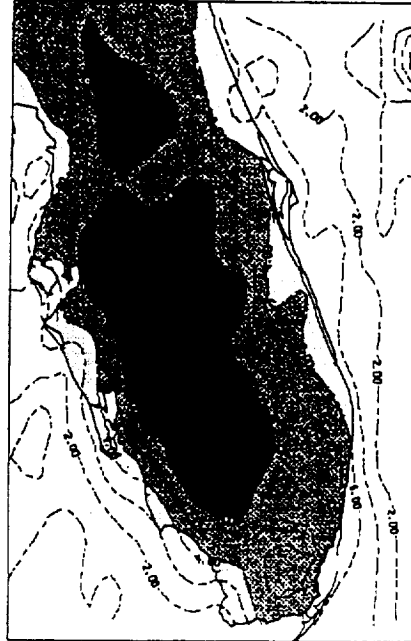


# JULY

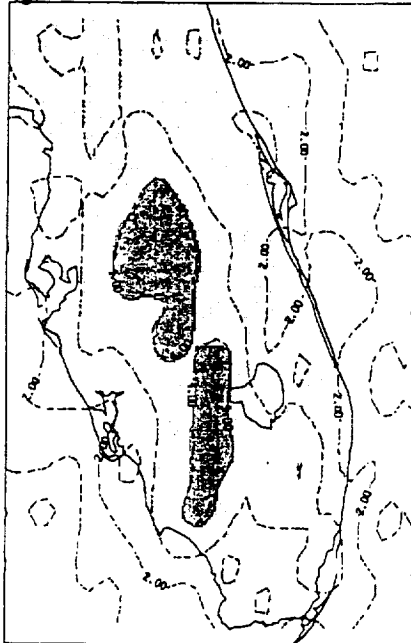
(e) 2100 GMT



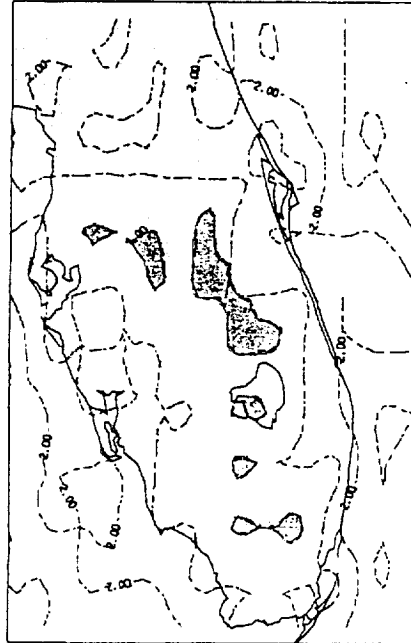
(f) 2200 GMT



(g) 2300 GMT



(h) 2400 GMT



*J. Clin.*

MEAN DIURNAL CHARACTERISTICS OF RADAR ECHOES  
OFFSHORE AND OVER THE FLORIDA PENINSULA

Claire M. Cosgrove and Michael Garstang

University of Virginia  
Department of Environmental Sciences  
Charlottesville, VA 22903

Date:

## ABSTRACT

Rainfall distributions, as detected by operational radar, are examined over the near-shore waters of the Florida peninsula. The main emphasis is on the diurnal distribution of the more intense radar echoes which are indicative of rainfall rates generally associated with convective rain. Hourly values for each month of a nine year period are analyzed. This composite approach eliminates fluctuations and extremes but retains the fundamental characteristics of the radar echoes, both over land and offshore reflecting the prevalent meteorological conditions of the region. The diurnal variation of echoes over the land is contrasted with the more steady state situation over the near-shore waters. This major difference reflects the influence of the physical coastline and the land-sea interface on the initiation, propagation and concentration of rainfall activity. The results suggest a mix of diurnal periodicities over the near-shore regions which combined give rise to a steady state over the diurnal cycle.



## 1. Introduction

The weather over the peninsula of Florida is strongly influenced by the surrounding waters of the Atlantic Ocean and the Gulf of Mexico. The effect of the water bodies is very evident during the summer months when rainfall occurrence and thunderstorm activity is largely controlled by the seabreeze circulations which develop almost daily along each coast. The importance of the double seabreeze phenomena over south Florida has been studied extensively and is well documented in the literature (Byers and Rodebush, 1948; Gentry and Moore, 1954; Frank et al., 1967; Estoque, 1962; Pielke, 1974). Subsequent studies have identified other meteorological parameters that influence the location and development of rain systems over the Florida peninsula (Gentry, 1950; Frank and Smith, 1968; Burpee, 1979; Lopez et al., 1984; Blanchard and Lopez, 1985).

Radar observations have been used in a number of studies examining rainfall and its distribution over south Florida. The main focus of this body of research has been on the frequency distribution of the echoes (Moore, 1963; Frank et al., 1967; Frank and Smith, 1968; Michaels et al., 1986). Based on these climatological studies, it was possible to identify the convective regimes based on the location and magnitude of the echo coverage (Gerrish, 1970).

Few studies have described the development of convection offshore or any interaction between the offshore activity and the land. A high correlation between the seabreeze phenomena and the

spatial and temporal variation of summer convective precipitation was detected by weather radar (Frank et al., 1967). This was based on a limited dataset of radar echoes collected at 3-hour intervals from May through August 1963. Their results indicated a day-to-night reversal of peninsula versus offshore convection.

Frank et al. (1967) calculated surface divergence for different areas of the peninsula to illustrate the diurnal cycle of convective activity. Burpee (1979) undertook a similar series of calculations for June to September of 1973-1976. He used two sets of stations, one set focused over the central portion of the peninsula while the other set extended down the west coast and out across coastal waters to the Keys. The surface divergence determined for the terrestrial region was comparable to the earlier results of Frank et al. (1967), showing a pronounced diurnal cycle with maximum convergence at 1800 UTC. (All times given in this paper are in Universal Time Conversion (UTC) whereby EST = UTC-5h.) The divergence calculated for the area encompassing the near-shore waters exhibited much weaker convergence but still depicted a diurnal signal. It would appear that the echoes over the land have strongly influenced the detection of the diurnal signal over the region encompassing coastal waters.

Subsequently, lightning activity has been analyzed in conjunction with radar data. The earliest results of lightning analysis were for the summer months of 1968 and 1969 (Hiser, 1970). His results revealed two diurnal maxima for thunderstorm

and lightning activity. The daytime maximum occurred in the southwest over the Everglades while the nocturnal maximum was to the northeast over the eastern portion of the central peninsula and the adjacent waters. Lightning and its frequency of occurrence has been studied in considerable depth at Kennedy Space Center (Jacobson and Krider, 1976; Livingston and Krider, 1978; Peipgras et al., 1982). Storm characteristics were determined but there is limited discussion on the spatial distribution of the storms, especially those offshore.

In more recent research, observations of lightning have been used to depict the diurnal pattern of summertime thunderstorms indicative of convective activity (Peckham et al., 1984; Maier et al., 1984; Lopez and Holle, 1986). The frequency and time of occurrence of lightning in the Tampa Bay area was determined from 111 storms over an 8-day period in August 1979 (Peckham et al., 1984). The majority of the storms over Tampa Bay occurred during the afternoon predominantly between 2100 and 2300 UTC while storms detected offshore mainly occurred between 0500-0700 UTC. This study was very limited in terms of sample size as only one day exhibited offshore convective activity. The work of Maier (1984) and his colleagues focused not only on the average diurnal variation of lightning in the Kennedy Space Center and Cape Canaveral areas but also considered cloud-to-ground flashes over the south Florida peninsula and the offshore waters. The lightning activity over the eastern central portion of the peninsula depicted the typical diurnal signal peaking between

2000-2130 UTC. The lightning activity over south Florida was collected during the summer months of 1978. The cloud-to-ground flashes were sampled between latitudes  $26^{\circ}$ - $27^{\circ}$ S and longitudes  $77.5^{\circ}$ - $84.5^{\circ}$ W. Again, the strong afternoon peak was apparent over the land but there was no significant peak over either the Atlantic Ocean or the Gulf of Mexico. The lightning statistics adhere closely to the thunder statistics which describe the diurnal variation over the land (Wallace, 1975). The peak activity of lightning and thunder occurrence between 1900-2200 UTC is also in agreement with rainfall statistics for the region (Schwartz and Bosart, 1979; Hamilton, 1981). Lopez and Holle (1986) depicted the spatial and diurnal variability of lightning over central Florida. They detected the highest summer activity northward from Cape Canaveral and inland to Orlando with a coastal maximum in the afternoon with some activity offshore during the night.

Further radar echo studies and lightning investigations have been undertaken in the vicinity of the Gulf Stream (Hobbs, 1987; Biswas and Hobbs, 1990; Orville, 1990; Trunk and Bosart, 1990). These investigations extended northward from Daytona Beach to Cape Hatteras where the tendency for radar echoes to cluster offshore has been frequently observed. The relevant findings from these studies are that convective clouds and precipitation are recurrent and almost stationary over the Gulf Stream off the coast of the Carolinas during winter months (Biswas and Hobbs, 1990). The frequency of lightning flashes detected at the

earth's surface from mid-January to mid-March 1986, were more frequent at the lower latitudes, i.e., both over the Florida peninsula and extending offshore (Fig. 1). The effect of the Gulf Stream is very apparent with the increase in lightning flashes detected along this thermal gradient. Based on the National Weather Service (NWS) hourly radar observations, the extent of rainfall coverage off the southeast coast was discernible (Trunk and Bosart, 1990). Trunk and Bosart mapped the radar intensity levels 1, 3 and 5 where level 1 refers to light rainfall, level 3 is probably thunderstorm cells and level 5 corresponds to very heavy convective rains with possible hail. At Daytona Beach, the diurnal signal overland of radar intensity level 3, dominates with a peak in mid-morning (1435 UTC) and a secondary maximum in the mid-to-late afternoon between 2035-2335 UTC (Fig. 2). The occurrence of echoes offshore is less frequent. The peak period for echoes offshore is at 1435 UTC then dropping off until the early evening (2335 UTC). Another peak occurs at midnight (0535 UTC) and completely diminishes in the early morning hours (0835 UTC). The difference between the offshore and onshore curves was assessed using a Student t-test. The difference between the echo density curves was significant at the 0.05 level for both intensity levels at both locations.

This present study focuses on the occurrence of radar echoes offshore as well as over the greater portion of the peninsula. The echo levels analyzed are indicative of strong to intense rainfall. The diurnal progression both over land and near-shore

waters are discussed for the two main seasons, summer and winter, and the transition months between these seasons.

## 2. Data Source

Manually digitized radar (MDR) data are recorded by personnel at the National Weather Service (NWS) radar sites. In Florida, the NWS radars are located at Daytona, Miami, Tampa, West Palm Beach and Key West. Figure 3 shows the echo coverage for the 185 km range from each radar. In general, the radar information is considered reliable within 200 km of the coast (Trunk and Bosart, 1990). The Daytona, Miami and Tampa radars are WSR-57 models while the WSR-74S model is located at the other two sites. Both models are S-band radar and operate continuously, scanning at an elevation angle of  $0.5^\circ$ . The return signals are automatically processed by a digital video integrator and processor (DVIP) unit to produce levels of echo intensity called VIP levels. These intensity levels are objectively recorded in each grid cell following the procedures set out in the Federal Meteorological Handbook No. 7 (1987). Each grid cell represents an area 1/16th of the National Meteorological Center's (NMC) operational Limited Fine Mesh (LFM) Model grid boxes (about  $34 \text{ km}^2$ ). Even with these standard procedures, there is a systematic bias in the data tending to overestimate the areal coverage. The maximum level of intensity, regardless of areal extent, is allocated to each grid cell. The recording procedure identifies the area of maximum precipitation but does not reflect the persistence of the echoes nor detail the areal coverage of

the echoes.

The echo intensities correspond to radar reflectivities: VIP L1 ( $< 30$  dBz), VIP L2 (20-40 dBz), VIP L3 (41-46 dBz), VIP L4 (47-49 dBz), VIP L5 (50-57 dBz) and VIP L6 ( $> 57$  dBz). These echo levels also have corresponding rainfall rates. In convective-type rain, VIP levels 3, 4 and 5 correspond to approximate rainfall rates of 28-56 mm h<sup>-1</sup>, 56-114 mm h<sup>-1</sup>, and 114-180 mm h<sup>-1</sup>, respectively. For stratiform-type rain the same VIP levels correspond to rainfall rates of 13-25 mm h<sup>-1</sup>, 25-51 mm h<sup>-1</sup>, and 51-127 mm h<sup>-1</sup>.

A 12 x 12 array of grid cells was extracted from the NWS radar data source tapes. Each grid cell covered an area of approximately 34 km on a side in this region. The total area of echoes analyzed was in the order of  $1.7 \times 10^5$  km<sup>2</sup>. This array covered the Florida peninsula in a diamond configuration and extended over the adjacent waters (Fig. 4). The range of offshore waters monitored was from 30 km off the southeast coast to over 150 km both southwest and northeast of the land. The period of investigation was from 1978 to 1986, inclusive. Data was obtained on an hourly basis over the nine year period with an overall loss of 9% of the data during the study period.

### 3. Analysis of Radar Echoes

The occurrence of each echo level as a percentage of the monthly total echo hours (TEH) was determined. These values were then compared as a series of echo level combinations (Table 1). From this table, it is apparent that the combination of VIP L3,

L4 and L5 is most representative of intense rainfall. This echo combination occurs 30-35% of the TEH during the winter months, 40-45% of the transition months and nearly 50% of the TEH in the summer months. The addition of L6 echoes would have increased the computational requirements but would not necessarily add to the understanding of rainfall variability over the region since L6's occur less than or equal to 1% of the TEH in any one calendar month. The greater portion of the more intense echoes are attributed to L3 and L4 echoes. Level 1 echoes were not used at any stage in the analysis as this level equates with light rainfall which if measured by raingauges, would be referred to as "trace" rainfall.

Based on these results, and the results from previous studies, it was decided to treat levels 3, 4 and 5 as being representative of convective rain. According to Trunk and Bosart (1990), level 3 echoes are associated with thunderstorms in convective systems and possibly bright-band activity in heavier stratiform precipitation events while level 5 echoes are more frequently associated with very heavy convective rain and hail. Echo intensity levels, L2 to L6, were treated as the total rainfall.

To delineate between rainfall over land and that over coastal waters, the MDR database of 144 grid cells was subdivided. The map of radar coverage (Fig. 3) was placed over the grid cell array (Fig. 4) to identify those cells which lay within the 100 km range of the shoreline. This resulted in three



subsets: 70 cells over the land, 53 cells over coastal waters and a remaining 21 cells that were considered to be at the limits of the radar range for applying the data to hydro-meteorological interpretation (Fig. 5). Along the coastal margins, grid cells were considered offshore if half or more of the area was water.

#### 4. Results of Land-Sea Echo Comparison

##### a. Seasonal Variation

The mean number of TEH (L2-L6) was calculated for each month for both "over the land" and the "near shore" subsets (Table 2). The majority of the radar echoes were observed between June and September. Echoes were more prevalent over the land than near-shore from February through to August. By September, the occurrence of echoes over the water was as frequent as over the land. Echoes were more frequent over the near shore regions during the remainder of the year. The difference between the number of near shore and over land echo hours as shown in Table 2a is more informative. From September through to April, the difference in TEH per month ranged between -6 and +7 hours. In May, there were 14 more echo hours over land. This difference increased during the summer to between 23-34 hours. In terms of the echo hours as percentages of the maximum possible hours, 67% of the echoes occur over the land from June to September compared with 54% along the coastal waters (Table 2b). During May, October and November, 22% of the echoes occurred over both the land and offshore. This table shows that summer months, June to September, are the more important ones for indepth analysis.

There is a strong seasonal variation both over land and the near shore waters. However, the variation between echoes over land and water is insignificant for eight months of the year.

Table 2 also implies that rainfall over the surrounding waters is almost as significant in amount as that measured over the land. The unknown factors which would modify this inference are the duration of the echoes and whether rain actually reached the surface. When comparing the mean number of TEH over the land with those offshore, it is interesting to note that, in June, nearly 18% more echoes occurred over the land than coastal waters. This decreased to 13% more echoes over the land in July, 9% more in August and finally diminishing to only a 1% difference in September. The most significant difference in rainfall over these two regions should be observed in June with the least variation in September.

b. Diurnal Cycle in September

During the summer months, the most frequent echoes over the land occurred between 1500 and 0100 UTC ( $> 20$ ) while the least frequent occurrence of echoes was between 0400-1300 UTC ( $< 10$ ) (Table 3). The afternoon peak formed between 1800 and 2000 UTC ( $> 50$ ) with the maxima at 1900 and 2000 UTC ( $> 70$ ) in July and August. This equated with over 50% of the echoes depicting strong to intense rain during the peak rain periods (Table 4). Table 4 relates the occurrence of level 3-5 echoes as a percentage of all rainfall based on echo levels 2-6. Echo occurrence is minimum during the pre-dawn-morning period (Table

3). However, 30-40% of those echoes recorded represent heavy rainfall (Table 4). In contrast with this, the pattern of occurrence of radar echoes over the coastal waters is fairly steady throughout the diurnal cycle (Table 5). This table reflects the strong seasonal variation but virtually no diurnal variation. This translates to over 40% of the rain period during June through October as having strong to very intense rainfall rates in the near shore region (Table 6).

The variability over a diurnal cycle is clearly depicted in the monthly graphs (Figs. 6 to 8). In these graphs, heavy to very intense rain (L3-L5) are presented as a percentage of the total diurnal echo hours for each hour interval. The term, total diurnal echo hours (TDEH), refers to the mean number of echo hours that are recorded during a 24-h period for each grid cell. During the summer months, echoes reflecting L3-L5 rainfall rates occur less than 8% of the TDEH in any one hour period over the land. This percentage decreases to < 5% for May and October (Fig. 8), to < 3.5% during April and November and < 2.5% for the winter months (Fig. 7). In contrast with this, the occurrence of convective-type echoes over the coastal waters are recorded as less than 3% of the TDEH in summer (Fig. 6). This drops to around 2% in May and October, to 1.5-2% in April and November (Fig. 8) and between 1-1.5% in winter (Fig. 7).

During the summer months over land, the general trend reveals the preferred time for convective activity (Fig. 6). Convection develops in the late morning (1500 UTC) (2% of TDEH),

peaks in the mid-afternoon (1900-2100 UTC) (5.5-7% of TDEH), then dies off in the early evening (2300-0100 UTC) (2% of TDEH). Whereas rainfall activity offshore is fairly steady with a lower frequency of occurrence throughout the diurnal cycle (2% of TDEH).

Winter rainfall offshore shows a much more varied pattern (Fig. 7). In December, there is a discernible diurnal cycle over both the land and near shore waters from the mid-afternoon (1900-2200 UTC) (1.75% of TDEH). The strength of the diurnal signal over land is diminishing. It is less intense and of shorter duration (1800-2000 UTC). It peaks at 2100 UTC (2.5% of TDEH). By January, the peak rainfall offshore is earlier in the day reaching a maximum just after dawn (1200 UTC) (1.75% of TDEH). The offshore echoes are more prevalent than over the land and are typically nighttime to early-late morning occurrences (0400-1600 UTC) (1.5% of the TDEH). Echoes over the land have continued to diminish considerably (0100-1000 UTC) (1% of TDEH). Any activity tends to be in the early morning to late afternoon (1200-1900 UTC) (1.5% of TDEH) with a maximum in the early afternoon. In February, there are two minor peaks of activity over the coastal waters, during the night and then at dawn. Activity offshore reaches its maximum in the middle of the afternoon (2000-2100 UTC) (2% of TDEH). Activity over the land is almost non-existent during the first half of the day (< 1% of TDEH). Noticeable activity begins from 1500 UTC onwards. This activity continues to increase throughout the afternoon peaking in the late

afternoon at 2200 UTC (2.3% of TDEH). February does appear to be a more active month in comparison to the other winter months. The diurnal trend is similar to that of summer. March has a less defined diurnal cycle peaking between 1900-2200 UTC (2.3-2.5% of TDEH) over the land while near shore activity is relatively steady (1.5% of TDEH).

Of the transition months, May and October have more defined diurnal signals than either April or November (Fig. 8). There is virtually no activity over land from midnight through early morning. Radar echoes appear from 1600 UTC through to 2300 UTC. A maximum of 4.5% of TDEH occurs at 2100 UTC. In May and October, the trend adheres very closely to that of the summer months. In April and November, the significant difference is in the decrease of occurrence of the more intense echoes in the afternoon period. The signal peaks at 3.5% of TDEH between 0200-2100 UTC. Echo occurrence over the coastal waters is steady, averaging 2% of TDEH in May and October. In April, the frequency of these echoes fluctuates between 1.5-2% of TDEH with a noticeable absence of signal between 0100-0400 UTC. During November, the signal over the water averages 1.5% of TDEH from 0100-1700 UTC. Then there is a gentle increase during the afternoon until 2200 UTC.

In general, the winter signals are much weaker in comparison with either the summer season or any of the transitional months. January tends to have the weakest diurnal signal over the land and the most atypical signal near shore. Echoes over the near

shore region are more prevalent during the night reaching a maximum at dawn. February is unusual in that it tends towards a summer pattern but on a reduced scale both over land and offshore. The diurnal signal near shore, although weak, is discernible with increased activity between 1800-2100 UTC. This afternoon peak in the near shore activity could be due to a mix of onshore and offshore cycles during the winter months. This signal is in agreement with the results of Trunk and Bosart (1990).

During the summer months, the diurnal variation of radar echoes is very pronounced over the land. Maximum echo coverage occurs through the afternoon hours until mid-evening with minimum echo coverage during the late night/early morning. The radar echoes detected in the near shore region exhibit a steady state with no clearly defined variation in the diurnal signal. These results compliment the work of Maier et al. (1984).

## 5. Discussion and Conclusions

The use of manually digitized radar data from the operational NWS radar network has provided a means of assessing rainfall activity both over land and the offshore waters of the peninsula of Florida during the wet and dry seasons. This investigation uses a radar dataset from a much longer time span than has been undertaken in the previous studies. Compositing over the nine year period may have lessened the contrast in the radar echo coverage between the land and water. However, the diurnal variation is still discernible, thus providing a set of

reference information depicting the basic characteristics of the temporal variability of radar echoes over the land and coastal waters.

The question of how well the results show the variation between the onshore and offshore convective activity is not fully resolved. The diurnal signal for the near shore waters may not be as pronounced as might be anticipated further offshore over the core of the Gulf Stream. The subset of near shore echoes were taken from both sides of the peninsula. Compositing the echoes from the Gulf of Mexico and the Atlantic Ocean may have suppressed significant features.

This study shows that the well established modulation of convection over the land rapidly decays over the near shore waters. Based on the diurnal variation of radar echoes over the land, there is a tendency for maximum echo coverage throughout the afternoon into the early evening with minimum echoes from midnight until dawn. There is reduced diurnal activity over the land in winter. The frequency of radar echoes over the coastal waters, however, are steady throughout the diurnal cycle. This lack of near shore diurnal signal reflects the interface between the daytime land maximum and the offshore nighttime maximum. There is slight enhancement of the diurnal activity over the near shore waters in winter. This enhancement may be due in part to the presence of the warmer Gulf Stream waters enhancing the temperature differential between the land and sea during winter. The more intense echoes (L3-L5), occur on average, 17% of the

time during the summer months over the land compared with 14% of the time offshore. This implies that there may be significant amounts of rainfall over the near shore waters comparable to that occurring over the land. The greatest difference in rainfall occurrence between land and surrounding water should occur in June with the least difference in September. This implies that single-cell and small convective systems are responsible for the rain in early summer compared with larger more complex systems in late summer.



## Acknowledgements

This work has been sponsored by a grant from NASA/Goddard Space Flight Center. Results presented in this paper are from Ms. Cosgrove's M.S. thesis.

## References

- Biswas, K.R. and P.V. Hobbs, 1990: Lightning over the Gulf Stream. Geophys. Res. Letters, 17, 941-943.
- Blanchard, D.O. and R.E. Lopez, 1985: Spatial patterns of convection in south Florida. Mon. Wea. Rev., 113, 1282-1299.
- Burpee, R.W., 1979: Peninsula-scale convergence in the south Florida sea breeze. Mon. Wea. Rev., 107, 852-860.
- Byers, H.R. and H.R. Rodebush, 1948: Causes of thunderstorms of the Florida peninsula. J. Meteor., 5, 275-280.
- Estoque, M.A., 1962: The sea breeze as a function of the prevailing synoptic situation. J. Atmos. Sci., 19, 244-250.
- Frank, N.L., P.L. Moore and G.E. Fisher, 1967: Summer shower distribution over the Florida peninsula as deduced from digitized radar data. J. Appl. Meteor., 6, 309-316.
- \_\_\_\_\_ and D.L. Smith, 1968: On the correlation of radar echoes over the various meteorological parameters. J. Appl. Meteor., 7, 712-714.
- Gentry, R.C., 1950: Forecasting local showers in Florida during the summer. Mon. Wea. Rev., 78, 41-49.
- \_\_\_\_\_ and P.L. Moore, 1954: Relation of local and general wind interaction near the sea coast to time and location of airmass showers. J. Meteor., 11, 507-511.
- Gerrish, H.P., 1970: Temporal variation in echo coverage as a function of tropical convective regime in south Florida. Proc. 14th Conf. Radar Meteor., Tucson, AZ, November 17-20,

pp. 425-428.

Hamilton, K., 1981: A note on the observed diurnal and semi-diurnal rainfall variations. J. Geophys. Res., 86, 12122-12126.

Hiser, H.W., 1970: Thunderstorm studies in south Florida. Proc. 14th Conf. Radar Meteor., Tucson, AZ, November 17-20, pp. 309-312.

Hobbs, P.V., 1987: The Gulf Stream rainband. Geophys. Res. Letters, 14, 1142-1145.

Jacobson, E.A. and E.P. Krider, 1976: Electrostatic field charges produced by Florida lightning. J. Atmos. Sci., 33, 103-117.

Livingston, J.M. and E.P. Krider, 1978: Electric fields produced by Florida thunderstorms. J. Geophys. Res., 83, 385-401.

Lopez, R.E., D.O. Blanchard, D. Rosenfeld, W.L. Hiscox and M.J. Casey, 1984: Population characteristics, development processes and structure of radar echoes in south Florida. Mon. Wea. Rev., 112, 56-75.

\_\_\_\_\_ and R.L. Holle, 1986: Diurnal and spatial variability of lightning activity in northeastern Colorado and central Florida during summer. Mon. Wea. Rev., 114, 1288-1312.

Maier, L.M., E.P. Krider and M.W. Maier, 1984: Average diurnal variation of summer lightning over the Florida peninsula. Mon. Wea. Rev., 112, 1134-1140.

Michaels, P.J., R.A. Pielke, J.T. McQueen, and D.E. Sappington, 1986: Composite climatology of Florida summer

- thunderstorms. Mon. Wea. Rev., 115, 2781-2791.
- Moore, P.L., 1963: A radar study of shower activity associated with the sea breeze. Proc. 10th Weather Radar Conf., Washington, D.C., April 22-25, pp. 8-12.
- Orville, R.E., 1990: Winter lightning along the east coast. Geophys. Res. Letters, 17, 713-715.
- Peckham, D.W., M.A. Uman and C.E. Wilcox, Jr., 1984: Lightning phenomenology in the Tampa Bay area. J. Geophys. Res., 89, 11,789-11,805.
- Pielke, R.A., 1974: A three-dimensional model of the sea breeze over south Florida. Mon. Wea. Rev., 102, 115-139.
- Piepgras, M.V., E.P. Krider and C.B. Moore, 1982: Lightning and surface rainfall during Florida thunderstorms. J. Geophys. Res., 87, 11,193-11,201.
- Schwartz, B.E. and L.F. Bosart, 1979: The diurnal variability of Florida rainfall. Mon. Wea. Rev., 107, 1535-1545.
- Trunk, T.J. and L.F. Bosart, 1990: Mean radar echo characteristics during project GALE. Mon. Wea. Rev., 118, 459-469.
- Wallace, J.M., 1975: Diurnal variations in precipitation and thunderstorm frequency over the conterminous United States. Mon. Wea. Rev., 103, 406-419.

### List of Figures

- Fig. 1. Isopleths of the average number of lightning flashes to the earth's surface per day during the period 15 January through 15 March 1986. The mean location of the Gulf Stream was within the dashed lines. (After Biswas and Hobbs, 1990.)
- Fig. 2. Echo density as a function of time (UTC) for Daytona Beach for the period 15 January-15 March 1986. Solid (dashed) lines denote offshore (onshore) radar echoes. The  $\alpha$  symbol refers to  $1-\beta$ , where  $\beta$  is the level of significance for a Student's t-test on the difference of the onshore versus offshore means. (After Trunk and Bosart, 1990.)
- Fig. 3. Range of the radar scope over the peninsula of Florida. The range of the radar is depicted at 185 km (100 nmi).
- Fig. 4. The manually digitized radar (MDR) array of 144 grid cells over the Florida peninsula.
- Fig. 5. A 12x12 array of MDR grid cells covering the peninsula of Florida. Seventy cells over the land, 53 cells over coastal waters and a remaining 21 cells considered beyond the limits of the radar range.
- Fig. 6. The diurnal distribution of convective rain as a percentage of the total rainfall during the summer months.
- Fig. 7. As in Fig. 6 except for the winter months.
- Fig. 8. As in Fig. 6 except for the transition months.

TABLE 1. Monthly occurrence of each MDR echo level as a percentage of total echo hours (TEH).

	ECHO LEVELS					
	L2	L3	L4	L5	L6	L3/4/5
January	70	17	10	3	0	30
February	68	18	10	4	0	32
March	64	20	11	5	1	36
April	60	19	13	7	1	39
May	54	21	15	9	1	45
June	53	20	18	9	1	47
July	50	21	18	10	0	49
August	51	22	17	9	0	48
September	54	22	16	7	0	45
October	61	21	13	5	0	39
November	69	19	10	2	0	31
December	70	18	8	3	0	29

TABLE 2. Comparison of echoes for the whole data set, and the land and near shore subsets: (a) mean number of total echo hours for each month for the entire dataset (144 cells), over land (70 cells) and near shore (53 cells) and the difference between the number of echoes over land and near shore; (b) mean number of total echo hours as a percentage of of the maximum possible hours.

---

---

(a) Mean number of total echo hours

	JAN	FEB	MAR	APR	MAY	JUN	JUL	AUG	SEP	OCT	NOV	DEC
MDR												
Data Set												
(144)	28	33	32	29	49	90	104	120	102	60	41	29
Land												
( 70)	30	38	37	34	61	114	124	138	109	62	41	30
Near Shore												
(53)	30	33	30	28	47	80	95	115	107	68	47	33
$\Delta$												
(70-53)	0	5	7	6	14	34	29	23	-2	-6	-6	-3

---

(b) Mean percentage of maximum possible hours

	JAN	FEB	MAR	APR	MAY	JUN	JUL	AUG	SEP	OCT	NOV	DEC
MDR												
Data Set												
(144)	4	5	4	4	7	13	14	16	14	8	6	4

Table 2 (cont.)

---

---

	JAN	FEB	MAR	APR	MAY	JUN	JUL	AUG	SEP	OCT	NOV	DEC
<b>Land</b>												
(70)	4	6	5	5	8	16	17	19	15	8	6	4
<b>Near Shore</b>												
(53)	4	5	4	4	6	11	13	15	15	9	7	4

---



TABLE 3. The seasonal and diurnal distribution of the occurrence of echo levels 3-5 over the land (70 cells).

TIME (UTC)	JAN	FEB	MAR	APR	MAY	JUN	JUL	AUG	SEP	OCT	NOV	DEC
0000	3	5	7	7	16	32	32	36	25	13	6	4
0100	3	5	6	5	11	23	20	23	18	10	5	3
0200	3	4	4	5	7	14	13	15	13	7	4	3
0300	2	4	4	3	5	9	9	10	10	5	4	3
0400	2	3	4	3	4	7	5	8	8	5	3	3
0500	3	2	4	3	3	6	5	6	8	4	3	3
0600	3	2	4	2	3	5	4	5	6	4	3	2
0700	2	2	3	3	4	5	4	6	7	3	3	2
0800	3	3	4	3	4	6	4	6	6	3	3	2
0900	3	3	4	3	4	6	4	7	6	3	3	3
1000	3	2	3	3	5	6	5	6	4	3	2	2
1100	2	2	2	3	4	4	4	5	3	2	1	1
1200	3	3	4	4	5	7	6	7	6	4	3	3
1300	3	3	5	4	5	8	6	9	7	4	3	3
1400	3	3	5	4	7	12	11	13	9	4	3	3
1500	4	4	5	5	9	20	20	23	15	6	4	3
1600	3	5	6	7	14	31	35	36	24	9	6	3
1700	4	6	6	7	18	42	48	52	33	15	6	4
1800	4	6	6	8	24	52	65	64	47	18	9	5
1900	4	7	8	10	26	59	73	73	53	24	10	5

Table 3. (cont.)

TIME (UTC)	JAN	FEB	MAR	APR	MAY	JUN	JUL	AUG	SEP	OCT	NOV	DEC
2000	4	7	8	10	27	64	72	76	53	26	11	6
2100	4	7	8	11	27	58	67	72	53	25	10	6
2200	3	7	8	9	23	46	59	63	40	19	9	5
2300	2	6	6	7	14	28	32	32	21	7	4	2

TABLE 4. The seasonal and diurnal distribution of convective rainfall as a percentage of the total rainfall over the land (70 cells).

TIME (UTC)	JAN	FEB	MAR	APR	MAY	JUN	JUL	AUG	SEP	OCT	NOV	DEC
0000	31	37	39	43	50	47	46	48	46	43	35	29
0100	26	37	40	43	44	44	43	43	44	39	29	27
0200	25	33	34	41	42	42	44	40	39	35	27	27
0300	29	32	35	35	37	40	41	40	37	34	25	28
0400	25	28	31	39	37	40	40	42	40	31	26	29
0500	31	25	35	34	37	41	41	35	37	25	26	30
0600	31	24	35	34	33	41	42	39	34	25	27	24
0700	28	20	31	34	38	41	40	41	34	23	28	26
0800	30	26	34	33	39	40	33	37	35	27	31	24
0900	28	29	31	35	38	40	37	40	34	28	25	30
1000	31	25	33	36	43	39	42	36	30	26	25	31
1100	35	27	31	43	45	39	39	35	31	22	25	26
1200	32	29	31	41	41	39	34	37	34	32	26	29
1300	26	30	39	34	38	42	35	43	37	29	27	31
1400	31	31	41	38	42	43	46	48	39	34	28	31
1500	33	32	40	38	45	46	50	52	43	34	27	32
1600	31	36	36	45	51	47	56	54	48	34	32	32
1700	33	40	39	43	52	48	60	56	51	39	32	32
1800	35	38	41	42	57	51	62	60	57	40	35	33
1900	34	39	43	47	56	49	63	62	58	47	37	32

Table 4. (cont.)

TIME (UTC)	JAN	FEB	MAR	APR	MAY	JUN	JUL	AUG	SEP	OCT	NOV	DEC
2000	35	36	39	47	57	51	61	62	56	47	41	33
2100	35	36	38	48	56	50	58	58	55	47	39	34
2200	33	38	39	46	53	47	57	56	50	47	39	35
2300	28	37	40	44	53	47	52	51	47	42	34	27

TABLE 5. The seasonal and diurnal distribution of the occurrence of echo levels 3-5 near shore (53 cells).

TIME (UTC)	JAN	FEB	MAR	APR	MAY	JUN	JUL	AUG	SEP	OCT	NOV	DEC
0000	3	4	4	5	9	17	19	23	22	14	8	4
0100	3	3	4	4	8	15	19	21	22	13	7	4
0200	3	4	4	4	7	15	16	19	21	11	7	3
0300	3	3	4	3	7	13	15	17	19	10	6	4
0400	3	4	4	2	7	13	14	16	16	10	6	3
0500	3	3	3	3	6	13	13	17	16	10	6	3
0600	4	3	4	3	7	12	14	17	15	10	6	4
0700	3	3	4	3	7	13	15	16	15	10	6	4
0800	3	3	4	4	8	14	16	18	15	9	5	3
0900	4	3	4	5	9	14	17	20	15	10	6	4
1000	3	2	4	4	8	13	15	18	13	8	4	3
1100	3	2	3	4	6	8	11	15	10	6	2	2
1200	4	3	4	4	8	13	19	23	16	10	6	4
1300	4	3	4	5	8	13	17	23	17	10	5	4
1400	4	3	4	5	7	13	18	22	17	10	6	4
1500	4	4	4	4	7	14	17	21	17	9	6	4
1600	4	4	4	5	7	13	18	22	18	10	6	4
1700	3	4	4	5	7	14	18	22	20	10	6	4
1800	4	5	4	5	8	15	20	24	22	11	6	4
1900	3	5	5	5	8	16	19	23	22	10	6	5

Table 5. (cont.)

TIME (UTC)	JAN	FEB	MAR	APR	MAY	JUN	JUL	AUG	SEP	OCT	NOV	DEC
2000	3	5	5	5	9	18	21	23	24	12	7	5
2100	3	5	4	5	10	17	21	24	24	13	7	5
2200	3	5	4	5	10	16	20	24	23	11	7	5
2300	3	4	4	4	6	12	15	15	15	7	5	3

TABLE 6. The seasonal and diurnal distribution of convective rainfall as a percentage of the total rainfall near shore (53 cells).

TIME (UTC)	JAN	FEB	MAR	APR	MAY	JUN	JUL	AUG	SEP	OCT	NOV	DEC
0000	30	30	35	37	46	49	45	47	45	42	35	26
0100	30	31	34	39	45	44	47	46	47	42	32	26
0200	28	31	33	39	39	45	44	43	45	40	32	25
0300	28	31	37	32	43	45	45	43	45	38	32	26
0400	29	37	37	29	44	46	45	43	44	39	32	31
0500	33	34	32	36	42	47	45	46	43	37	33	29
0600	35	30	33	38	40	45	46	45	43	38	34	31
0700	38	30	35	36	42	47	46	43	42	38	31	31
0800	34	28	36	38	44	46	48	43	42	39	30	26
0900	35	31	35	42	44	45	44	45	43	40	32	29
1000	34	28	41	43	46	44	45	44	43	41	27	30
1100	35	29	34	45	47	42	45	47	42	41	32	28
1200	37	34	34	35	43	45	46	47	44	41	28	31
1300	35	31	36	38	44	45	46	47	48	43	30	34
1400	30	29	37	39	39	43	45	44	47	42	34	32
1500	35	34	37	37	40	42	44	43	44	40	33	33
1600	32	34	36	41	38	40	43	45	45	42	31	32
1700	31	33	38	42	38	42	43	45	46	38	34	30
1800	33	36	39	40	39	42	46	44	46	38	31	30
1900	32	34	39	41	42	42	43	42	46	34	31	35

Table 6. (cont.)

TIME (UTC)	JAN	FEB	MAR	APR	MAY	JUN	JUL	AUG	SEP	OCT	NOV	DEC
2000	34	36	35	39	45	45	46	45	45	37	34	31
2100	29	36	37	35	47	45	47	45	45	37	33	34
2200	31	34	33	41	43	44	48	47	47	39	35	36
2300	34	31	33	36	43	47	50	45	49	38	36	31



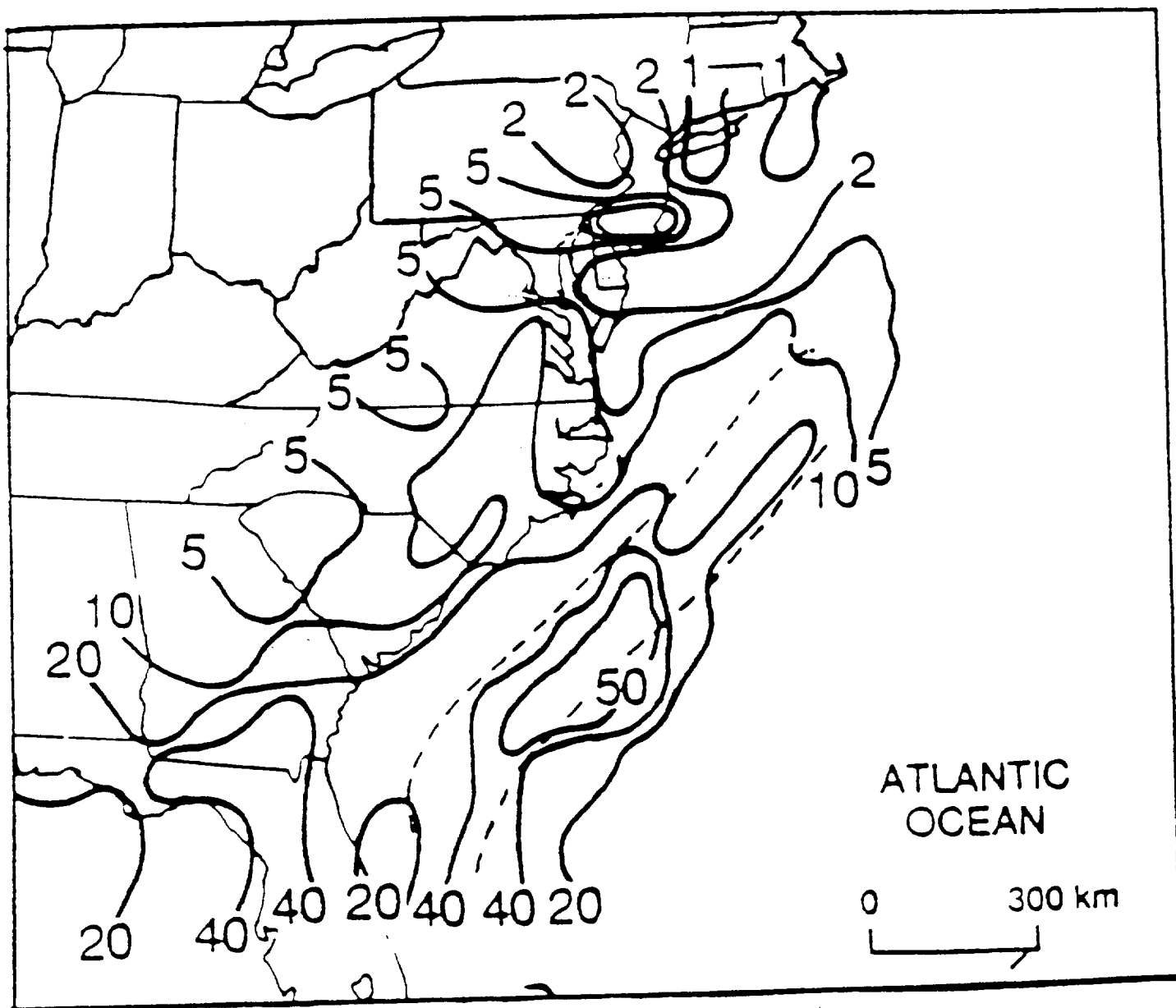
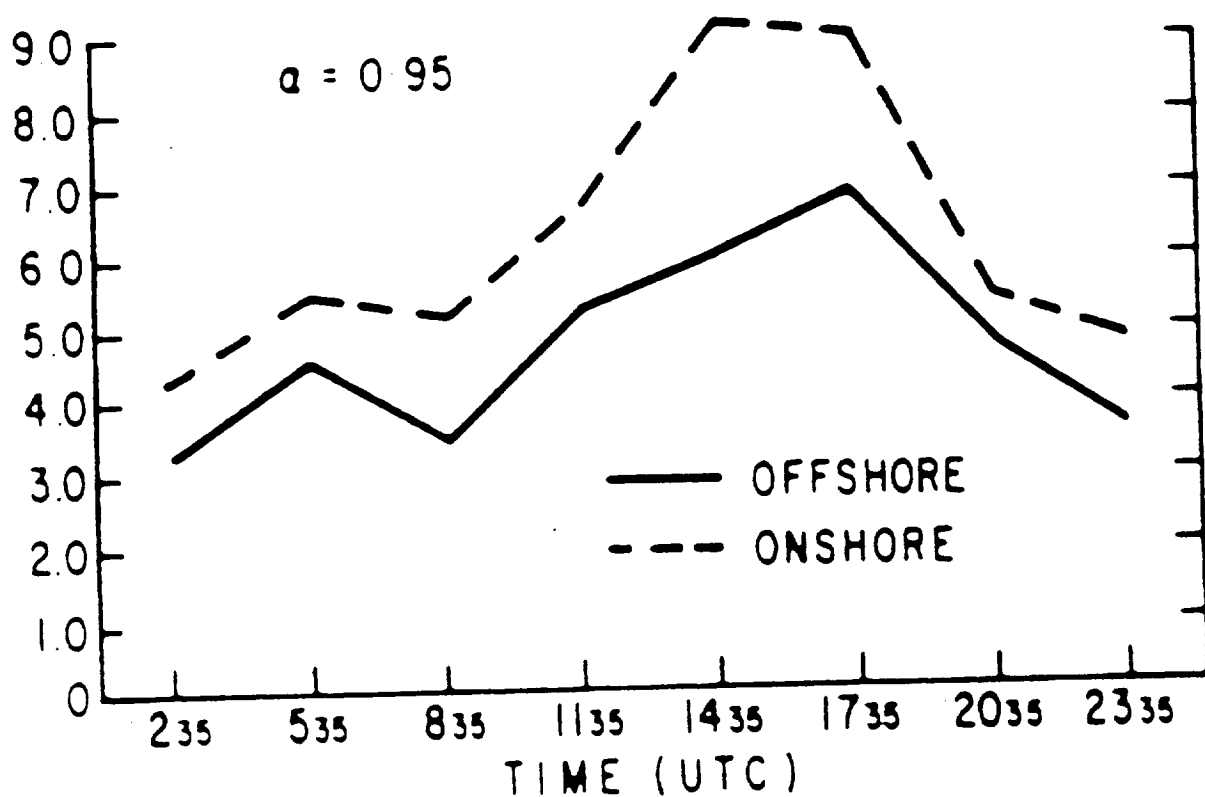


Fig. 1

ECHO DENSITY (NUMBER OF EVENTS PER HALF DEGREE LATITUDE - LONGITUDE BOX)

# DAYTONA BEACH: VIP 1



# DAYTONA BEACH: VIP 3

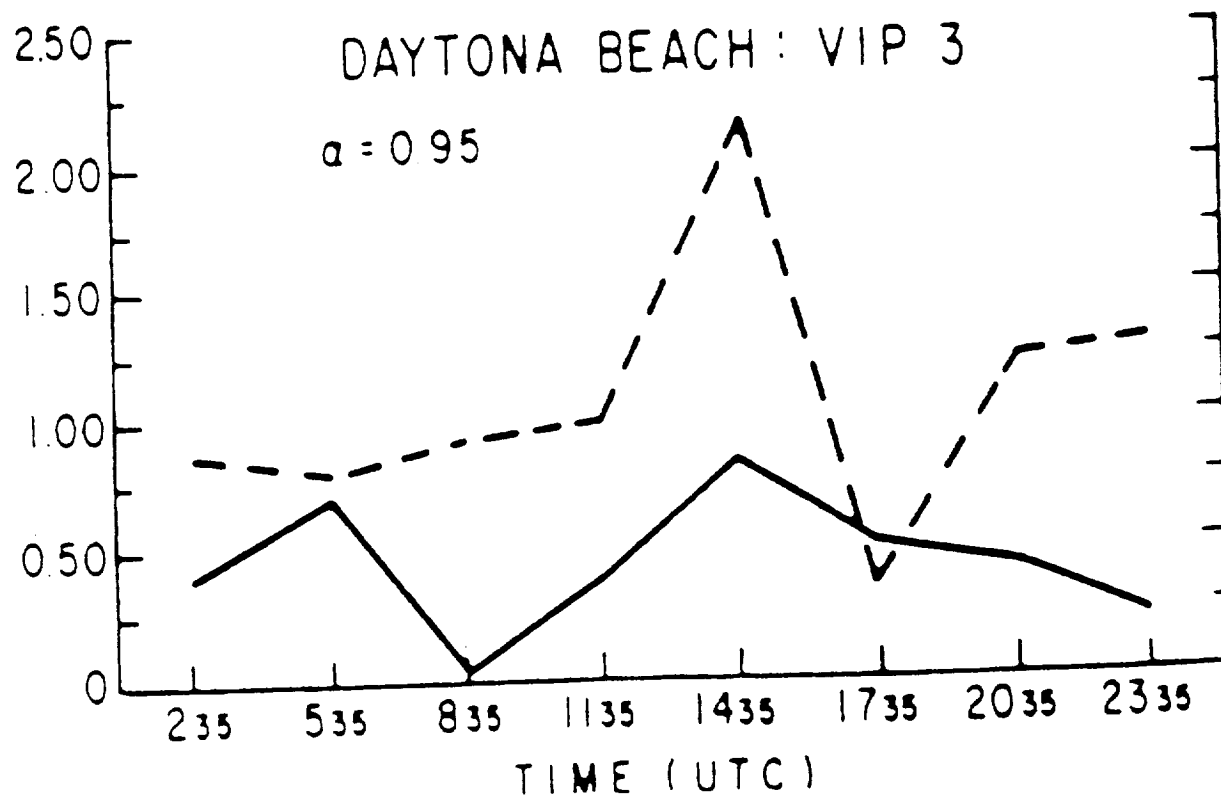
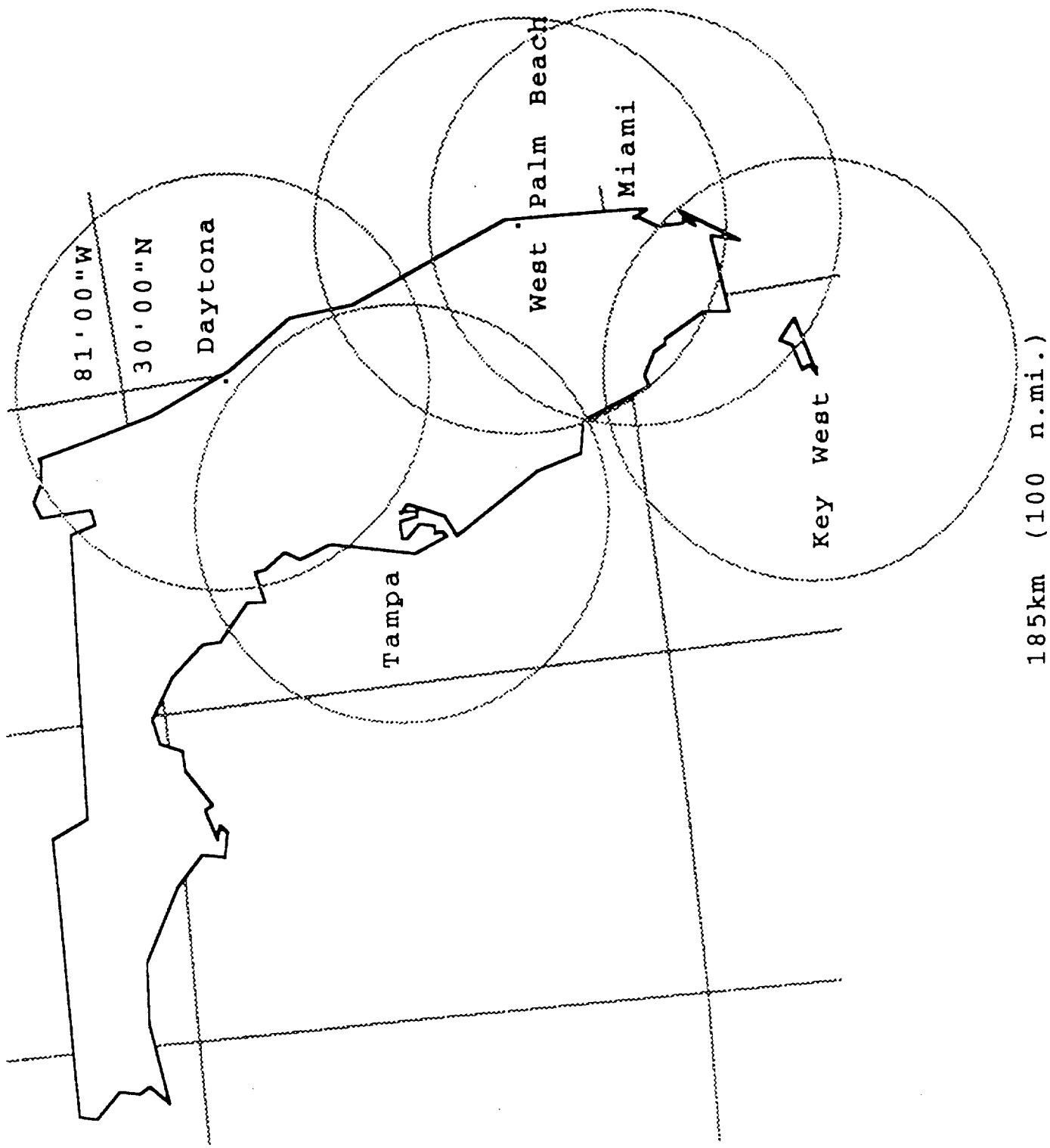


Fig. 2



185km (100 n.mi.)

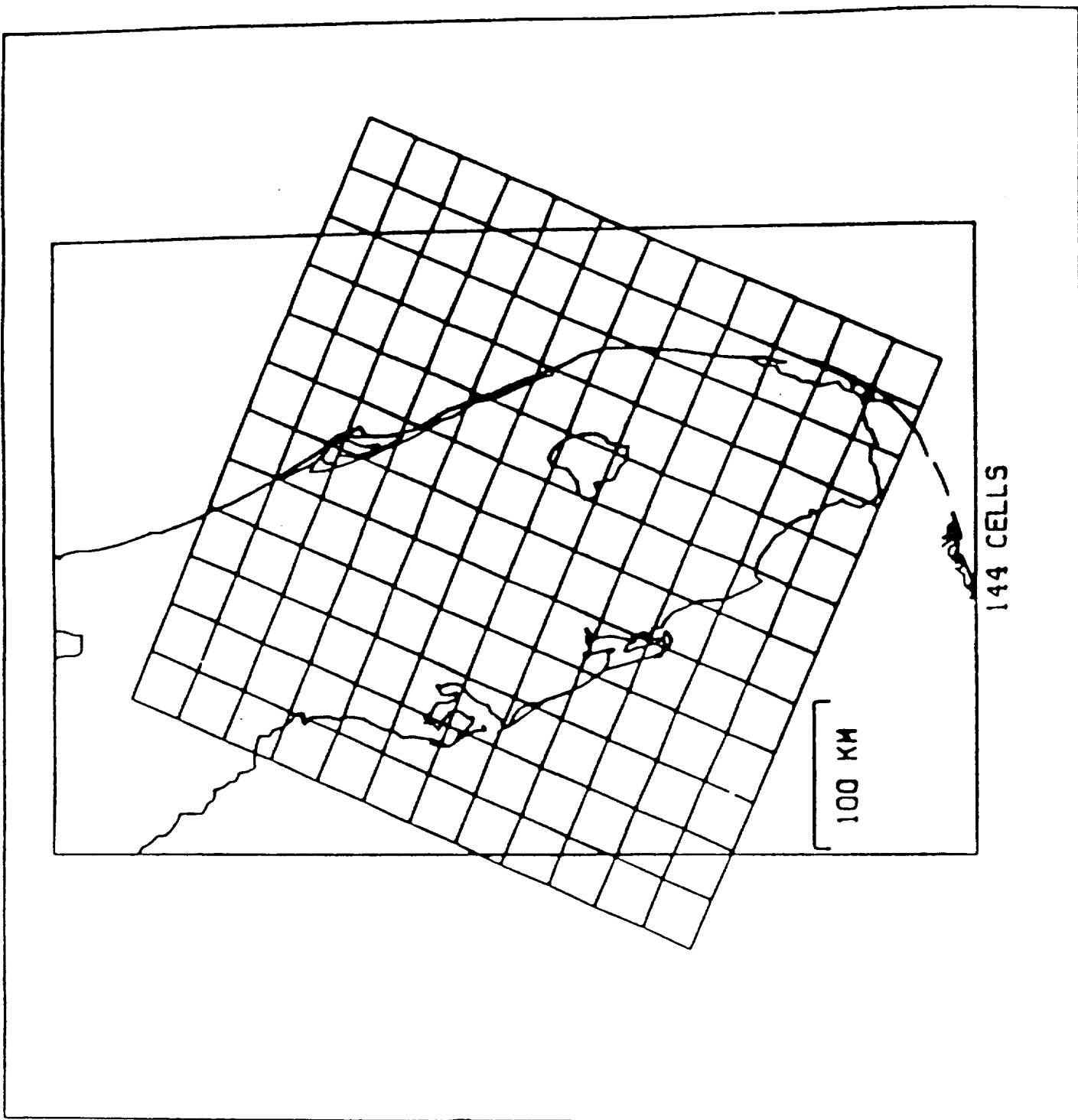
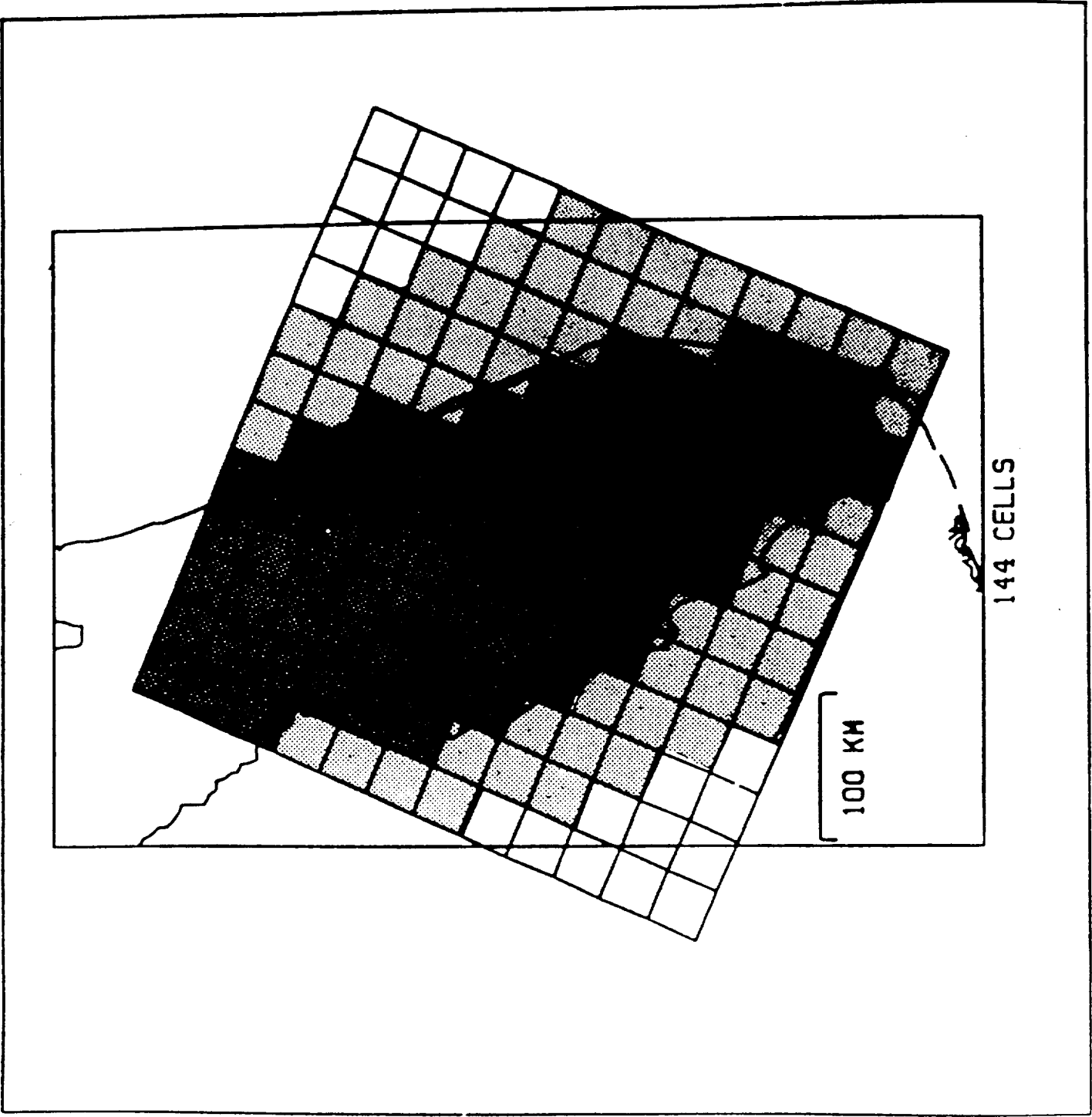


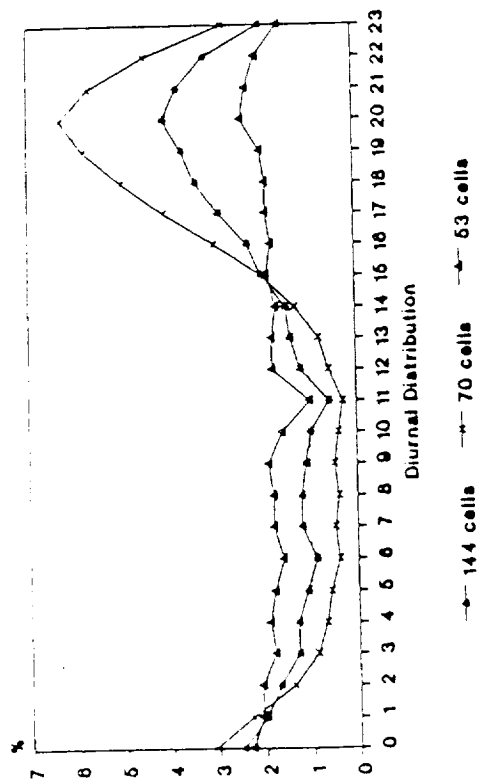
Fig. 1



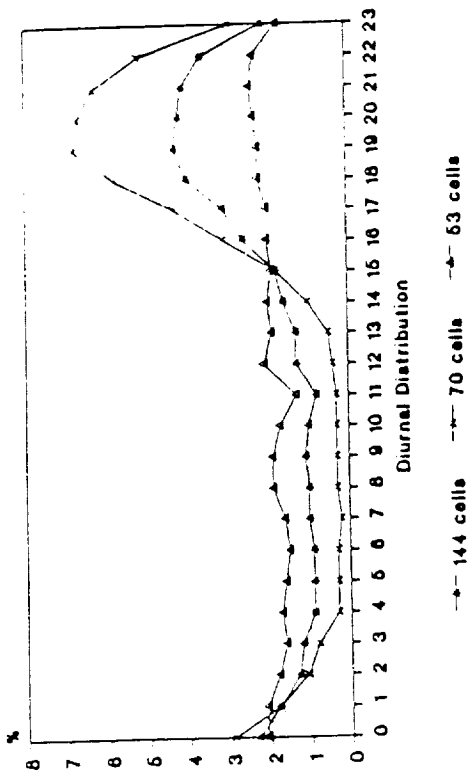
5-16-95

# LEVELS 3-5 vs T.D.E.H. for SUMMER MONTHS

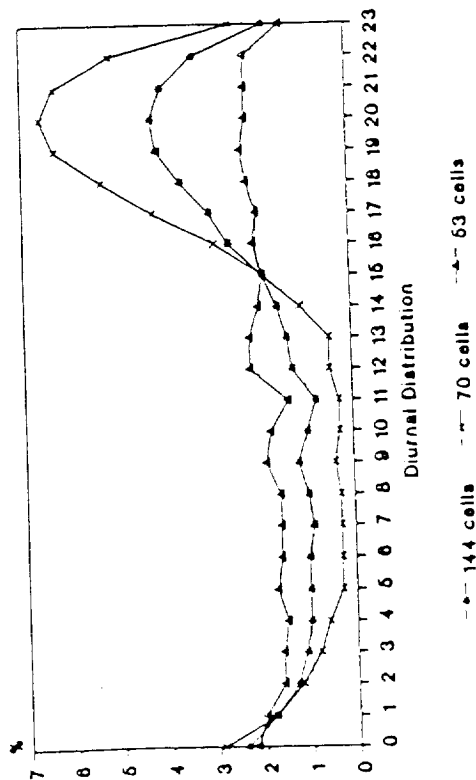
June



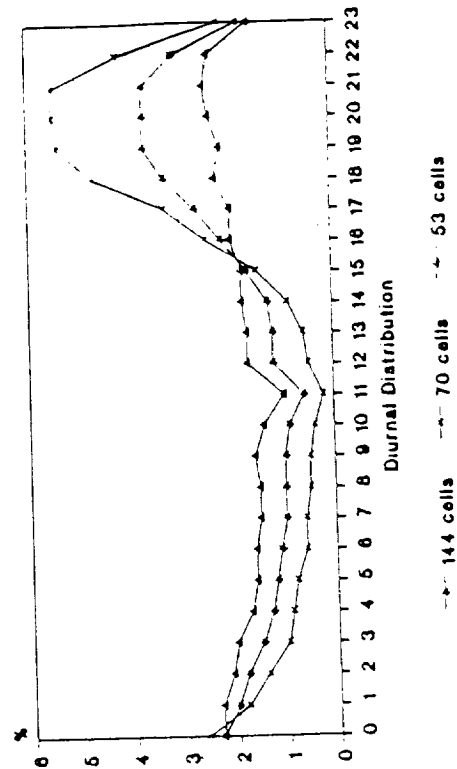
July



August



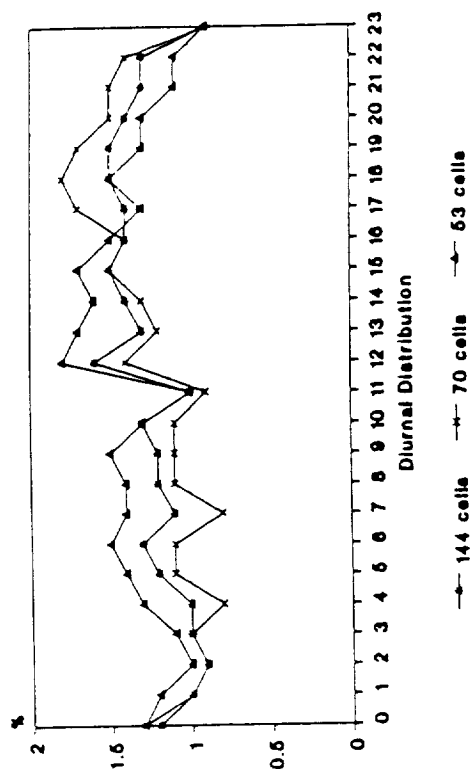
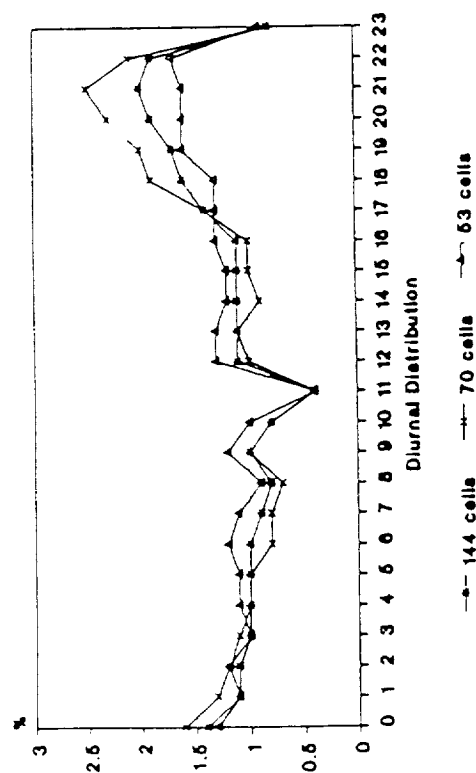
September



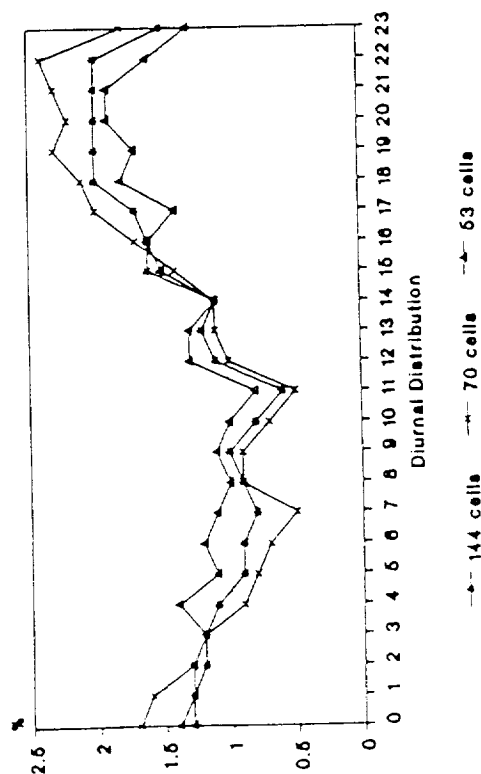
TIME UTC MCH Data 1970 86

# LEVELS 3-5 vs T.D.E.H. for WINTER MONTHS

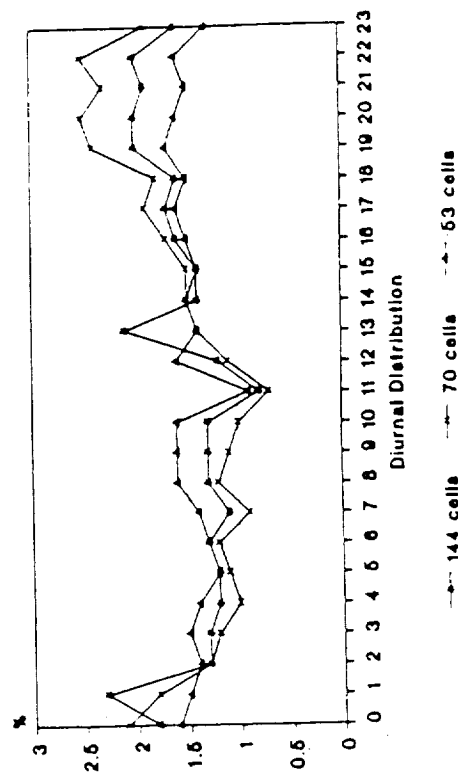
## December



## February

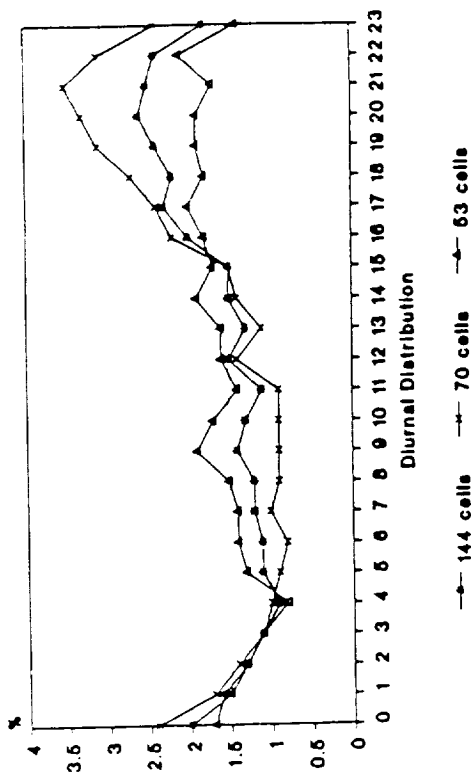
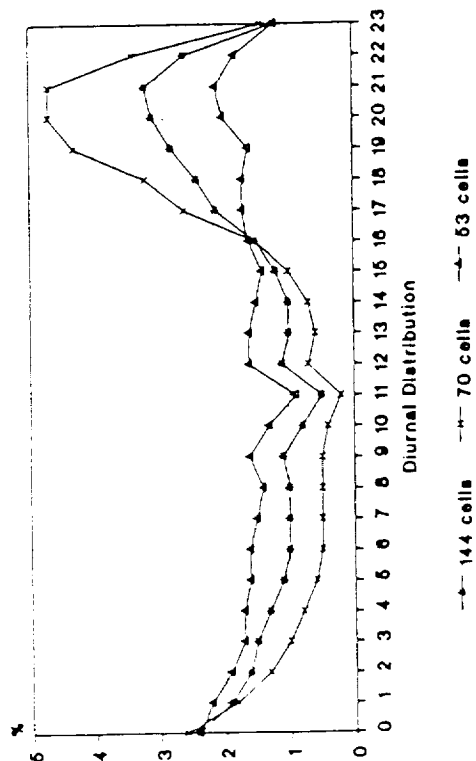


## March

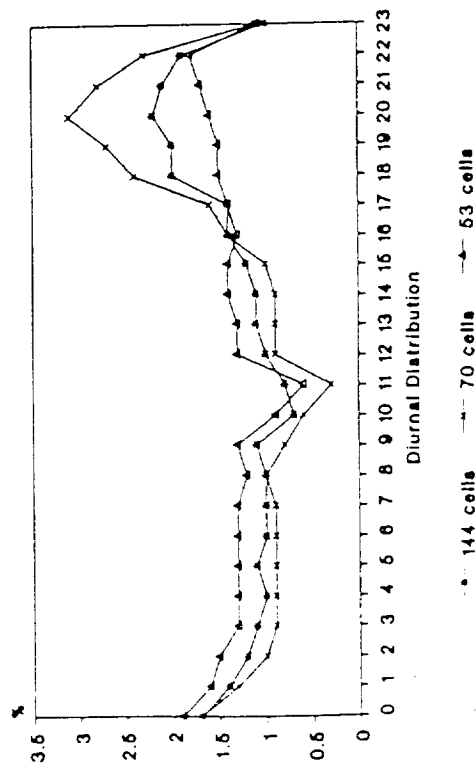


# LEVELS 3-5 vs T.D.E.H. for TRANSITION MONTHS

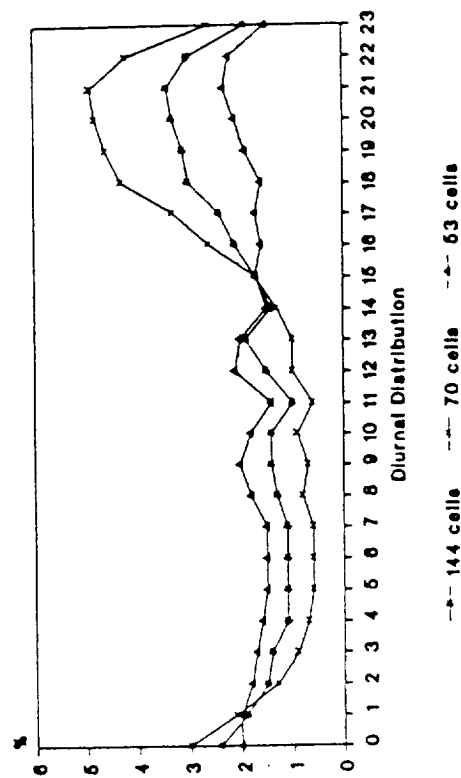
October



November



May





**On the Calibration and Use of  
Radar and an Optical Rain Gage  
To Measure Oceanic Rainfall**

B.J. Turner and G.L. Austin

McGill Radar Weather Observatory  
Macdonald Campus, McGill University  
Ste. Anne de Bellevue, Quebec, Canada.

J. Wilkerson

Satellite Research Laboratory, National Environmental Satellite,  
Data, and Information Service, NOAA, Suitland, Maryland

M. Garstang

University of Virginia  
Charlottesville, VA.

**ABSTRACT:**

In support of the development of a ground truthing site for the TRMM satellite project the radar at Patrick AFB was operated in a manner compatible with the collection of areal rainfall estimates. The radar coverage is over Florida and the adjacent part of the Atlantic Ocean. This data was calibrated using a network of gages located near the Kennedy Space Center, Cape Canaveral. An optical rain gage was deployed on a buoy a similar distance from the radar but out at sea. It was found that the optical gage and the radar were in good agreement, lending support to the use of the optical rain gage for long term ocean buoy deployments.

A review of alternative radar calibration procedures indicates that best results will be obtained for direct radar to gage network intercomparisons rather than matching of cumulative distribution functions.

## 1. Introduction

A number of areas of study in meteorology require a more thorough understanding of the hydrological cycle, in which precipitation plays a key role. Yet reliable estimates of areal averaged precipitation are available only for a small fraction of the earth's surface, and almost not at all over the oceans. Even for satellite-based systems, it is necessary to extend the range of ground truth measurements.

Measurements of rainfall over the oceans are sparse, and a World Meteorological Organization report (WMO, 1970) concluded that, at that time, all methods were subject to significant difficulties. It was stated in that document that "every effort should be made in order to improve our present knowledge of precipitation at sea".

This study considers summer Florida precipitation measured by several methods. The Kennedy Space Center, Cape Canaveral (KSC) rain gage network provided high temporal resolution data. Observations by the Patrick Air Force Base (PAFB) weather radar were calibrated, as discussed in Section 2, in a direct comparison with the gage data. An optical rain gage, deployed on a buoy in the ocean off the Florida coast, provided a third set of measurements which are considered in Section 3.

Section 4 considers the compromising effects that the intermittency of rainfall will have upon some statistical methods of radar calibration. Comparisons are made of the statistics of rainfall measurements at different spatial and temporal resolutions.

## 2. Radar Calibration

Radar reflectivities (  $Z$  ) can be converted to estimated rainfall rates (  $R$  ). The form of the Z-R relation is usually taken to be a power law (Marshall and Palmer, 1948):

$$Z = a R^b \quad (1)$$

The best choice of parameters 'a' and 'b' for a given situation is dependent on microphysical parameters such as the drop size distribution and updraft speed.

The best choice of the parameters "a" and "b" are also dependent on the data processing and averaging methods. This is particularly true for strongly convective rainfall, where spatial resolution of observations becomes a very important factor (Tees and Austin, 1989).

The calibration of the radar Z-R relation may be accomplished by a variety of techniques. The hardware reflectivity calibration can be carried out using any of the methods found in Smith (1968). After this is done the Z-R relations can be optimized by minimizing error between radar derived accumulations and colocated rain gage measurements for the same time period. Data from 17 rain gages of the KSC network were used for this purpose.

An absolute minimum detection level was not available for the PAFB radar, due to difficulty in locating an adequate bore site and local restrictions on balloon flying. Setting the threshold at 8 dBZ was

found to lead to reasonable results in comparison with gages. The values of the two parameters in equation (2) for this study, then, are for this choice of threshold level. Since the work here was conducted an appropriate site has been found from which routine electrical calibrations are made.

The PAFB radar uses a scanning strategy of a 5 minute sequence of conical scans at 24 different elevation angles. For each range distance from the radar, there is some elevation angle for which the beam center is located closest to any particular height of interest. This allows images to be assembled from various elevation scans to indicate the precipitation patterns at a particular height above the ground. Such a product is termed a Constant Altitude Plan Position Indicator ( CAPPI ) (Langleben and Gaherty, 1957).

For the purpose of this calibration, CAPPI images at a height of 2 km were used in estimating surface rainfall. A height for calibration was required which would be above most of the ground clutter in the radar data which might seriously hamper the calibration. Yet the height chosen should still be below the levels at which rain might be being generated. For summer Florida weather, at the 2 km height this seems a reasonable assumption.

The polar data recorded by the radar in dBZ levels was first converted to Z. It was then averaged in Z over 2 km by 2 km resolution pixels, then converted to R.

Between 2340 GMT, Sept. 22, 1989 and 0200 GMT, Sept. 23, 1989 a storm passed over the KSC rain gage network. Good data was available for that period from both the gages and the radar.

The parameter "b" was set to 1.60 in the Marshall-Palmer Z-R relation from observations of stratiform rainfall. This parameter has been found in the past to be more appropriately set to 1.40 for summer Florida rainfall (Gerrish and Hiser, 1965). For this calibration study, values of the parameter "b" were chosen in the range 1.00 to 1.60. For each "b", an "a" value was found for which the mean radar derived accumulation over the gage sites would match the actual mean gage accumulation.

The 17 gages used had a mean accumulation of 12.1 mm during the time period considered. The relation chosen for use in the rest of this study was:

$$Z = 360 R^{1.35} \quad (2)$$

The mean absolute error was less than 20% of the mean gage accumulation for all values of "b" considered, and as seen in Fig. 1, was nearly constant for relations with the parameter 'b' taking values from 1.1 to 1.6. This suggests that the precise value of the parameter 'b' is not crucial in obtaining accurate rainfall estimates from radar data. A multiparameter radar capable of determining 'b' by combining the extra quantities measured would not have greatly increased the accuracy of the estimates.

### 3. Optical Rain Sensor Comparisons

The optical rain gage used (a model 705 manufactured by Scientific Technology Incorporated) was developed from an earlier

design (Wang et al., 1983). The instrument operates by measuring variations in the intensity of a light beam transmitted over a 0.5 m path. The partially coherent beam is formed by the transmitter optics using an infrared emitting diode as a light source. The receiver optics, employing a 1 mm horizontal line aperture, is sensitive only to the vertical motion of objects entering the beam. Rain drops with a vertical component of velocity passing through the beam cause optical scintillation of the received light. Variations of intensity of the received power are detected, bandpass filtered and converted to produce a voltage proportional to the log of the average fluctuating power. This output voltage is linearly related to the log of the rainfall rate. The logarithmic output covers over four decades of dynamic range from 0.1 to 3000 mm/hr.

From July 17 to September 28, 1989, this instrument was deployed on a buoy in the Atlantic Ocean, offshore from PAFB. The platform, a 6 m boat buoy, was moored in 40 m of water approximately 50 km from the coast. The rain gage was mounted on the superstructure of the buoy at a height of 8 m in order to be clear of obstructions. A digital acquisition system located within the buoy recorded an average rainfall rate every 5 minutes from 1 second samples. A summary of the rain events measured by the rain gage at the buoy site is presented in Fig. 2.

The optical gage results were for the most part reliable. One storm case, during a period of strong winds (as measured by an anemometer on the buoy), showed abrupt high rainfall rates. There was no evidence of any rainfall in the radar data. These were thought to be unrealistic readings, probably due to ocean spray

reaching the sensor. This storm case was omitted from the radar - optical gage comparison which follows.

Extra uncertainties arise in radar estimations of rainfall rates at a point, more so than those for estimating accumulation. The 4 to 8 minutes for raindrops to fall through 2 km (from the CAPPI height used in these comparisons) are partially compensated for, since the time given is for the end of each radar volume scan. The actual radar returns were recorded from a low elevation rotation in the sequence perhaps 3 minutes before the end of scan time.

Also, during the fall time the raindrops will be advected a distance and direction dependent on the wind velocity. If storm motions are taken as an indication, wind speeds are of the order of 20 to 40 km/hr. This could result in a 2 km to 3 km horizontal drift during the estimated fall time from the CAPPI height to the sea surface. In the presence of strong horizontal rainfall gradients, which are frequent for the convective storms studied, this can result in substantial difference in sensor estimates averaged over short periods. In Fig. 3 (a)-(f) such problems are apparent.

Comparisons were made between the optical gage results and the calibrated PAFB radar estimates of the rainfall rates in the 16 km<sup>2</sup> area surrounding that point. This was done for several periods of rainfall over the buoy site for which radar data were available. The times of rainfall correspond well between the radar and optical gage data. The bias and mean absolute errors of rainfall accumulation comparisons are shown in Table 1. Similar data for the calibration case with the KSC rain gage network are also shown for comparison. Given the uncertainties in the comparisons of the measurement



systems, due to the variability of the rainfall field, the results are very encouraging. This is evidence, independent of the gage calibration procedure, that the radar data provides a reasonable depiction of the precipitation field over the ocean, and that the optical gage is a viable instrument for buoy deployments.

#### **4. Statistical Comparison Of Rainfall Measurements**

There have been numerous studies of the distributions of rainfall rates measured by radar and by rain gages. More recently the strong dependence of such distributions on the spatial or temporal resolution at which measurements are made has been noted (Lin, 1976; Seed et al., 1990). For example, in strong convective rainfall, the most intense regions of rainfall are small and intermittent, scattered within regions of less intense rainfall. The larger the spatial resolution, or the longer the temporal resolution of measurements, the more the high rainfall rates will be averaged in with nearby lower rates.

Data for August 1989 for the KSC gage network were used to illustrate this resolution dependence of rainfall measurement statistics. The gage data were recorded with one minute time resolution, and could be averaged in such a way to simulate measurements at degraded temporal resolution. Fig. 4 shows how the averaging time for the gage measurements strongly affects the rainfall rate associated with a given value of the cumulative distribution function of rainfall rates.

In any comparison of rain gage and radar statistics, the appropriate matching of an averaging time for the gages and a spatial resolution for the instantaneous radar reflectivities is crucial. Calheiros and Zawadzki (1987) described a radar calibration method based on the cumulative distribution functions (c.d.f.'s) of radar reflectivity values and rain gage measurements (hereafter referred to as the CZ method). If, for example, 60% of radar reflectivities above the threshold were less than some value  $Z$ , and 60% of non-zero rain gage measurements were less than a value  $R$ , then the radar reflectivity  $Z$  would be chosen to correspond to the rainfall rate  $R$ . A relation based on Zawadzki (1975) :

$$1.3 (A)^{1/2} = v t \quad (3)$$

was used in the CZ paper. Here  $A$  is the areal resolution of the radar data,  $t$  is the averaging time of the gage measurements, and  $v$  is the speed of the storm's motion. The CZ method is appealing for its potential to eliminate the need for a series of gage and radar measurements to be co-located in space and time.

However, we believe the nature of the statistics of convective rainfall render the CZ method largely ineffective. First, even accepting equation (3) as a reliable relation, the value of  $v$  can be expected to vary between storms, and even from point to point within a storm. For rapidly developing storms there would be some uncertainty in its actual value. Suppose that radar data which would have been best matched with one temporal scale of gage data was instead matched with another. Fig. 5 and Fig. 6 indicate that, for the

August 1989 KSC gage data, a 20% mismatch of time averaging scales would result in about a 10% bias in the calibration. This would be a serious systematic error in rainfall estimation.

As well, the generality of equation (3) should be called into question, particularly the constant on the left hand side of the equation. This constant should be expected to depend upon the variability of the precipitation field. For a stratiform rainfall pattern, rainfall statistics from a gage (sampling a narrow strip of length  $L$  of the storm as it passes overhead) will be a reasonable estimate of statistics for square areas of area  $L^2$ . In such situations the constant would be close to 1.0. For highly convective cases, the areal measurements over  $L^2$  will average out high rates with nearby lower rates. The gage measurements (of a strip of length  $L$ ) will not have as much 'equivelant spatial averaging'. For such cases, the value of the constant in equation (3) could be much greater than 1.3 .

For the storm of J-Day 232 (Aug. 20, 1989), the accumulation estimates of the optical rain sensor discussed in Section 3 agreed reasonably well with those of the radar as calibrated in Section 2. As an indication of whether equation (3) was at all reasonable for this strongly convective rainfall, the c.d.f. of the 2 km x 2 km radar rainfall rate estimates were compared with the c.d.f.'s of gage measurements, at various temporal resolutions, for the month of August 1989. The radar c.d.f. was best matched to a gage c.d.f. with 10 or 11 min. averaging. By equation (3), this would lead us to expect a storm translation speed of about 15 km/hr. However, as best could be determined for the rapidly changing storm, the storm's speed for the time period varied from 30 km/hr to 60 km/hr. A CZ radar

calibration using equation (3) would have, in this case, resulted in a 200% to 400% overestimation of a reasonable gage averaging time for statistical comparisons.

For gage averaging times of 1 to 12 min., the following function was capable of relating rainfall rates of a specified c.d.f. level:

$$R(T \text{ min.}) = A(T) R(6 \text{ min.}) \quad (4)$$

The value of parameter  $A$  in equation (4), as a function of  $T$ , is shown in Fig. 7.

In a direct comparison of radar and gage accumulations over a period of over an hour, the question of temporal resolution of gage data will not be a problem. It is in the comparison of the rainfall rate statistics averaged over times much less than the period of the storm that the problem arises

## 5. Conclusion

In this study, precipitation measurements over the ocean by radar and by a buoy mounted optical rain gage were in reasonable agreement. As expected, this indicates that radar can be used to measure rainfall over oceanic regions near land. More importantly, this was good evidence of the effective operation of the buoy mounted optical rain gage.

A second thrust of this work concerns radar calibration. A single case direct comparison of radar accumulation estimates with

traditional rain gage amounts provided a good estimation of the Z-R relation parameters. Examination of the intermittent character of Florida convective rainfall indicated that calibration methods relying on indirect statistical comparisons of radar and gage observations would be inadequate.

Radar calibration procedures based on the intercomparison of rain gage and radar cumulative distribution functions should therefore be treated with caution. Large errors can be introduced by differing spatial and temporal sampling of the rainfall field. There appears to be no useful shortcut to the work required for a direct comparison of rainfall accumulation at colocated points by radar and gages.

## References

- Calheiros, R.V. and I. Zawadzki, 1987: Reflectivity - Rainfall Rate Relationships for Radar Hydrology in Brazil, *J. Clim. Appl. Met.*, 26, 118-132.
- Gerrish, H.P. and H.W. Hiser: Meso-scale studies of instability patterns and winds in the tropics, *Rept. 7*. U.S. Army Electronics Labs., Fort Monmouth, N.J., U.S.A., 63 pp.
- Langleben, M.P. and W.D. Gaherty, 1957: An Optical System for Automatic Synthesis of Constant-Altitude Radar Maps. In (Ed.), *Stormy Weather Group Sci. Rep. MWT-3*. McGill University, Montreal, Canada.
- Lin, S.H., 1976: Dependence of rain-rate distribution on rain-gage integration time, *The Bell System Technical Journal*, 55 (1), 135-141.
- Marshall, J. S. and W.M. Palmer, 1948: The Distribution of Raindrops With Size, *J. of Met.*, 5, 165-166.
- Seed, A.W., V.-T.-V. Nguyen, and G.L. Austin, 1990: On the Sensitivity of the Rainfall Probability Distributions to Averaging Area, *Fifth International Conference on Urban Storm Drainage*, 581-586.
- Smith, P.L. Jr., 1968: Calibration of Weather Radars, *Proceedings of the 13th Radar Meteorology Conference*, 60-65.
- Tees, D. and G.L. Austin, 1989: The Effect of Range on the Radar Measurement of Rainfall, *International Symposium on Hydrological Applications of Weather Radar, Paper H2*. Department of Civil Engineering, University of Salford, U.K.
- Wang, Ting-i, P.N. Kuma, and D.T. Fang, 1983: Laser Rain Gage: Near-Field Effect, *Applied Optics*, 22, 4008-4012.

World Meteorological Organization, 1962: Precipitation Measurements at Sea, *Technical Note No. 47*, 13.

Zawadzki, I, 1975: On Radar-Raingage Comparisons, *J. Appl. Met.*, 14, 1430-1436.

## Table and Figure Captions

Table 1 - Statistics of radar to gage accumulation comparisons.

- Fig. 1 - Mean absolute errors between radar and gages for accumulations from 2340-0200 GMT, Sept 22, 1989. Mean gage accumulation was 12.1 mm for that time period.
- Fig. 2 - Summary of the rain events recorded by the optical rain gage for the period July 17 to Sept. 28, 1989.
- Fig. 3 - Time series of radar and optical gage measured rainfall rate comparisons: (a) J-Day 223, (b) J-Day 266, (c)-(f) J-Day 232.
- Fig. 4 - Rainfall rate at several c.d.f. levels as a function of gage averaging time.
- Fig. 5 - Effects of rainfall c.d.f. matching for 4 and 6 min. temporal averaging instead of 5 min. averaging.
- Fig. 6 - Effects of rainfall c.d.f. matching for 8 and 12 min. temporal averaging instead of 10 min. averaging.
- Fig. 7 - The value of parameter A in equation (4) as a function of gage averaging time.



## Radar - Raingage Calibration

Calibration Time Period: 2340 - 0200 GMT  
Sept. 22, 1989.

Optimal Z-R Relation:  $Z = 360 R^{1.35}$

Accumulation Time: 2 hr., 20 min.

Number of Gages: 17

Mean Gage Amount: 12.1 mm

Mean Absolute Error: 2.23 mm  
= 18.4% of mean gage amount

## Radar vs. Optical Gage

Number of Storm Comparisons: 4

Mean Storm Accumulation Time: 2 hr.

Mean Optical Gage Accumulation: 5.72 mm

( Radar / Optical Gage ) = 20.71 mm / 22.87 mm  
= 0.91

Mean Absolute Storm Difference = 1.57 mm  
= 27.4% of mean optical gage accumulation

Table 1

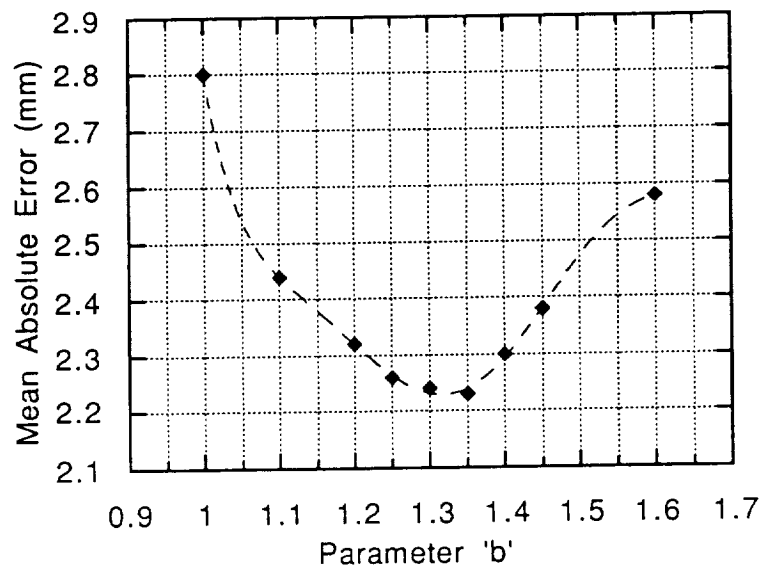
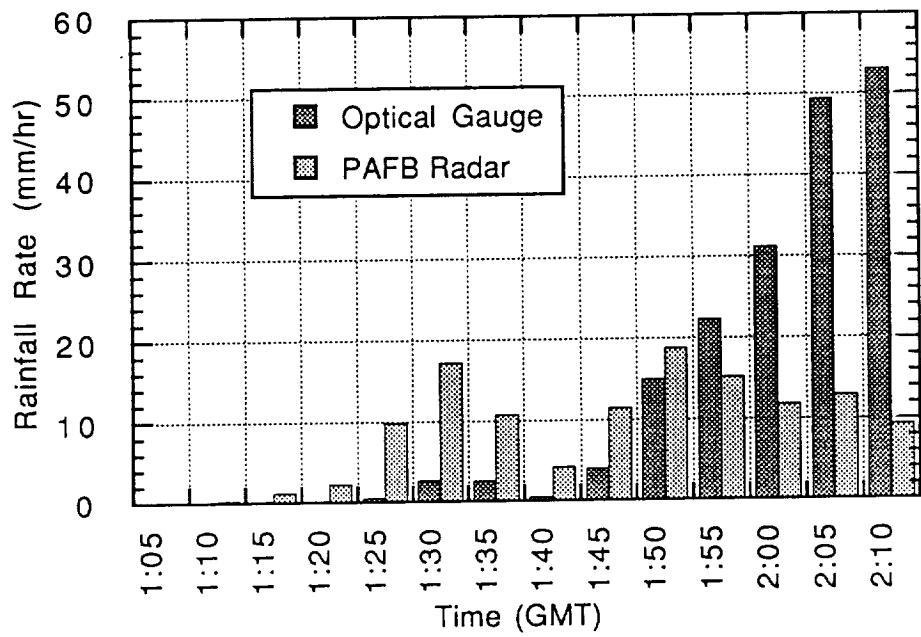
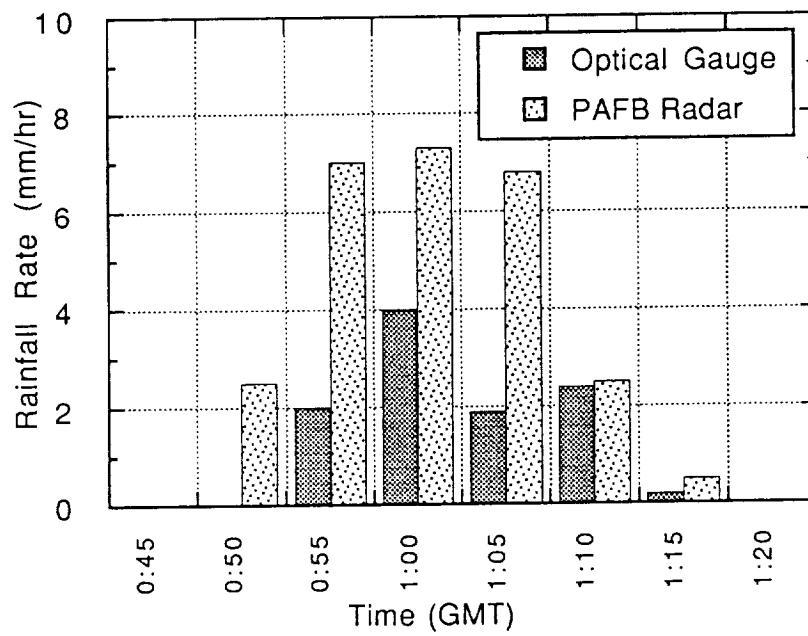


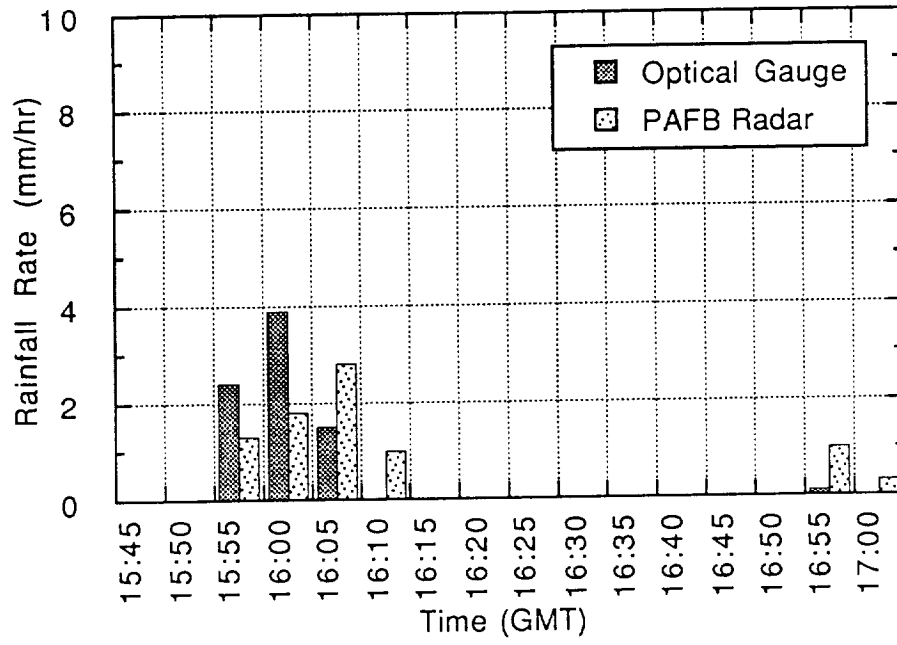
Fig. 1



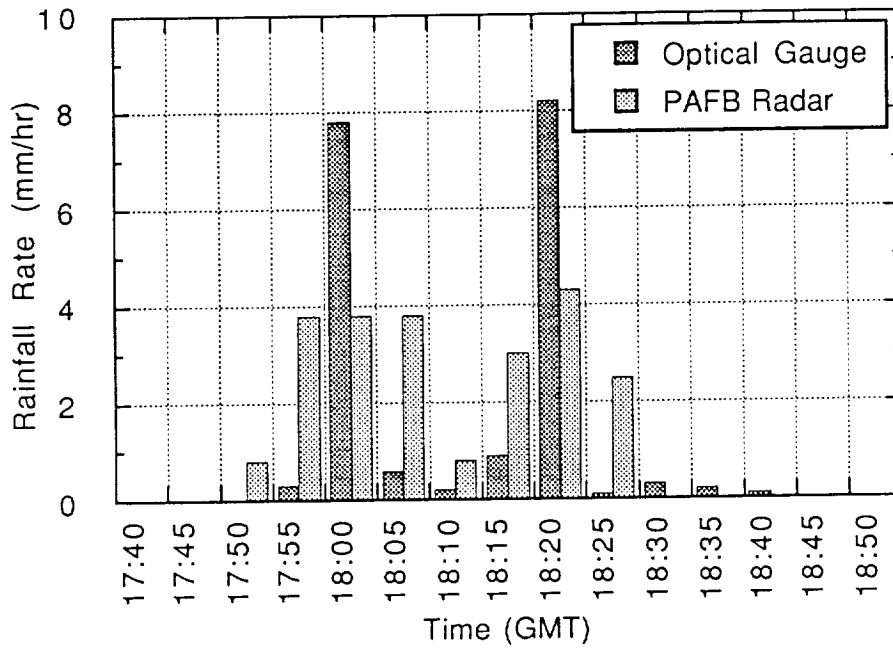
(a)



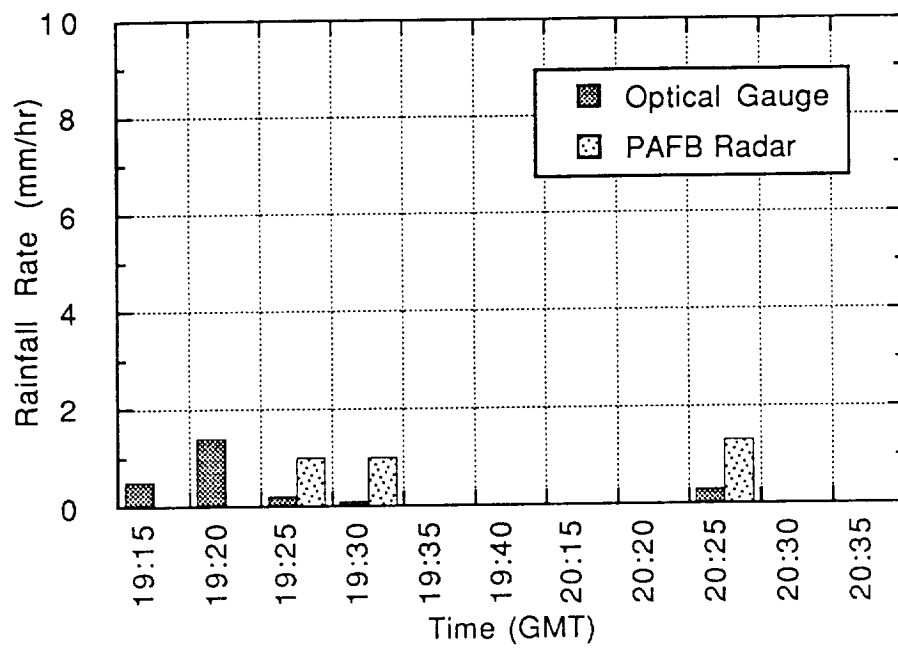
(b)



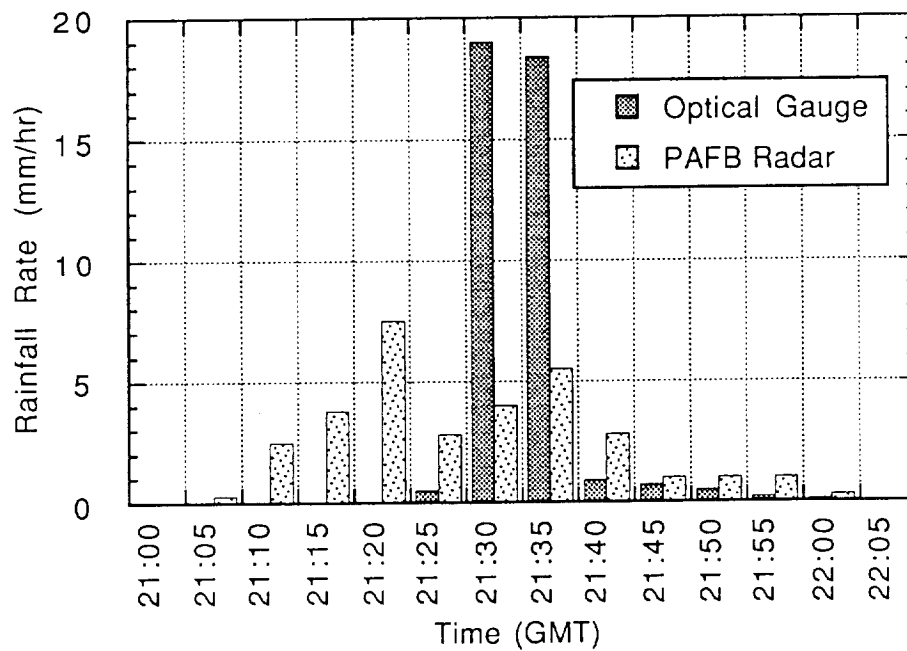
(c)



(d)



(e)



(f)

Fig. 3

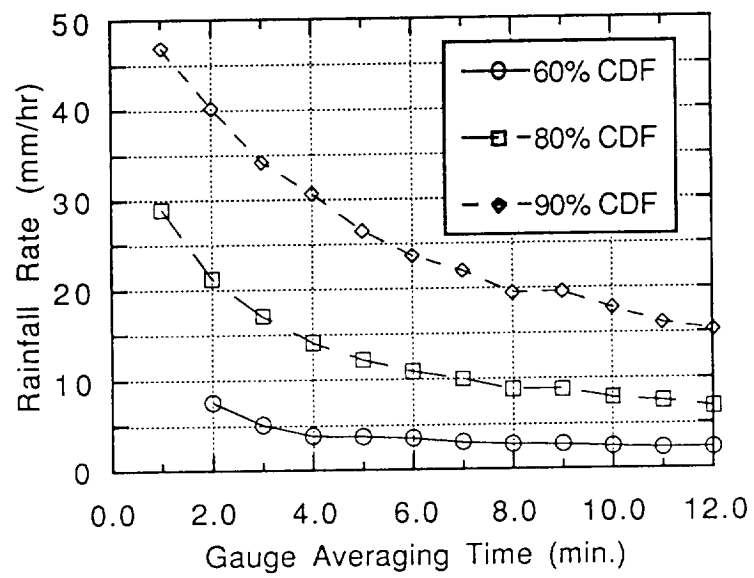


Fig. 4

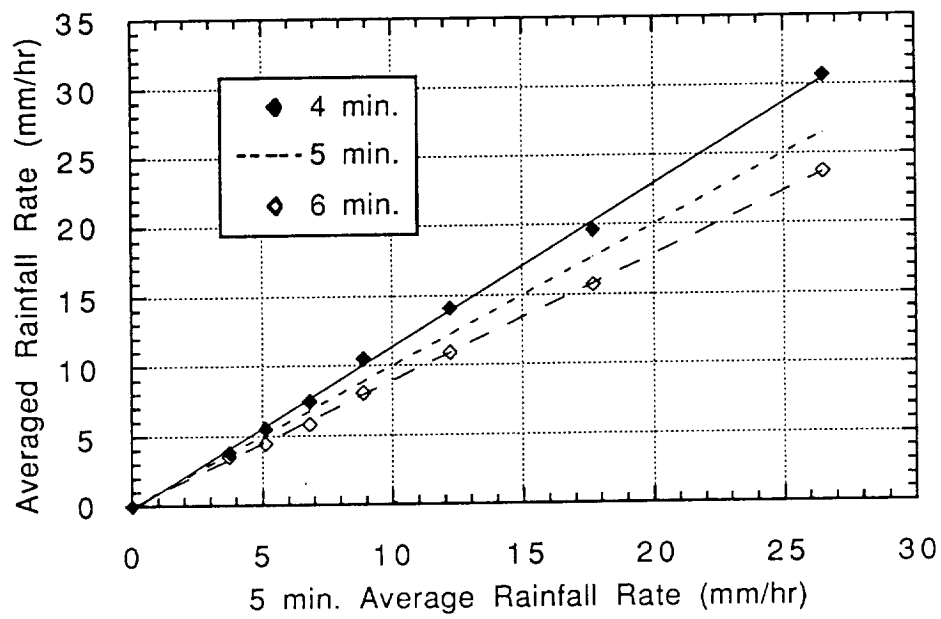


Fig. 5

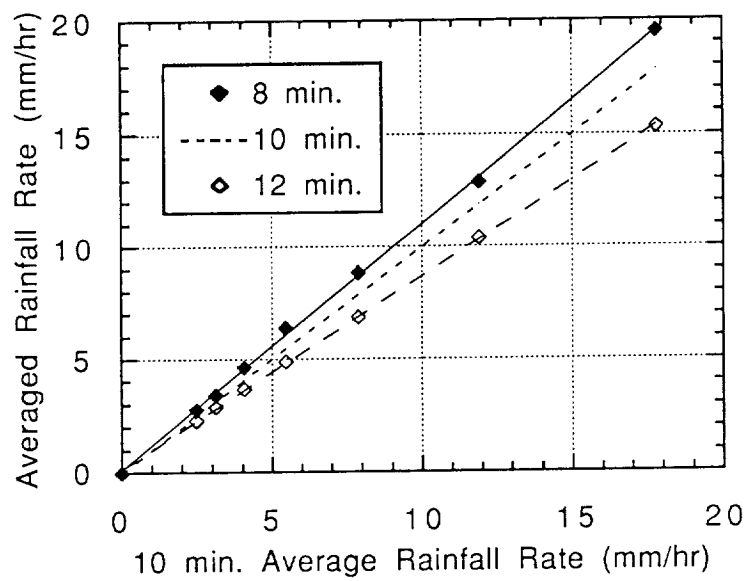


Fig. 6

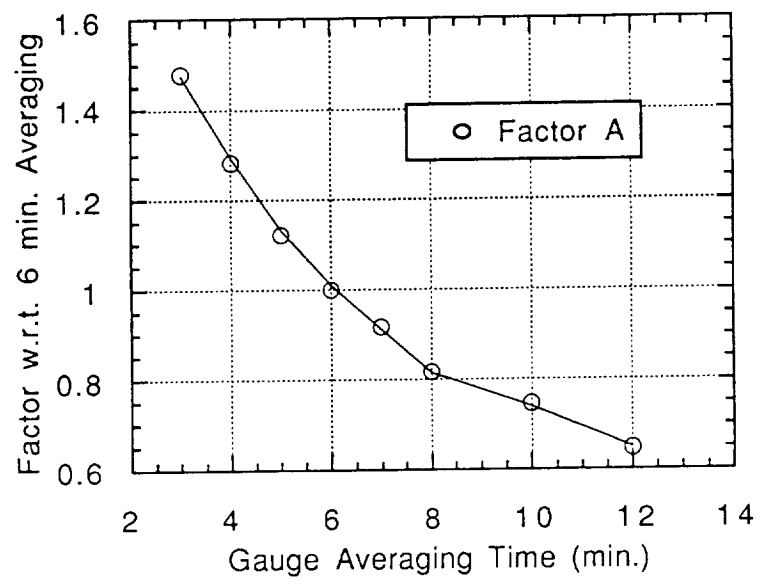


Fig. 7



**Spatial Variability Of Summer Florida Precipitation  
and Its Impact on Microwave Radiometer  
Rainfall Measurement Systems**

B.J. Turner and G.L. Austin  
McGill Radar Weather Observatory  
McGill University  
Montreal, Canada.

## ABSTRACT:

Three dimensional radar data for three summer Florida storms is used as input to a microwave radiative transfer model. The model simulates microwave brightness observations by a 19 GHz, nadir pointing, satellite borne microwave radiometer.

The statistical distribution of rainfall rates for the storms studied, and therefore the optimal conversion between microwave brightness temperatures and rainfall rates, was found to be highly sensitive to the spatial resolution at which observations were made. The optimum relation between the two quantities was less sensitive to the details of the vertical profile of precipitation.

Rainfall retrievals were made for a range of microwave sensor footprint sizes. From these simulations, spatial sampling error estimates were made for microwave radiometers over a range of field of view sizes. The necessity of matching the spatial resolution of ground truth to radiometer footprint size is emphasized. A strategy for the combined use of rain gauges, ground based radar, microwave and VIS/IR satellite sensors is discussed.

## 1. INTRODUCTION

Spatial resolution of present microwave radiometers is often large enough that it is comparable with the scale of substantial horizontal variability of rainfall patterns. This is particularly true of particularly convective rainfall observed in the tropics. The footprint or field of view (FOV) of the sensor can contain sharp gradients of rainfall rate, or a mixture of raining and non-raining areas. This frequently leads to averaging errors since the brightness temperature - rain rate relationship is generally nonlinear.

The horizontal FOV problem has been considered in a number of studies. Short and North (1990) have considered the problem using actual ship based radar and satellite based microwave observations from the GARP Atlantic Tropical Experiment (GATE) data. A further study was conducted using a stochastic rain field model tuned to the parameters of the GATE data (Bell et al., 1990).

In the present study three dimensional radar data is used as input to a microwave radiative transfer model. Radar data are actual measurements of rainfall rather than the output of models based on such measurements. This at least eliminates one set of assumptions. Also, the three dimensional data allows investigation of the largely unknown effect of vertical variability in rainfall on microwave radiative transfer and on microwave radiometer rainfall estimates. In the past, two-dimensional radar rainfall maps such as those published from the GATE experiment (Arkell and Hudlow, 1977) have been more often

used. Given the extensive attention which has already been given to the GATE data set, the opportunity was taken to consider rainfall measurements from another tropical location. The radar data used here is from Patrick Air Force Base near Cape Canaveral in Florida. The digitizing and recording system for this radar system was designed and built by a group from the Radar Weather Observatory of McGill University in Montreal, Canada.

Radar provides measurements of reflectivity from precipitation, and from this quantity rainfall rate estimates can be derived. The resulting remotely sensed image cannot be said to be an exact representation of a precipitation field which actually occurred. Radar measurements are subject to a number of errors as described by Austin (1987). Here it will be assumed the radar data set provides representative statistical properties, down to the spatial resolution of the observations, and hence represents to some extent an image of a rainfall field which could have existed.

Microwave radiometer rainfall retrieval algorithms were developed for a range of sensor spatial resolutions, based on the statistics of the simulated 19 GHz observations. The accuracy with which a 19 GHz microwave radiometer can be used to measure precipitation was examined. Its ability was evaluated for the estimation of average rainfall rate, at a particular time, over a 300 000 km<sup>2</sup> area. Comparing these retrieval rainfall fields with the radar data used for the simulation provided estimates of spatial sampling errors and effects of the variability in the vertical profile of the precipitation.

## 2. METHOD

### 2.1 Radar Data

At wavelengths commonly used in meteorological radars (10 cm, 5 cm, and 3 cm), the backscattering of radar beam energy from raindrops is subject to the Rayleigh approximation:

$$Z \propto \sum D^6 \quad (1)$$

That is, the radar reflectivity factor  $Z$  is proportional to the sum of the sixth powers of the raindrop diameters.

However, converting this quantity to rainfall rate  $R$  is not a simple matter. A number of  $Z$ - $R$  relations have been found over the years for different meteorological conditions. The form of the  $Z$ - $R$  relation is usually taken to be a power law (Marshall and Palmer, 1948):

$$Z = a R^b \quad (2)$$

The best choice of parameters 'a' and 'b' for a given situation is dependent on microphysical parameters such as the drop size distribution, and is also dependent on the data processing and averaging methods. This is particularly true for strongly convective rainfall, where spatial resolution becomes a very important factor (Tees and Austin, 1989).

The calibration of the radar Z-R relation may be accomplished by a variety of techniques. The hardware reflectivity calibration can be carried out using any of the methods found in Smith (1968). After this is done the Z-R relations can be optimized by minimizing error between radar derived accumulations and colocated rain gauge measurements for the same time period. Data from 17 rain gauges of the Kennedy Space Centre ( KSC ) network were used for this purpose.

The PAFB radar uses a scanning strategy of a 5 minute sequence of conical scans at 24 different elevation angles. For each range from the radar, there is some elevation angle for which the beam centre is located closest to any particular height of interest. This allows images to be assembled from various elevation scans to indicate the precipitation patterns at a particular height above the ground. Such a product is termed a Constant Altitude Plan Position Indicator ( CAPPI ) (Langleben and Gaherty, 1957).

For the purpose of this calibration, CAPPI images at a height of 2 km were used in estimating surface rainfall. A height for calibration was required which would be above most of the ground clutter in the radar data which might seriously hamper the calibration. Yet the height chosen should still be below the levels at which rain might be generated. For summer Florida weather, at the 2 km height this seems a reasonable assumption .

The polar data recorded by the radar in dBZ levels was first converted to Z. It was then averaged in Z over 2 km by 2 km resolution pixels, then converted to R.

Between 2340 GMT, Sept. 22, 1989 and 0200 GMT, Sept. 23, 1989 a storm passed over the KSC rain gauge network. Good data was available for that period from both the gauges and the radar.

The parameter "b", which is set to 1.60 in the Marshall-Palmer Z-R relation, has been found in the past to be more appropriately set to 1.40 for summer Florida rainfall (Gerrish and Hiser, 1965). For this calibration study, values of the parameter "b" were chosen in the range 1.0 to 1.6. For each "b", an "a" value was found for which the mean radar derived accumulation over the gauge sites would match the actual mean gauge accumulation. The mean absolute errors are seen to be nearly constant for a range of relations with the parameter 'b' taking values from 1.25 to 1.45. The relation chosen for use in the rest of this study was:

$$Z = 360 R^{1.35} \quad (4)$$

As shown in Fig. 1, this Z-R relation resulted in the minimum mean absolute errors.

Radar data was processed in this manner, for the following three periods of convective Florida rainfall:

1940 - 2240 GMT, July 19, 1989	(J-Day 200)
1340 - 1810 GMT, Aug 20, 1989	(J-Day 232)
1120 - 1915 GMT, Sept 15, 1989	(J-Day 258)

The Julian day (or J-Day) is used as a convenient label of the day being referred to.

## 2.2 Radiative Transfer Model

In the microwave radiative transfer calculations, a number of assumptions and simplifications were made. Secondary effects on calculated upwelling 19 GHz microwave radiances are dealt with by approximations applied identically over the area studied.

The Rayleigh-Jeans approximation, that radiance is proportional to equivalent blackbody temperature, is valid in the microwave region of the electromagnetic spectrum. The microwave radiance (incident power per unit area normal to a particular direction) may be expressed in terms of approximately linearly related 'brightness temperature', namely the equivalent blackbody temperature ( $T_b$ ).

With the assumption of approximately axial symmetry of the radiation field in the neighbourhood of any point, the equation of radiative transfer (Chandrasekar, 1960) becomes :

$$\frac{dT_b}{dh} + \gamma_{\text{ext}} T_b = \gamma_{\text{sca}} \int_0^\pi T_b(\Theta_s) P(\Theta, \Theta_s) \times \sin \Theta_s d\Theta_s + \gamma_{\text{abs}} T(h) \quad (5)$$

where  $\Theta$  specifies a direction from a point being considered,  $T(h)$  is the thermodynamic temperature as a function of height,  $\gamma_{\text{sca}}$  is the scattering coefficient,  $\gamma_{\text{abs}}$  is the absorption coefficient, and  $\gamma_{\text{ext}}$  is the extinction coefficient due to both scattering and absorption. The expression  $P(\Theta, \Theta_s)$  describes a normalized scattering phase function.

Radiative transfer at 19 GHz is most influenced by precipitation. For example, the quantities  $\gamma_{\text{sca}}$ ,  $\gamma_{\text{abs}}$ ,  $\gamma_{\text{ext}}$ , and  $P(\Theta, \phi)$  in equation (5) are primarily determined by the

rainfall rate. By using the radar derived images of rainfall, realistic first-order effects of horizontal and vertical variability of the precipitation will be incorporated into the microwave radiometer simulations. Since three-dimensional radar images were used, assumptions such as uniform rain rate through a pre-specified rain-layer height were unnecessary.

An iterative finite-difference method based on equation (5) was used to determine a vertical profile of brightness temperature. Starting with a realistic value of upwelling microwave radiance at the surface, and ignoring the scattering term, the finite difference method produced an initial estimate of  $T_b$  at each height. On successive iterations an approximation of the scattering term was used, based on the previous estimate for the vertical profile of  $T_b$ . For each vertical profile the calculation was done to a height of 10 km, and iterated until it converged. The value of  $T_b$  at the highest level of 10 km was taken as the brightness temperature which would be observed by a nadir pointing satellite-borne microwave radiometer.

A two-way approximation of the scattering term was used, and adjusted to best reproduce the Wilheit (1977) model behaviour at 19.35 GHz for the model atmosphere used in that paper. As in that simulation, a typical ocean surface emissivity was assumed over the region of study, a uniform layer of cloud was introduced from 3.5 km to 4.0 km height, and ice crystals are assumed to not significantly influence upwelling microwave radiances near 19 GHz.

For each time of radar volume scans, the radar CAPPIs, at 0.5 km height intervals between 1.5 km and 10.0 km, were used as a three-dimensional representation of the precipitation field. The 1.5 km CAPPIs were used to represent the rainfall pattern below this level.

The cloud component which was uniformly introduced is certainly an unrealistic simplifying assumption. More complex cloud models could have been used, but each method would involve assumptions and would likely still underestimate the variability of real cloud fields. At 19 GHz cloud effects are secondary to precipitation effects upon the radiative transfer, so the naive cloud model used was considered acceptable.

For the convective rain cases studied, it was unreasonable to assume that all precipitation above the melting level (0°C isotherm) would be ice crystals. Douglas (1963) shows more reasonable vertical profiles, given strong convective updrafts, of the fraction of water content frozen. In this set of simulations, liquid water fraction was assumed to be at 100% up to 5.5 km, to decrease linearly from 100% to 20% between 5.5 km and 7.5 km, and remain at 20% up to 10.0 km.

The output of the radiative transfer model is a simulation of the image of microwave

brightness temperature as viewed from above the atmosphere. The image is at the fundamental spatial resolution of the radar CAPPI data used as input to the simulation. An image of microwave radiance was produced for each radar volume scan time in the three rainfall cases considered.

### 2.3 Rainfall Retrieval Functions

To produce rainfall estimates from real or simulated microwave radiometer data, a functional relationship must be established between rainfall rate and brightness temperature. With simplifying assumptions concerning the vertical structure of precipitation such curves can be derived. However, even with these theoretical curves there are ambiguities in the estimation of high rainfall rates. This is shown in Fig. 2, taken from Wilheit (1977). For the curves shown, brightness temperature increases with rainfall rate until about 20 mm/hr. Then there is a levelling off and slow decrease of brightness temperature with higher rainfall rates.

For rates greater than about 15 mm/hr, one can expect substantial errors in microwave retrieval estimates. Even if only a small fraction of the raining area falls into this category, such localized heavy rainfall events may be very important hydrologically. This is seen in Fig. 3. For this rain case of J-Day 232, although only 5% of the raining area (at this resolution) shows rates greater than 20 mm/hr, these higher rates contribute almost 30% of the accumulation. These heaviest rainfall measurement errors are probably not significant for most climate studies so long as no overall bias is introduced into long term averages.

For actual retrieval algorithms some sort of unambiguous retrieval method must be devised. The optimal relationship will vary from storm to storm and with the spatial resolution of the data.

The fundamental resolution of the CAPPIs and simulated brightness temperature images was 2 km by 2 km. The spatial resolution of present and proposed satellite-borne microwave radiometers, at 19 GHz or higher frequencies, is substantially larger than this.

Images of the rainfall field at degraded spatial resolutions were produced by averaging in rainfall rate, as indicated by the 1.5 km height radar CAPPI data (from which ground clutter had been removed), to areal resolutions of 16, 36, 64, 100, 144, 196, and 256 km<sup>2</sup>. These degraded images are used to determine the statistical distribution of rainfall rates at each spatial resolution. In Fig. 4 an example pair of image sections at 100 km<sup>2</sup> is shown for visual comparison. In Fig. 4 (b), areas with brightness temperatures greater than the surface emission of 168 degrees Kelvin have been highlighted. The corresponding rainfall rates for those regions on Fig 4 (a) should be noted.

In this study an empirical method was used to determine 'ideal' one-to-one functions for each of the three sets of data over a range of spatial resolutions. This was accomplished using the cumulative distribution functions (c.d.f.'s) for the simulated brightness temperatures ( $T_b$ ) above a certain threshold and for rainfall rates ( $R$ ) of the corresponding 1.5 km CAPPIs. The lower threshold for the  $T_b$  c.d.f. was set so the total area above that threshold would most closely match the total rainfall area. A relation was then established such that the frequency of occurrence of the two parameters were matched:

$$\text{c.d.f.}(T_b(R)) = \text{c.d.f.}(R) \quad (7)$$

Such a method of establishing a function between two related quantities was suggested by Miller (1972) and promoted more recently by Calheiros and Zawadzki (1987) for establishing a proper Z-R relation for radar calibration. In that application the related quantities are radar reflectivity ( $Z$ ) and rainfall rate ( $R$ ) using rain gauge measurements as a reference. For such radar to rain gauge calibrations, though, the sampling characteristics of the two instruments are quite different and this can lead to problems as discussed in Seed and Austin (1990). In this study there is no such difficulty in using such a method to derive a  $T_b(R)$  relationship, since one of the quantities,  $R$ , has been used to simulate the other at the same resolution. The spatial averaging is therefore automatically matched between the two quantities. This is an important aspect of using radar and gauge data to ground truth real microwave radiometer rainfall estimates.

As shown in Fig. 5, each spatial resolution of each day's simulated microwave images required a specific  $T_b$  threshold value to satisfy the area matching condition. An example of the dependence of  $T_b(R)$  on spatial resolution is illustrated in Fig. 6. Finally, Fig. 7 shows  $T_b(R)$ , at 10 km by 10 km spatial resolution, for the three periods of rainfall. The three retrieval curves are similar. In an operational microwave radiometry scheme for estimating rainfall, one retrieval algorithm would likely be used for all three cases. The sensitivity of instantaneous rainfall estimates over large areas to changes between such similar retrieval algorithms is investigated in Section 3.



### 3. RESULTS

#### 3.1 Simulation Descriptions

The microwave radiative transfer model described in Section 2.2 incorporates the effects of radiometer sensor resolution and vertical variability of the precipitation. The merit of simulated retrievals was judged by how accurately an algorithm reproduces the 1.5 km CAPPI images from the associated simulated brightness temperature images. The considerable effects of temporal resolution and variable cloudiness on accuracy have been considered elsewhere (Lovejoy and Austin, 1980 ; Seed and Austin, 1990). These effects are not incorporated into the present simulation.

For comparison, an analysis of retrieval errors from an area-threshold method was performed using the same rainfall data. This is a model of what VIS/IR type satellite systems attempt to accomplish: determine exactly the raining area, and then multiply by an accurate rain-area mean rainfall rate for that period, to obtain an accumulation estimate. It should be noted here that VIS/IR systems actually fall short of this seemingly modest goal (Griffith et al., 1978; Lovejoy and Austin, 1979).

Each method, simulated microwave and VIS/IR, was applied at the following spatial resolutions: 4, 16, 36, 64, 100, 144, 196 and 256 km<sup>2</sup>. The accuracy of each sensor simulation is expressed in terms of the root mean square of the per centage error (r.m.s.%) for instantaneous rainfall estimates averaged over an area of 30 000 km<sup>2</sup>.

For the area-threshold method, the rain area mean rainfall rate is dependent on the resolution of observations in a manner related to the intermittency of the rainfall field. This can be seen in Fig. 8 for each storm case. The mean rainfall rate for the raining areas decreases with increased spatial averaging. Heavy rainfall is distributed in small cells within storms. As areal averaging increases more of these areas are combined with neighbouring regions of lower rainfall rates. Heavy rainfall rates are thus smoothed out at coarser resolutions. This should be a consideration in any rainfall measurement technique based on measurements of rainfall area, otherwise considerable systematic errors could be introduced. It also highlights the problem of using the high spatial resolution raingauge data for calibration of low resolution remote sensing techniques.

#### 3.2 Modelled Microwave Retrieval Accuracy

Retrieval algorithms optimized for each of the three rainfall cases, at each spatial resolution, were derived as described in Section 2.3. For each rainfall case studied, all three retrieval methods were applied. Thus not only can the accuracy using the optimal retrieval function be studied, but also the sensitivity of the errors to realistic storm to storm changes in the optimal rainfall retrieval function. Fig. 9 (a) - (c) show the r.m.s.% error of single image retrievals over an area of about 30 000 km<sup>2</sup>.

At 4 km<sup>2</sup> the simulated rainfall retrievals were at the same horizontal resolution as the original radar data used to derive them. At this resolution, vertical structure variability and ambiguous heavy rainfall areas rather than degraded spatial resolution, then, must be the source of any error. As seen in Fig. 9 (a) - (c) this amounted to between 10% and 25% for instantaneous rain averages over the 30 000 km<sup>2</sup>.

There is generally only minor reductions in accuracy due to degrading the sensor resolution from 4 km<sup>2</sup> to 100 km<sup>2</sup>. The range of r.m.s. errors increased to between 10% and 35% at the more realistic larger microwave radiometer FOV. Naturally, if the retrieval function determined for 4 km<sup>2</sup> was used for all ranges, the averaging out of higher rainfall rates at coarser resolution would have led to drastic errors. These errors could be even more severe if gauge data were used to calibrate the procedure. Proper attention to this resolution dependence has avoided a large part of this problem.

As would be expected, best retrievals were generally obtained using the retrieval algorithm specifically tuned for that day. The J-Day 200 retrievals at coarser resolutions were the only results for which this was not clearly the case.

### 3.3 Area-Threshold Retrieval Accuracy

The r.m.s.% errors for the best possible area-threshold (idealized VIS/IR) retrievals are shown in Fig. 10. At 4 km<sup>2</sup> resolution they range from 15% to 30%, while at 100 km<sup>2</sup> they have increased to 35% to 75%. However, 4 km<sup>2</sup> would be the more typical operational resolution of the VIS/IR system these area-threshold calculations are meant to simulate. At this resolution the errors are comparable with the coarser resolution microwave radiometer techniques.

#### 4. DISCUSSION

The error statistics detailed in Section 3 describe the manner in which the performance of certain satellite-based rainfall measurement techniques would be influenced by the spatial variability of Florida convective rainfall. In these three storm cases, employing another day's optimal retrieval algorithm sometimes doubled the error in comparison to what that storm's optimal algorithm would have obtained. The variability of rainfall characteristics from storm to storm can lead to increased spatial sampling errors.

Simulated microwave retrievals showed errors which generally increased slightly with degrading sensor resolution (Fig. 9 (a) - (c)). The effect of averaging larger and increasingly inhomogenous rain areas into the sensor beam may be partially offset by the averaging out of small scale vertical variability of the precipitation. Actual observations could well be more sensitive to sensor resolution due to broken cloud cover. The brightness temperature observed for cloud-free regions would be substantially cooler than for cloudy regions, and hence more markedly different from raining areas.

Comparing magnitude of error estimates from different studies is difficult. The size of the area and the number of images averaged are also critical to the estimate of average error. This being said, Seed and Austin (1990) estimates a 130% daily temporal sampling error for measurements of rainfall averages over an area of 250 000 km<sup>2</sup>. That error estimate was determined using data from Florida convective rainfall, and considering twice daily overpasses such as what is proposed for the Tropical Rainfall Measuring Mission (TRMM) satellite. That is an area eight times as large as the one in this study, and estimates are averaged over two images. This magnitude of temporal sampling error would certainly dominate over the sorts of spatial sampling errors for simulated microwave retrievals in this work.

In a study using the GATE radar data set from the ITCZ, McConnell and North (1987) found much smaller temporal sampling errors. This difference seems attributable to the more intermittent nature and strong diurnal effects of storms near Florida, outside the ITCZ. For the GATE area of 280 km by 280 km there was a decorrelation time of 7.7 hours for the average rainfall over the region (Bell et. al., 1990). For a larger area of 360 km by 360 km near Florida, Seed and Austin (1990) found 2 to 3 hours to be the decorrelation time. The less intermittent rainfall in the ITCZ would probably also lead to spatial sampling errors smaller than those for Florida rainfall estimates. Thus temporal sampling would likely still be the greater problem.

In Fig. 11 the errors arising from spatial variability of the rainfield are compared

between two measurement methods. The 10 km by 10 km  $T_b$  retrieval is a model for the planned TRMM microwave radiometer. The 2 km by 2 km mean - area retrieval can be taken as an idealized VIS/IR area - threshold system. The coarser resolution microwave simulation is generally more accurate than VIS/IR estimates for single images of the precipitation field. Ambiguities arising from non-raining cloudy areas are present for both VIS/IR and microwave methods. Thus for instantaneous precipitation measurements, the microwave radiometer provides the more accurate estimates. This, however, presupposes that the microwave system has been calibrated against "ground truth" with a spatial resolution comparable with the microwave system. Weather radar would be a natural choice for such a calibration, and should be used in combination with gauge networks in various tropical regions during the TRMM project.

Yet temporal sampling of twice per day, versus twice per hour for a typical VIS/IR system, counters any advantages of a stand-alone microwave system. An idea which has been present in the meteorological remote sensing community for a number of years is to include microwave estimates in an operational trispectral VIS/IR/MR method. Relatively accurate microwave radiometer (MR) retrievals could provide regular real time calibration of VIS/IR rainfall retrieval parameters. Geostationary VIS/IR measurements could then be used to interpolate between radiometer satellite passes.

## 6. CONCLUSION

Three-dimensional radar data was used to simulate satellite-borne microwave radiometer measurements of precipitation fields at 19 GHz. For three Florida convective storms various rainfall retrieval algorithms were used to check the potential accuracy of sensor systems of different footprint sizes. As found by previous researchers, these simulations indicate that such methods can be used to derive useful area-averaged instantaneous rainfall rate estimates. There is potential for microwave radiometer measurements from the planned TRMM satellite to provide better 'snapshot' estimates than area-threshold methods using VIS/IR measurements of cloud fields. Microwave brightness to rainfall rate algorithms depend on the availability of calibration data having a comparable spatial resolution. This suggests a key role for several conventional ground based radars in the tropical regions for the TRMM project. The dominant source of error is then the temporal resolution. With a twice per day sampling strategy, microwave radiometer methods will only be useful for averages over large areas for rainfall types displaying uncharacteristically long decorrelation times. Using microwave radiometer rainfall estimates to operationally optimize the parameters of a VIS/IR system over the oceans is a more promising arrangement than independent microwave systems.

Proper attention to spatial resolution is still crucial in the calibration of rainfall remote sensing methods. The averaging out of high rainfall rates at coarser resolutions dramatically changes the rainfall statistics. Any satellite-based method, calibrated with ground truth of the wrong spatial resolution, will introduce disastrous biases into precipitation estimates.

However, in determining the optimum method for the upcoming TRMM mission, the attenuation radar is also an attractive candidate for use in a trispectral rainfall measurement scheme. The radar system will have a sensor FOV less than that of the microwave radiometer, although a smaller scanning swath. Horizontal averaging errors will be less than for the microwave sensor, but for the same reason there will be less averaging out of the vertical rainfall profile variability. Most radar retrieval algorithms share with radiometer methods the necessity of making assumptions concerning the vertical profile of precipitation. How this radar system might be expected to compare with the microwave radiometer system is a matter worth considering in further accuracy simulation studies. To what extent each could improve the accuracy of a VIS/IR rainfall measurement system should also be addressed.

## ACKNOWLEDGEMENTS:

This work was supported in part by a research grant to Prof. M. Garstang of the University of Virginia as part of the NASA project for TRMM. We acknowledge and appreciate the assistance of Prof. Garstang and his group, of Mr. Otto Thiele of NASA, and of the USAF and contract personnel at Patrick Air Force Base and Cape Canaveral, Florida.

## References

Arkell, R. and M. Hudlow, 1977, *GATE International Meteorological Radar Atlas*. U.S. Dept. of Commerce, NOAA.

Austin, P.M., 1987: Relation Between Measured Radar Reflectivity and Surface Rainfall, *Mon. Wea. Rev.*, **115**, 1053-1073.

Bell, T.L., A. Abdullah, R.L. Martin and G.R. North, 1990: Sampling Errors for Satellite-Derived Tropical Rainfall: Monte Carlo Study Using a Space-Time Stochastic Model, *J. Geophys. Res.*, **95** (D3), 2195-2205.

Calheiros, R.V. and I. Zawadzki, 1987: Reflectivity - Rain Rate Relationships for Radar Hydrology in Brazil, *J. Clim. Appl. Met.*, **26**, 118-132.

Chandrashekar, S., 1960, *Radiative Transfer*. Dover, 393 pp.

Douglas, R.H., 1963: Recent Hail Research: A Review, *Meteorological Monographs*, **5** (27), 164.

Gerrish, H.P. and H.W. Hiser, 1965: Meso-scale studies of instability patterns and winds in the tropics, *Rept. 7*. U.S. Army Electronics Labs., Fort Monmouth, N.J., 63 pp.

Griffith, C.G., W.L. Woodley, P.G. Grube, D.W. Martin, J. Stout and D.N. Sikdar, 1978: Rain Estimation from Geosynchronous Satellite Imagery - Visible and Infrared Studies, *Monthly Weather Review*, **106** (8), 1153-1171.

Langleben, M.P. and W.D. Gaherty, 1957: An Optical System for Automatic Synthesis of Constant-Altitude Radar Maps, *Stormy Weather Group Sci. Rep. MWT-3*. McGill University, Montreal, Canada.

Lovejoy, S. and G.L. Austin, 1979: The Delineation of Rain Areas From Visible and IR Satellite Data for GATE and Midlatitudes,

*Atmos. - Ocean*, 20, 77-92.

Lovejoy, S. and G.L. Austin, 1980: The estimation of rain from satellite-borne microwave radiometers, *Q.J.R.M.S.*, 106, 255-276.

Marshall J.S. and W.M. Palmer, 1948: The Distribution of Raindrops With Size, *J. of Met.*, 5, 165-166.

McConnell, A. and G.R. North, 1987: Sampline Errors of Tropical Rain, *J. Geophys. Res.*, 92 (D8), 9567-9570.

Miller, J.R. Jr., 1972: A Climatological Z-R Relationship For Convective Storms In the Northern Great Plains, *Preprints, 15th Radar Meteorology Conference*, 153-160.

Seed, A. and G.L. Austin, 1990: Variability Of Summer Florida Rainfall and Its Significance For the Estimation Of Rainfall By Gauges, Radar and Satellite, *J. Geophys. Res.*, 95 (D3), 2207-2215.

Short, D.A and G.R. North, 1990: The Beam Filling Error in the Nimbus 5 Electronically Scanning Microwave Radiometer Observations of Global Atlantic Tropical Experiment Rainfall, *J. Geophys. Res.*, 95 (D3), 2187-2193.

Smith, P.L. Jr., 1968: Calibration of Weather Radars, *Proceedings of the 13th Radar Meteorology Conference*, 60-65.

Tees, D. and G.L. Austin, 1989: The Effect of Range on the Radar Measurement of Rainfall, *International Symposium on Hydrological Applications on Weather Radar*. Department of Civil Engineering, University of Salford, U.K., Paper H2.

Wilheit, T.T., A.T.C. Chang, M.S.V. Rao, E.B. Rogers and J.S. Theon, 1977: A satellite technique for quantitatively mapping rainfall rates over the ocean, *J. Appl. Met.*, 16, 531-560.



## Figure Captions

- Fig. 1 - Mean absolute errors between radar and gauges, as a function of Z-R relation parameter  $b$ , for accumulations from 2340-0200 GMT, Sept. 22, 1989. Mean gauge accumulation was 12.1 mm for that time period.
- Fig. 2 - Brightness temperature near 19 GHz as a function of rainfall rate, as shown in Wilheit (1977). A uniform rainfall rate from the ground to a melting layer height of 4 km was used. The three lines are for calculations with the Marshall-Palmer and Sekkhon-Srivastiva drop size distributions (solid lines labelled M-P and S-S), and with the scattering term ignored (dotted line).
- Fig. 3 - Per cent of raining area exceeding each rainfall rate (solid line), and per cent of total storm accumulation due to precipitation intensities exceeding each rainfall rate (dotted line). Calculated from radar observations at 2km by 2km resolution from 1340-1820 GMT, Aug. 20, 1989.
- Fig. 4(a) - 1.5 km radar CAPPI of rainfall rates in mm/hr.
- Fig. 4(b) - Simulated 19 GHz microwave brightness temperature observations in degrees Kelvin.
- Fig. 5 -  $T_b$  threshold (for which area greater than threshold equals area raining) versus resolution.
- Fig. 6 - Rainfall retrieval curves, at three resolutions, optimized for storm of J-Day 232.
- Fig. 7 - Microwave brightness temperature to rainfall rate functions, optimized for each of the three storm cases studied.

- Fig. 8 - Mean measured rainfall rate (over raining areas) versus resolution.
- Fig. 9 - Root mean square of the per centage error for simulated microwave radiometer rainfall retrievals (averaged over an area of 30 000 km<sup>2</sup>) versus sensor resolution. Each plot shows error curves using retrieval functions optimized for each of the three storm cases. Each graph shows results for simulated retrievals of one of the storms studied.
- Fig. 10 - Root mean square of rainfall retrieval errors for measurements by a 'perfect' area-mean system over an area of 30 000 km<sup>2</sup>.
- Fig. 11 - Comparison of root mean square percentage errors of rainfall retrievals (over a 30 000 km<sup>2</sup> area) for two methods, optimized for each of the three rainfall cases.

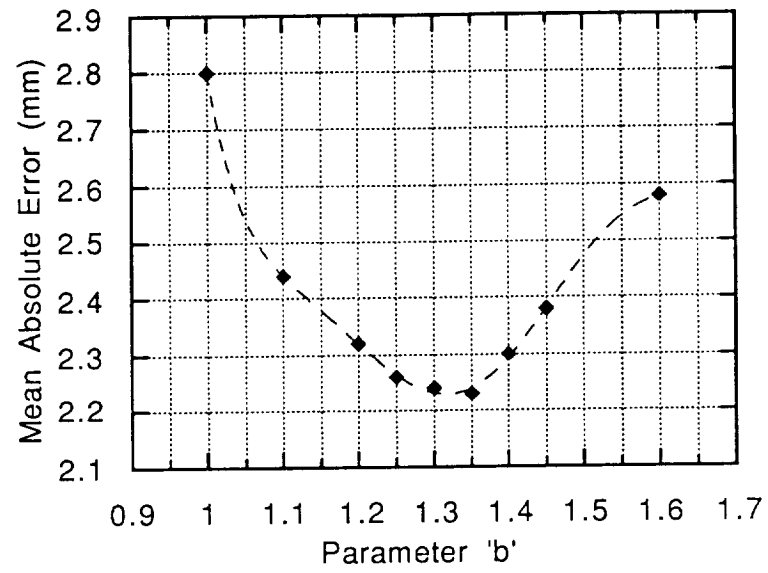


Fig. 1

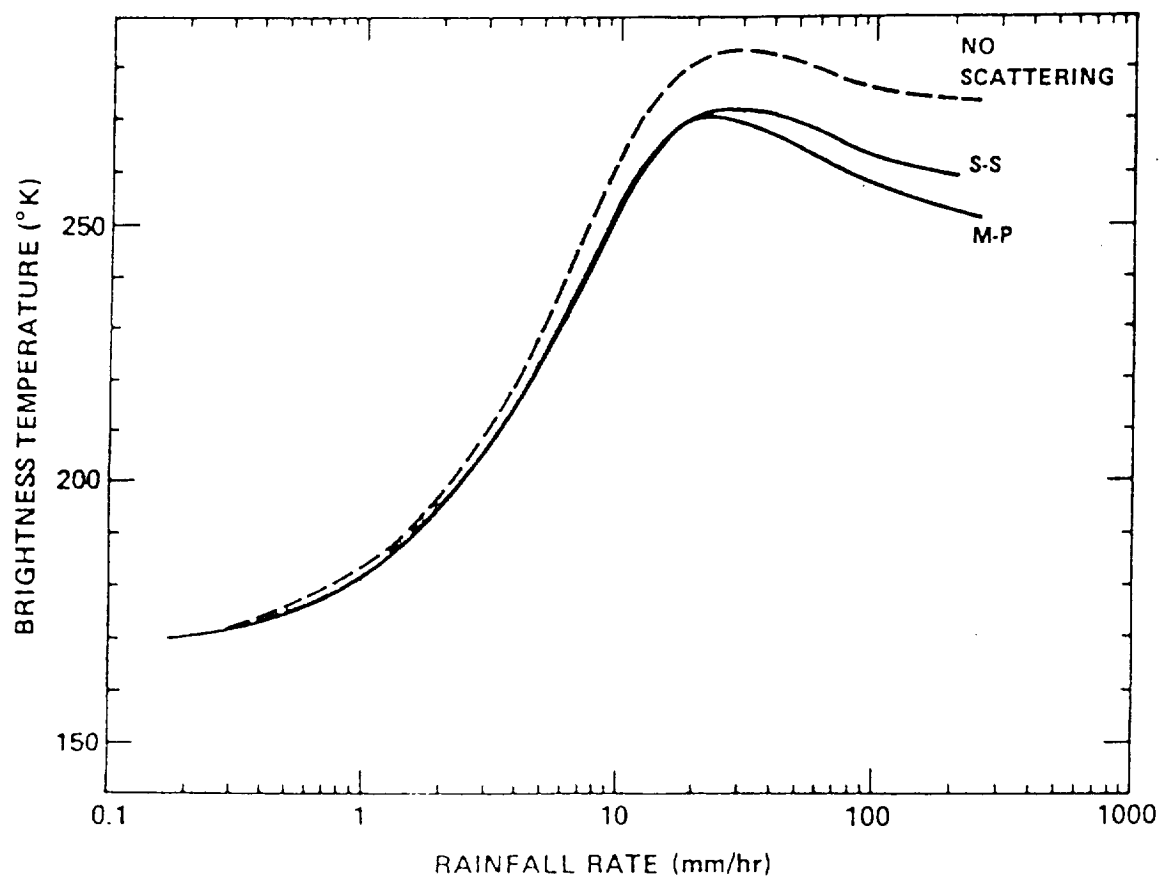


Fig. 2

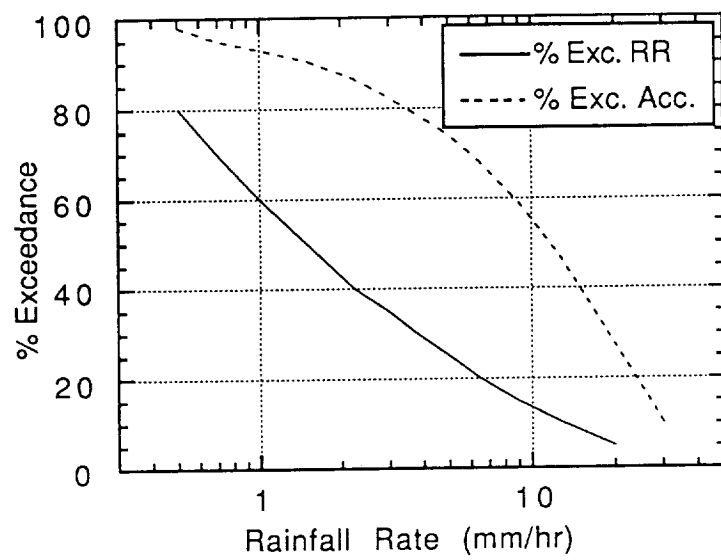
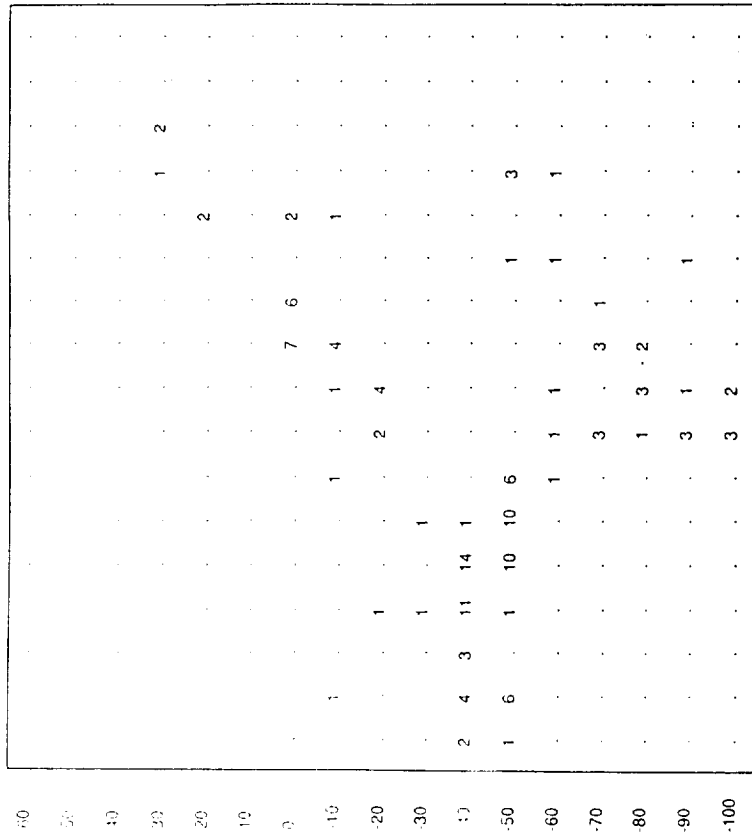


Fig. 3

KSC\_NEW 13:59 GMT DAY = 20 MONTH = 8 YEAR = 1989

km N of radar

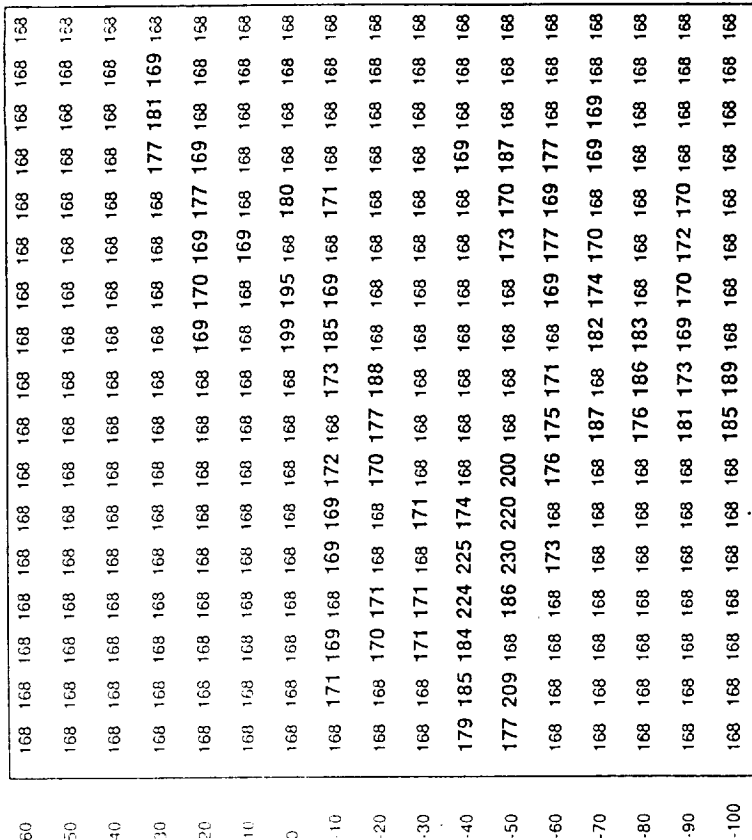


km E of radar

Fig. 4 (a).

KSC\_NEW 13:59 GMT DAY = 20 MONTH = 8 YEAR = 1989

km N of radar



km E of radar

Fig. 4 (b).

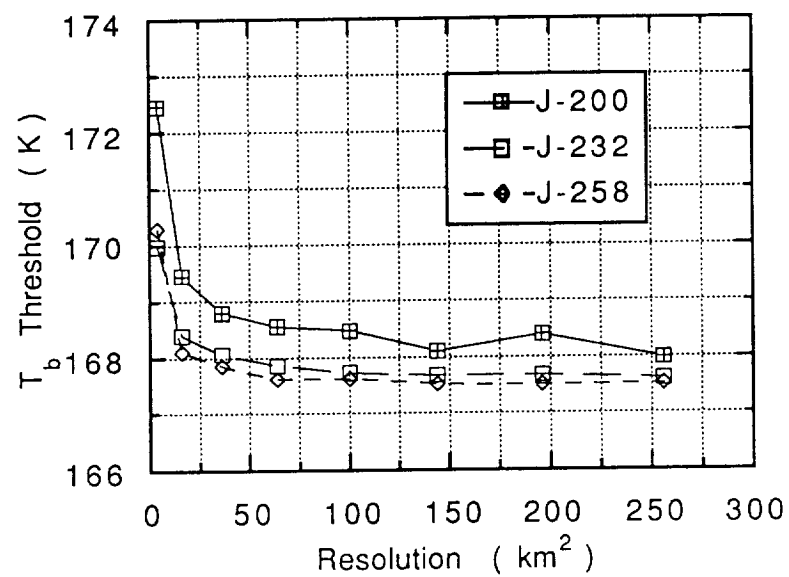


Fig. 5

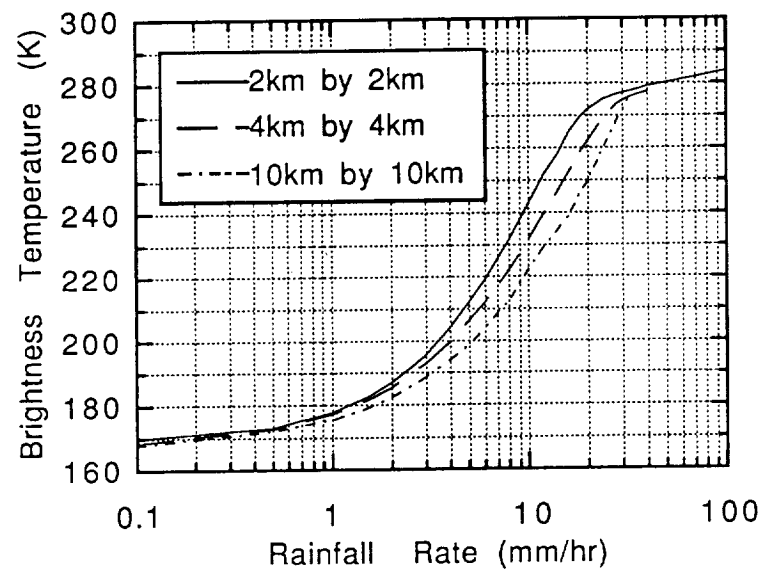


Fig. 6



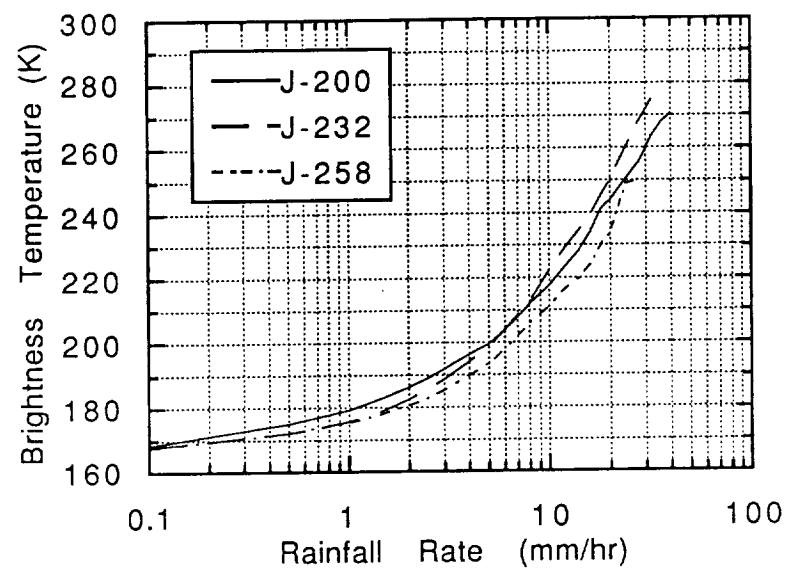


Fig. 7

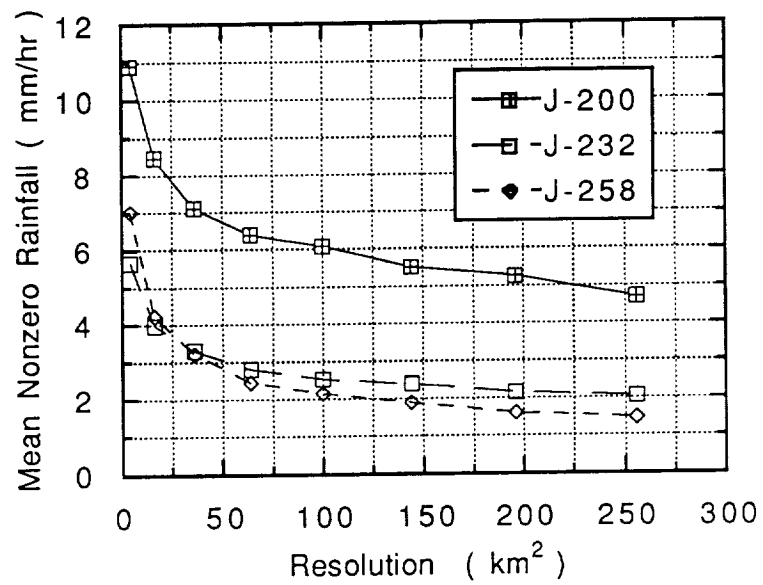


Fig. 8

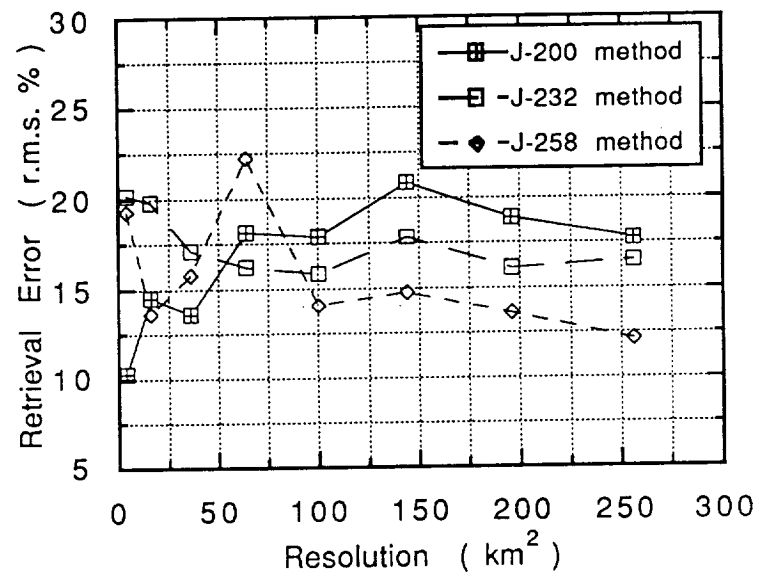


Fig. 9(a)

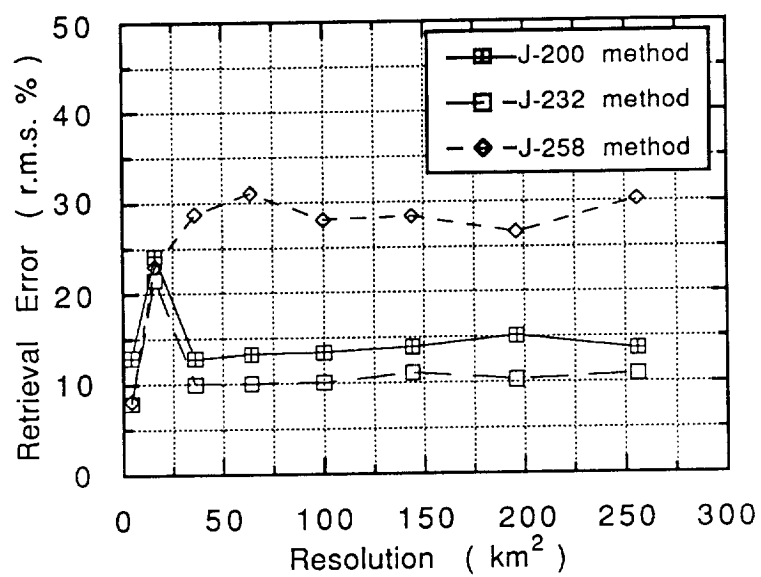


Fig. 9(b)

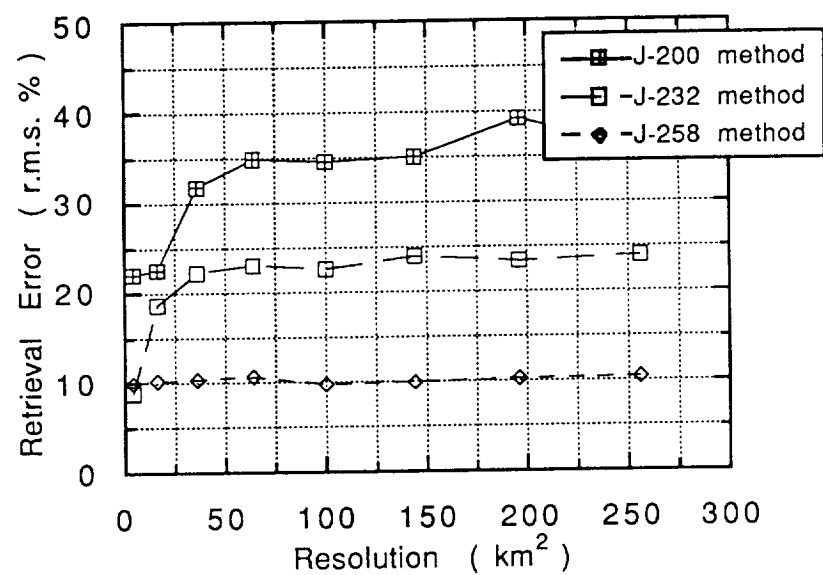


Fig.. 9(c)

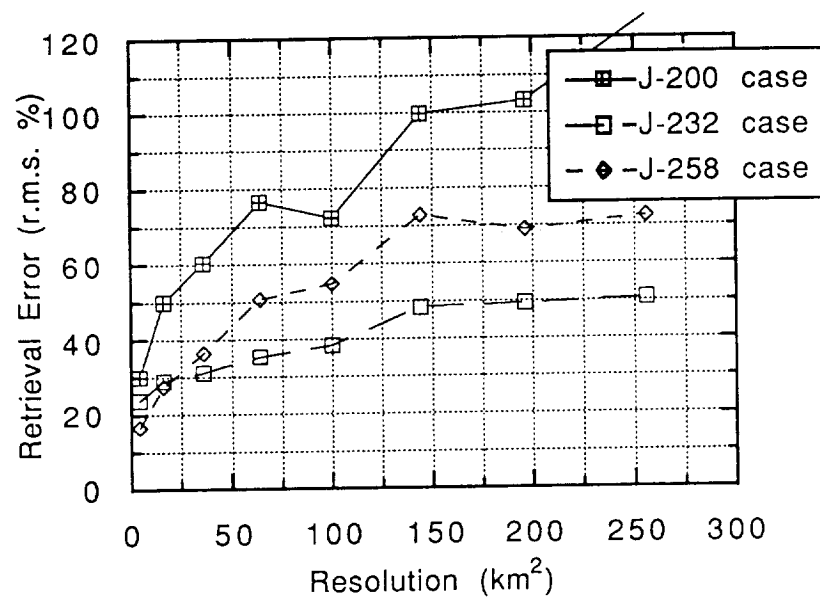


Fig. 10

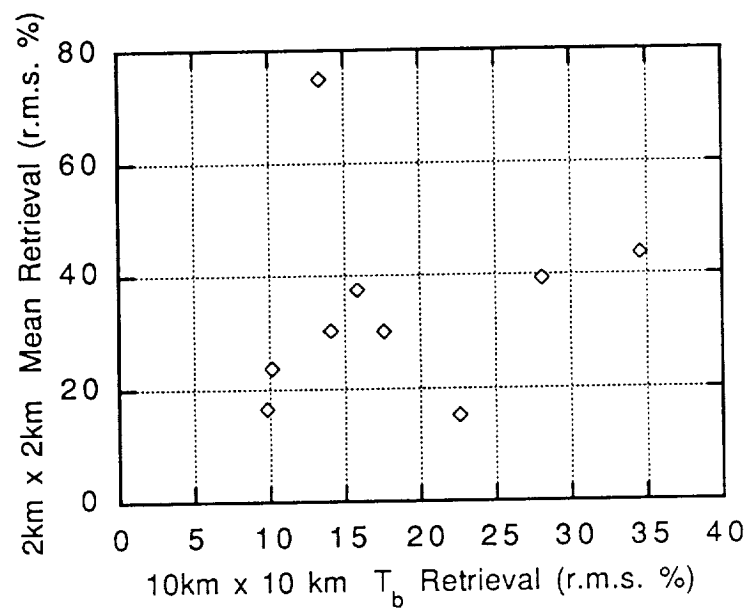


Fig. 11